Title
Imaging Interacting Electrons in van der Waals Moiré Heterostructures

Author
Li, Hongyuan

Publication Date
2023

Peer reviewed|Thesis/dissertation

Imaging Interacting Electrons in van der Waals Moiré Heterostructures

By

Hongyuan Li

A dissertation submitted in partial satisfaction of the

requirements for the degree of

Doctor of Philosophy

in

Applied Science and Technology

in the

Graduate Division

of the

University of California, Berkeley

Committee in charge:

Professor Feng Wang, Chair
Professor Junqiao Wu
Professor Michael F. Crommie

Spring 2023

Abstract

Imaging Interacting Electrons in van der Waals Moiré Heterostructures

by

Hongyuan Li

Doctor of Philosophy in Applied Science and Technology

University of California, Berkeley

Professor Feng Wang, Chair

The discovery of two-dimensional (2D) van der Waals heterostructure provided a highly tunable material platform with multiple knobs and hence extremely large phase space to study novel quantum phenomena. Particularly, the emergence of moiré heterostructures, formed by stacking two slightly mismatched atomic lattices, opened a new world to explore 2D interacting electrons owing to their new length and energy scale compared with conventional systems. On the one hand, the electron correlation effect in moiré heterostructure is greatly enhanced, leading to the emergence of a variety of correlated ground states such as correlated insulator, electron crystal, and unconventional superconductivity. On the other hand, the moiré potential also significantly impacts the excited states of interacting electrons such as generating novel excitonic states. Signatures of these novel quantum phenomena of moiré interacting electrons have been observed through mesoscopic measurements such as electrical transport and optical spectroscopy. However, their microscopic natures, such as local interaction strength and charge spatial distribution, remain mostly underexplored for lack of an effective probe tool.

My PhD mainly has focused on exploring the interacting electrons in 2D moiré heterostructures through developing a series of novel imaging techniques based on scanning tunneling microscopy (STM). In this thesis I will discuss my efforts in the last five years in four parts.

The first part briefly introduces the background knowledge used in the thesis. I will first discuss the material platform studied here: from 2D van der Waals materials to moiré heterostructure. Next, I will introduce a classic lattice model for correlated electrons: the Fermi-Hubbard model. Finally, I will talk about the main experimental instrument used here: STM and its various applications.

The second part explores the fundamental atomic and electronic structures in moiré heterostructure that consists of two works. The first one studies the atomic and single-particle electronic structures of a moiré heterostructure microscopically. The moiré superlattice and electronic minibands in a WS_2/WSe_2 moiré heterostructure are imaged with STM and STS. A three-dimensional atomic reconstruction was found to be present in the moiré heterostructure and responsible for the moiré potential. The second work

studies the electron Coulomb interactions in this moiré superlattice. Using STM tip as local gate, we can control the cascade discharge of nearby moiré electrons, through which the nearest-neighbor Coulomb interaction can be experimentally measured.

The third part describes our efforts on imaging an exotic correlated ground state of interacting moiré electrons, generlazied Wigner crystal, through developing a novel non-invasive microscopic thermodynamic probe tool. We innovatively employed a non-invasive graphene-sensing-layer assisted STM probe method, and for the first time saw the images of electron crystals after its prediction about 90 years ago. We further developed this imaging technique and demonstrated it to be a local thermodynamic measurement of correlated electrons. Through controlling the STM tip bias, we can locally excite an electron or hole quasiparticle and measure the local thermodynamic gaps. This technique is the so far one of the thermodynamic probes with the highest spatial resolution (~nm).

The last part studies the microscopic nature for photoexcited states of interacting electrons in TMD moiré superlattice. Through combing laser excitation with STM we realized the probe of transient photoexcited states. With this technique we directly imaged the internal electron and hole distributions within a new type of charge-transfer moiré excitons.

To my parents,
Xiaoyin Li and Yun Xia

Table of contents

List of figures

List of tables

Acknowledgments

Completing a PhD is a challenging and rewarding journey that requires support and encouragement from many individuals. I would like to take this opportunity to express my gratitude to those who helped me to achieve this milestone in my academic career.

First and foremost, I am deeply indebted to my supervisor, Prof. Feng Wang, for his guidance and encouragement throughout my PhD journey. I still remember when I first joined his group, I lacked even the most fundamental knowledge about condensed matter physics and my research view and taste is very limited. However, through our interactions during the last five years, his expertise, insights and constructive feedback has greatly expanded my horizon about this field and reshaped the direction and scope of my research. Particularly, his brilliant physics knowledge has greatly enhanced my research progress. I am grateful for his patience, kindness, and willingness to go above and beyond to ensure my success.

Additionally, I would like to express my heartfelt gratitude to Prof. Michael F. Crommie, my collaborator (even more like a co-supervisor). My early days on STM research were difficult since I am completely new and ignorant to it. During that time, I learned a lot of STM expertise from him, and our discussions have generated many great research ideas. Particularly, I also learned a lot from him about scientific writing and communication. I am grateful for the opportunity to work with him during my PhD.

I would also thank Dr. Shaowei Li (now a professor) for teaching and guiding me how to perform STM research step by step. In the early days, even after I made many mistakes, he could still fix everything and encouraged me. I learned almost everything about STM and UHV experiment from him. I am grateful for all the guidance from him.

As an experimentalist, I am fortunate enough to work with the most brilliant theorists here in Berkeley. I would thank Prof. Steven G. Louie and his group members especially Dr. Mit H. Naik for providing strong theory and calculation support.

Staying in Berkeley for five years, I am glad to have the precious opportunity to work with all the great colleagues from different groups. I would like to thank Ziyu xiang for our close collaboration on all the STM projects in my last two years, without whom the projects cannot be finished smoothly. Also, I would never forget the support from Dr. Wenyu Zhao, Dr. Sihan Zhao, Dr. Lili Jiang, Emma Regan, Danqing Wang, Dr. Sudi Chen, Shaoxin Wang, Salman Khan, Dr. Zuocheng Zhang who helped a lot on fabricating the complicated samples. When building experimental setups, I received support from Dr. Tiancong Zhu and Dr. Yoseob Yoon, Dr. Sheng Wang and I want to thank them as well. Of course, my PhD would not be complete without support from all the other students and postdocs in Feng's group and they are Dr. Seok Jae Yoo, Dr. Halleh Balch, Dr. Tairu Lyu, Dr. Iqbal Utama, Dr. Andrew Y. Joe, Zheyu Lu, Collin Sanborn, Can Uzundal, Ruishi Qi, Jingxu Xie, Qixing Feng, Haleem Kim, and Dishan Abeysinghe.

Finally, I want to thank the support and encouragement from Siyu He in all ways during the hard time of my PhD.

1 Introduction

1.1 2D van der Waals Moiré Superlattices

Since the first exfoliation of graphene flakes by A. Geim and K. Novoselov in 2004(*1*) (which earned them a Nobel Prize in 2010), the research of 2D materials has flourished. Due to the very thin nature of 2D materials (usually one layer of atoms), 2D materials have exhibited many exciting electrical, optical, and mechanical properties for both scientific and engineering purposes. Furthermore, their 2D nature allows us to easily stack different layers to form a heterostructure that has dramatically different properties from the pristine 2D layers. The numerous ways of combining different 2D materials greatly enlarges the physics world to explore. Particularly, the discovery of moiré heterostructures created a new lattice platform that owns completely different length scale and energy scale compared with conventional systems such as atomic lattices or cold atoms, where rich new quantum phenomena have been observed. All the experimental works described in this thesis are performed on 2D van der Waals moiré superlattice. Therefore, I will first briefly introduce 2D van der Waals materials, especially graphene, hexagonal boron nitride (hBN) and transition metal dichalcogenides (TMD) semiconductors, the main building blocks for the sample used in this thesis. Next, I will discuss the concept of 2D heterostructures and moiré superlattice.

A monolayer graphene is composed of a honeycomb lattice of carbon atoms (illustrated in Figure 1-1A), where two sublattices (labeled as A and B) are included within the unit cell. The honeycomb lattice yields a hexagonal first Brillouin zone as shown in Figure 1-1B. The electronic properties of graphene are mainly contributed by the p_z orbitals of the carbon atoms. Its electronic band structure can be calculated with a tight-binding model with the result shown in Figure 1-1C. Here the low-energy states are mainly localized around the two inequivalent K and K' valleys where the band dispersion is linear (zoom-in image shown in Figure 1-1C). Near the K/K' valleys, the Hamiltonian can be approximately expressed as

$$H = \hbar v_F \boldsymbol{\sigma} \cdot \boldsymbol{k} = \begin{pmatrix} 0 & k_x - ik_y \\ k_x + ik_y & 0 \end{pmatrix}, \tag{1.1}$$

where v_F is the Fermi velocity, $\boldsymbol{\sigma}$ is the Pauli matrices acting on the space expanded by the wavefunctions localized at the A and B sublattices, and $\boldsymbol{k}$ is the wavevector. The energy spectrum can be obtained as $E(k) = \pm\hbar v_F|k|$, where the positive (negative) part is for the conduction (valence) band. This Hamiltonian indicates that the quasiparticles in monolayer graphene are massless Dirac Fermion, an important property that we utilized in the work described in Chapter 4 and 5. Only monolayer graphene is mentioned here but we note that multilayer graphene can have different atomic and electronic structures(*2*).

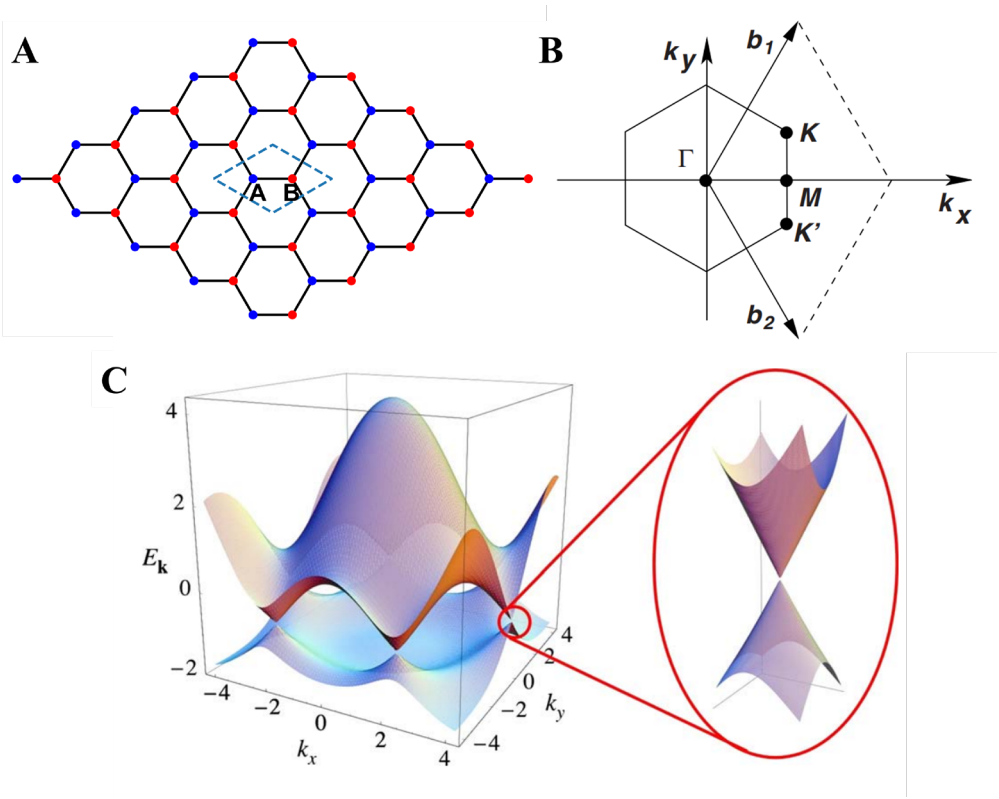

Figure 1-1 Structure of a monolayer graphene. **A**. The honeycomb structure of a monolayer graphene where two sublattices (labeled as A (blue) and B (red)) are included in a unit cell (contoured by blue dashed line). **B**. First Brillouin zone of the monolayer graphene. **C**. Electronic band structure of the monolayer graphene. The low-energy states are mainly localized around the two inequivalent K and K' valleys where the band dispersion is linear. B and C adapted from reference(*2*)

Hexagonal boron nitride (hBN) owns a similar atomic structure to graphene except that the A and B sublattices are occupied by boron (B) and nitrogen (N) atoms instead of carbon atoms as in graphene (Figure 1-1A). The inequivalent B and N atoms leads to an onsite energy difference between the A and B sublattices and hence changes the electronic structure. Its Hamiltonian near the two K valleys can be obtained by including the onsite energy difference, denoted as 2Δ, to Eq. (1.1) that yields,

$$H = \hbar v'_F\left(k_x\sigma_x + k_y\sigma_y + \Delta\sigma_z\right) = \begin{pmatrix} \Delta & k_x - ik_y \\ k_x + ik_y & -\Delta \end{pmatrix}, \qquad (1.2)$$

Its energy spectrum can be obtained as

$$E(k) = \pm\hbar v'_F\sqrt{k^2 + \Delta^2}. \qquad (1.3)$$

Therefore, a bandgap of 2Δ exists at the two K valley. For hBN this gap is pretty large and more than 5eV(*3, 4*), meaning hBN is very insulating and transparent for visible light. The atomically flat surface and large bandgap of hBN make it an ideal material to serve as the dielectric (dielectric constant ~4) and protection layer in the fabrication of various 2D heterostructure devices.

2D transition metal dichalcogenides (TMD) such as WS_2, WSe_2, and $MoSe_2$ are a large class of materials with exciting electronic and optical properties. The atomic structures of TMD monolayers are shown in Figure 1-2A, where the two most common structures are the 2H and 1T phases. The typical electronic band structure of a 2H-phase MoS_2 monolayer is shown in Figure 1-2B, which exhibits a direct band gap at the K/K' points of the Brillouin zone. However, depending on the material types and layer numbers, both direct and indirect bandgaps can exist in TMD materials(*5*). Research of 2D TMD materials has received wide attention since the first observation of the photoluminescence in MoS_2 monolayers(*6, 7*). They show interesting optical properties such as valley polarized excitation by circularized polarized light(*8*) and large exciton binding energy due to its 2D nature that lacks dielectric screening(*9*). TMD semiconductors also serve as promising candidates for developing the next-generation nanoelectronics devices such as field-effect transistors(*5, 10*).

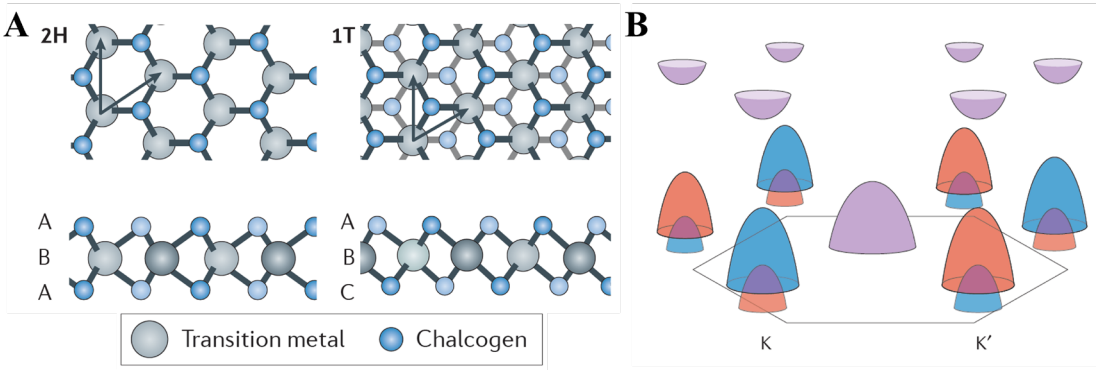

Figure 1-2 Structures of TMD materials. atomic structure of the 2H (left pannel) and 1T (right panel) phases of TMD. **B**. Schematic of the electronic band structure of a monolayer 2H-MoS_2. The spin-orbital coupling induces a large splitting between spin up (blue) and down (orange) states for the valence band edge at K/K' valleys. Adapted from reference(*5*).

Even though these pristine 2D materials themselves have exhibited rich novel electronic and optical properties, their combinations can even in exciting induce the emergence of more exotic quantum phenomena. Since these 2D materials are atomically thin, they can be easily stacked to form various heterostructures (illustrated in Figure 1-3A)(*11*). The different layers are so close to each other (sub-nm gap) that their electrons can easily couple with each other and consequently make the heterostructure behave like a new material. 2D heterostructures have been intensively studied during the last decade due to their greatly controllability. First, there are numerous ways to construct the 2D heterostructures with multiple tunable knobs such as layer stacking order and horizontal twist angle. Second, individual 2D materials layer can be *in situ* tuned electrically and optically.

The state-of-art technique for fabricating high-quality 2D heterostructure device now are mainly based on the polymer-stamp assisted dry-transfer method first demonstrated by L. Wang *et.al.(12)*. The main process is illustrated in Figure 1-3B. 2D flakes can be picked up layer by layer using polymer stamps such as polydimethylpolysiloxane

(PDMS) and poly(propylene) carbonate (PPC) at low temperature (below the polymer glass transition temperature). During this process, via utilizing a micromanipulator, the alignment of different layers can be precisely controlled. Once the stacking of all 2D layers is finished the heterostructure can be released from the polymer stamp by increasing the temperature above the glass transition.

In this thesis we mainly focus on the heterostructures consisting of TMD semiconductors. The electronic behavior in such heterostructures quite depends on the band alignment of the two composing semiconductor layers. Generally, three types of band alignment can exist, as illustrated in Figure 1-3C. In the type I alignment, both the conduction and valence band edges of the heterostructure are within the same layer (right), that hence dominates the low-energy electron behavior. In the type II situation, the conduction and valence band edges are vertically localized in different layers, indicating that the electron and hole quasiparticles are spatially separated. Exotic excited states such interlayer excitons have been observed in such systems(*13, 14*). In the type III band alignment, the valence band top of one layer has even higher energy than the conduction band bottom of the other layer. Consequently, interlayer charge transfer takes place making the heterostructure metallic. We note that the band alignment can be affected by not only the material types but also external parameters such as vertical electrical field (tuning the onsite energy difference of each layer). In certain cases, it is even possible to reverse the band alignment with external electrical field(*15*).

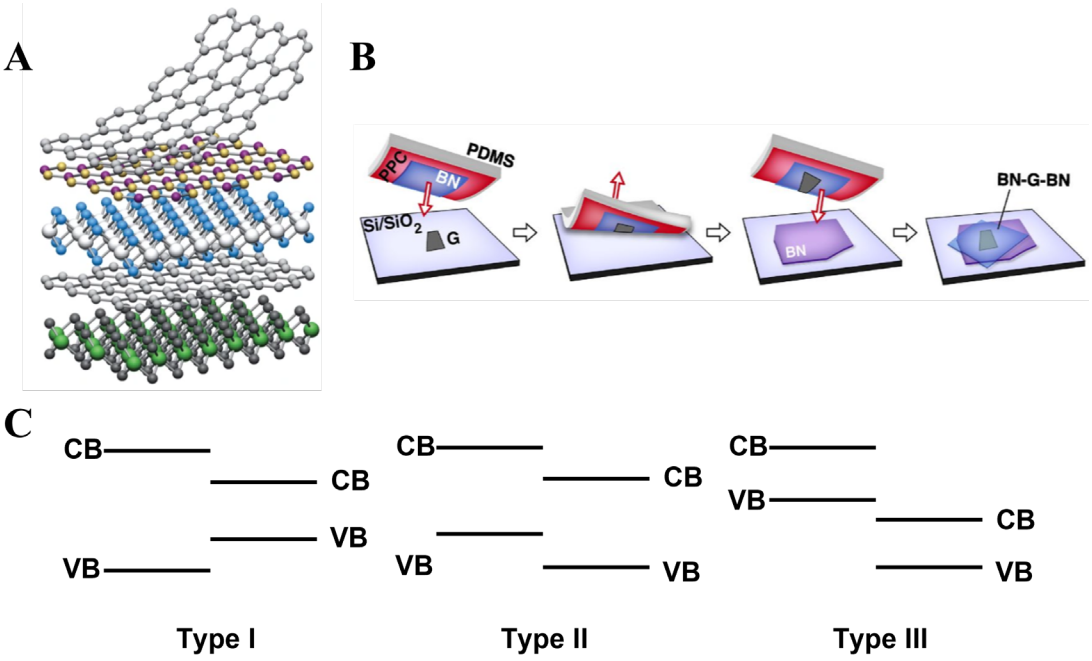

Figure 1-3 2D van der Waals heterostructure. **A**. Different 2D material layers can be stacked on each other to form a 2D heterostructure, where the stacking order and twist angle can be precisely controlled nowadays. Adapted from reference(*11*). **B**. Illustration of a typical 2D heterostructure fabrication process enabled by the polymer stamp dry-transfer method. Adapted from reference(*12*). **C**. Different types of band alignment for 2D semiconductor heterostructures.

The capability of precisely controlling the lattice alignment between different layers creates a new platform to study 2D quantum physics, moiré heterostructures. The moiré heterostructures are formed when two 2D flakes with similar lattice constant and orientation are stacked together. The spatial interference of the two sets of slightly mismatched atomic lattices generates a larger new lattice, the moiré superlattice (illustrated in Figure 1-4A). The moiré lattice constant L can be obtained through the formula,

$$L = \frac{a_1}{\sqrt{\delta^2 + \theta^2}}, \tag{1.4}$$

where $\delta = (a_1 - a_2)/a_1$ is the lattice mismatch, a_1 and a_2 are the lattice constants of the two atomic lattices, and θ is their twist angle. As a comparison, the typical moiré lattice constant of experimental interest is in the order of 10nm while the atomic lattice constant is usually in the order of 0.3nm. The large moiré superlattice is accompanied by a smaller mini-Brillouin zone (illustrated in Figure 1-4B).

The moiré superlattice significantly alters the electronic structures of 2D heterostructure. First, the lattice with a new length scale ($L/a \sim 30$) changes electrons' energy scale and their correlation strength. The Coulomb potential energy (PE) between nearest-neighbor electrons is proportional to $1/L$, while the kinetic energy (KE) $p^2/2m$ in lattice model is proportional to $1/L^2$ ($p = \hbar k$ where $k \sim \pi/L$). Both PE and KE get suppressed with a larger lattice constant while their ratio PE/KE, reflecting the electron correlation strength, is proportional to L and get enhanced. The stronger correlation effect in moiré superlattices has induced the observation of exotic quantum phases recently such as correlated insulator(*16-18*), superconductivity(*19-23*), Chern insulator(*24-26*), and ferromagnetism(*24, 27*). Second, the moiré superlattice applied an extra moiré potential on the 2D heterostructure. These potentials, depending on their strength and spatial landscape, can modify the electronic band structure (such as including moiré minibands) and change charge spatial distribution in both ground and excited states of interacting electrons. Most work described in this thesis focuses on exploring the moiré-induced novel correlated ground and excited states.

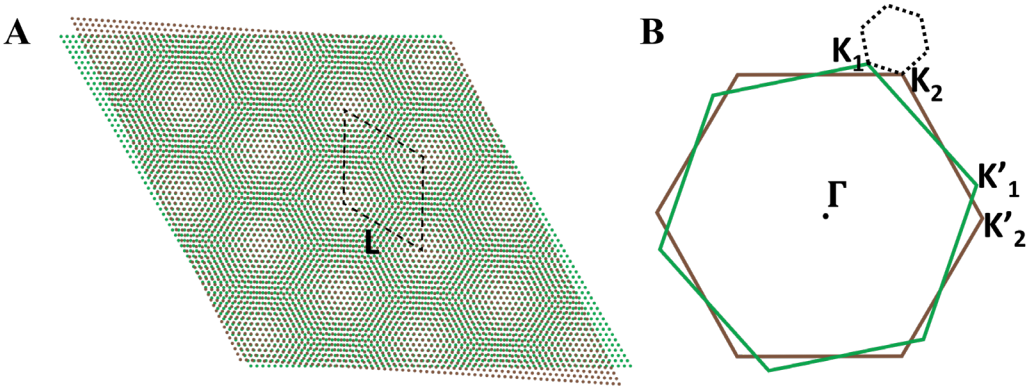

Figure 1-4 Moiré superlattice. **A**. The moiré superlattice formed by stacking two mismatched atomic lattices. **B**. Schematic of the moiré mini-Brillouin zone (blacked dashed line) folded from the two larger atomic Brillouin zones.

1.2 Interacting electrons: Hubbard Model

One of the best-known lattice models describing interacting electrons is the Fermi-Hubbard model (abbreviated as Hubbard model here). First introduced by J. Hubbard in 1967, this model has shown great success in studying many important strongly correlated phenomena such as Mott insulator, magnetism, and high-temperature superconductors. Here we will give it a short introduction.

Starting from a general lattice model with L sites that includes interaction between particles which has the Hamiltonian.

$$H = \sum_{ij\sigma} t_{ij} c_{i\sigma}^{\dagger} c_{j\sigma} + \sum_{ijmn} \sum_{\sigma\sigma'} v_{ijmn}\, c_{i\sigma}^{\dagger} c_{j\sigma'}^{\dagger} c_{m\sigma'} c_{n\sigma}. \tag{1.5}$$

where $c_{i\sigma}^{\dagger}$ and $c_{i\sigma}$ are the creation and annihilation of an electron at site i with spin σ, t_{ij} is the hopping energy between site i and site j, and v_{ijmn} is the general interaction term. Here we have assumed a constant onsite energy ε and neglected the onsite energy and chemical potential terms (assuming $\varepsilon - \mu = 0$). If we restrict ourselves to hopping and interaction within the nearest-neighbor regime, and further neglect the terms with smaller energy scale, we arrive at the generalized Hubbard model with the Hamiltonian.

$$\begin{aligned} H = -t \sum_{<i,j>\sigma} \left(c_{i\sigma}^{\dagger} a_{j\sigma} + c_{j\sigma}^{\dagger} a_{i\sigma}\right) + U \sum_{i} n_{i\uparrow} n_{i\downarrow} \\ + \frac{1}{2} U_{NN} \sum_{<ij>} n_i n_j, \end{aligned} \tag{1.6}$$

where $< i, j >$ denotes the nearest-neighbor sites, $t = -t_{ij}$ is the nearest-neighbor hopping term, $U = v_{iiii}$ is the onsite repulsion energy, and $U_{NN} = 2v_{ijij}$ is the nearest-neighbor repulsion energy. It is noteworthy that we have neglected the terms proportional to v_{iiij}, v_{ijji} and v_{iijj}, which describe the bond-charge interaction, nearest-neighbor spin exchange interaction and the hopping of a pair of electrons, respectively(*28*). The generalized Hubbard model can be further simplified by neglecting the nearest-neighbor interaction yielding the well-known Hubbard model.

$$H = -t \sum_{<i,j>\sigma} \left(c_{i\sigma}^{\dagger} a_{j\sigma} + c_{j\sigma}^{\dagger} a_{i\sigma}\right) + U \sum_{i} n_{i\uparrow} n_{i\downarrow}. \tag{1.7}$$

We note that keeping only the onsite repulsion term U is enough for understanding many important phenomena such as the Mott insulator and antiferromagnet at half-filling. However, to describe some exotic phases of matter such as the generalized Wigner crystal at fractional filling of the lattice (which will be studied in detail in Chapter 4 and 5), it is still necessary to consider the generalized Hubbard model. For now, we just focus on the Hubbard model.

Despite the simple form of the Hubbard model, it is actually challenging to obtain the general solutions of it (for one-dimension it can be exactly solved by the Bethe

Ansatz method(*29*)). However, it is still meaningful to check a few special situations so that we can have a general understanding of it.

In the limit of $t/U \to 0$, it is simplified to the common tight-binding model without electron interactions. It can be easily solved through the Fourier transformation $c_{i\sigma}^{\dagger} = \frac{1}{\sqrt{L}}\sum_{\boldsymbol{k}} e^{-i\boldsymbol{k}\cdot\boldsymbol{r}_i} c_{\boldsymbol{k}\sigma}^{\dagger}$ that yields

$$H = \sum_{\boldsymbol{k}\sigma} \varepsilon(\boldsymbol{k}) c_{\boldsymbol{k}\sigma}^{\dagger}\, c_{\boldsymbol{k}\sigma}, \tag{1.8}$$

where $\varepsilon(\boldsymbol{k})$ is the energy dispersion. Particularly, for 2-dimensional lattice with direct lattice vectors $\boldsymbol{a}_1$ and $\boldsymbol{a}_2$, $\varepsilon(k)$ can be calculated as $\varepsilon(\boldsymbol{k}) = -2t[\cos(\boldsymbol{k}\cdot\boldsymbol{a}_1) + \cos(\boldsymbol{k}\cdot\boldsymbol{a}_2)]$ for a square lattice and $\varepsilon(\boldsymbol{k}) = -2t[\cos(\boldsymbol{k}\cdot\boldsymbol{a}_1) + \cos(\boldsymbol{k}\cdot\boldsymbol{a}_2) + \cos\big(\boldsymbol{k}\cdot(\boldsymbol{a}_1+\boldsymbol{a}_2)\big)]$ for a triangular lattice. In the limit of $t/U \to \infty$ it is simply a classical model with no quantum hopping between different sites. The energy will simply be U multiplied by the number of double occupied sites.

In the case of nonzero U and t, the Hubbard model is generally hard to solve while we can check the situation of a (over)simplified two-site Hubbard model that can still reveal some important properties of correlated electrons. Before solving it, we first note some important symmetries of the Hubbard model. It can be shown that the Hamiltonian in Eq. (1.7) commutes with the total number of electrons with spin up $N_{\uparrow} = \sum_i n_{i\uparrow}$ and spin down $N_{\downarrow} = \sum_i n_{i\downarrow}$, that is, $[H, N_{\uparrow}] = [H, N_{\downarrow}] = 0$. Therefore, the total number of electrons with different spins are conserved in the Hubbard model. Therefore, the two-site model can be diagonalized by blocks under different combinations of $N_{\uparrow}$ and $N_{\downarrow}$: ($N_{\uparrow}$, $N_{\downarrow}$) = (0, 0), (1, 0), (0, 1), (2, 0), (0, 2), (1, 1), (2, 1), (1, 2), and (2, 2). For convenience, we denote the Hamiltonian and energy in different blocks as $H(N_{\uparrow}, N_{\downarrow})$ and $E(N_{\uparrow}, N_{\downarrow})$, respectively. The blocks of (0, 0), (0, 2), (2, 0), and (2, 2) are all 1-dimensional where the inters-site hopping is forbidden due to either no electrons or Pauli exclusion principle. Their energy can be easily calculated as $E(0,0) = E(0,2) = E(2,0) = 0$ and $E(2,2) = 2U$. The blocks of (1, 0), (0, 1), (1, 2), and (2, 1) are two-dimensional where the inter-site hopping is allowed. The Hamiltonian in the subspace can be written as

$$\begin{aligned} H(0,1) = H(1,0) &= \begin{bmatrix} 0 & -t \\ -t & 0 \end{bmatrix}, \\ H(2,1) = H(1,2) &= \begin{bmatrix} U & -t \\ -t & U \end{bmatrix}, \end{aligned} \tag{1.9}$$

and yields the energy spectrum of $E(1,0)_{\pm} = E(0,1)_{\pm} = \pm t$ and $E(1,2)_{\pm} = E(2,1)_{\pm} = \pm t + U$. The (1, 1) block is 4-dimensional that acts on states of $|\uparrow,\downarrow\rangle$, $|\uparrow,\downarrow\rangle$, $|\uparrow\downarrow,0\rangle$, and $|0,\uparrow\downarrow\rangle$, with the Hamiltonian

$$H(1,1) = \begin{bmatrix} 0 & 0 & -t & -t \\ 0 & 0 & -t & -t \\ -t & -t & U & 0 \\ -t & -t & 0 & U \end{bmatrix}, \tag{1.10}$$

It yields an energy spectrum of $E(1,1)_1 = 0,\ E(1,1)_2 = U, E(1,1)_3 = U/2 - \sqrt{4t^2 + U^2/4}$, and $E(1,1)_4 = U/2 + \sqrt{4t^2 + U^2/4}$. We have summarized the complete energy spectrum of this two-site Hubbard model in Table 1 where $N = N_\uparrow + N_\downarrow$ is the total electron number.

N	$\lvert N_\uparrow - N_\downarrow \rvert$	E
0	0	0
1	1	$\pm t$
2	0	$0, U, \frac{U}{2} \pm \sqrt{4t^2 + \frac{U^2}{4}}$
	2	0
3	1	$\pm t + U$
4	0	$2U$

Table 1 Energy spectrum of the two-site Hubbard model.

We can further study the thermodynamic properties via considering the grand canonical ensemble with the Hamiltonian of $H' = H - \mu N$. The ground state energy E' as a function of μ can be calculated as

$$E' = \begin{cases} 0, & (\mu \le -t, N = 0) \\ -t - \mu, & (-t < \mu \le t + \frac{U}{2} - \sqrt{4t^2 + \frac{U^2}{4}}, N = 1) \\ \frac{U}{2} - \sqrt{4t^2 + \frac{U^2}{4}} - 2\mu & (t + \frac{U}{2} - \sqrt{4t^2 + \frac{U^2}{4}} < \mu \le -t + \frac{U}{2} + \sqrt{4t^2 + \frac{U^2}{4}}, N = 2) \\ -t + U - 3\mu & (-t + \frac{U}{2} + \sqrt{4t^2 + \frac{U^2}{4}} < \mu \le U + t, N = 3) \\ 2U - 4\mu & (\mu > U + t, N = 4) \end{cases} \quad (1.11)$$

More information can be obtained if we plot the μ as a function of the ground state electron number N (Figure 1-5). At large U/t, a gap in μ comparable to U emerges at the half-filling ($N = 2$). In real space $N = 2$ means both sites are occupied with an electron and hence to add one more to either site must overcome the onsite repulsion U. For other filling factors, the gaps in μ mostly originates from the intersite hopping. Figure 1-5 also reveals that at half-filling this system has a small electronic compressibility (defined as $\Delta N/\Delta\mu$ here).

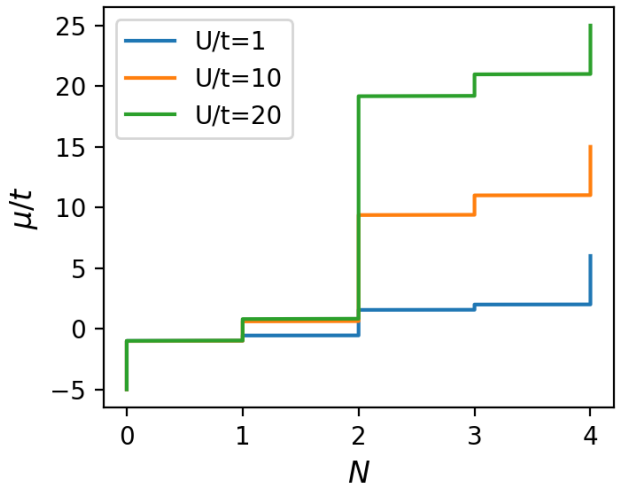

Figure 1-5 Chemical potential as a function of the total electron number for the two-site Hubbard model.

We can further fix the electron number to half-filling (N = 2) and check the spin behaviors. As shown in Table 1, the antiferromagnetic ($|N_\uparrow - N_\downarrow| = 0$) and ferromagnetic ($|N_\uparrow - N_\downarrow| = 2$) ground states have energies of 0 and $U/2 - \sqrt{4t^2 + U^2/4}$, respectively. That effectively defines an exchange interaction between the two sites as $J = \sqrt{4t^2 + U^2/4} - U/2$ (we set J to be positive since the ferromagnetic phase has lower energy). In the limit of $t/U \ll 1$, it can be approximated as

$$J = \frac{U}{2}\left(\sqrt{1 + \frac{16t^2}{U^2}} - 1\right) \approx \frac{4t^2}{U}. \tag{1.12}$$

This antiferromagnetic exchange interaction originates from the fact that the electrons with opposite spins still allow the intersite hopping which tends to lower the energy while this hopping is forbidden for the same-spin situation.

Although only the over-simplified two-site Hubbard model is considered above, its many important properties naturally extend to the real Hubbard model with more sites (~10^{23}). For example, a half-filled band without electron interaction usually means a metal with large electronic compressibility (defined more precisely as $dn/d\mu$, where n is the electron density) at the Fermi level. However, if we gradually increase the onsite repulsion U, a correlated gap emerges and yields zero electronic compressibility at the Fermi level (illustrated in Figure 1-6). According to the Einstein relation, the conductivity σ_c can be related to the compressibility as $\sigma_c = e^2 D \frac{dn}{d\mu}$, where D is the diffusion constant and e is the electron charge(*30*). Therefore, such electronic interactions induce a transition from metal to the Mott insulator. On the other hand, in the strong coupling limit $t/U \ll 1$ and around half-filling, the Hubbard model can yield the well-known t-J model through a Schrieffer–Wolff transformation and excluding the terms that requires double occupancy of a single site, that is

$$H = -t \sum_{<i,j>\sigma} \left(c_{i\sigma}^{\dagger} a_{j\sigma} + c_{j\sigma}^{\dagger} a_{i\sigma}\right) + \frac{4t^2}{U} \sum_{<i,j>} (\boldsymbol{S}_i \cdot \boldsymbol{S}_j - \frac{1}{4} n_i n_j). \qquad (1.13)$$

Indeed the Hubbard model can host a complicated phase diagram with many interesting correlated quantum phases(*31*) such as antiferromagnetism, strange metal, high-T_c superconductivity and so on, while we will not be able to introduce all of them here.

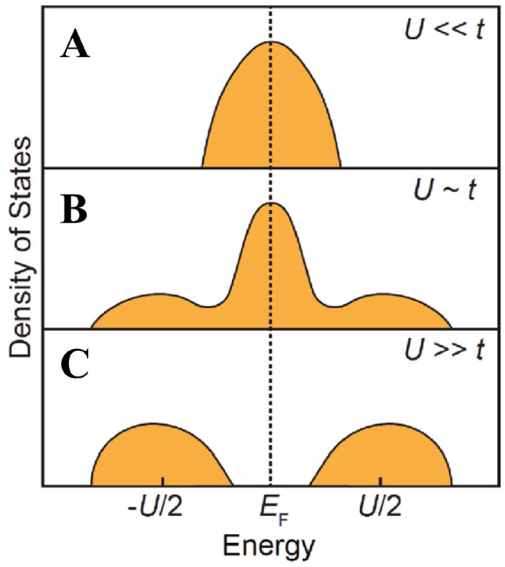

Figure 1-6 Illustration of the Mott transition in 3-dimensional situation.When U is small, the band is half filled and the material behaves like metal. **B**. When U is increased, the electronic interaction starts to play a role and the system can be described by Landau's Fermi liquid theory. At the Fermi level (E_f), there is finite density of states for the quasiparticle. **C**. When U is much larger than the hopping energy, the Mott transition can take place and induce a correlated gap around the Fermi level. Adapted from reference(*32*).

Particularly, in the above discussion about Hubbard model, we only include the onsite repulsion that predicts the correlated gap at half filling. However, if the long-range Coulomb interactions such as the nearest-neighbor interaction are also included as in the case of the generalized Hubbard model, a richer group of correlated insulating phases can emerge. As a topic explored in detail in this thesis, here we will briefly introduce the generalized Hubbard model. In the Hubbard model the large onsite repulsion leads to the Mott insulator at half filling corresponding to one electron filled per site spatially (each site hosting at most two electrons with opposite spins). With the longer-range Coulomb repulsion turned on, intuitively it can be expected that the electrons tend to fill only a fraction of the available sites to avoid not only double occupancy of single site and but also nearest-neighbor occupancy. To minimize the total potential energy, the electrons can form a new lattice with a larger lattice constant than the hosting atomic lattice. This new correlated phase is the so-called generalized Wigner crystal, a generalization of the electron Wigner crystal that first predicted in strongly interacting electron gas on a lattice model that is first proposed by J. Hubbard(*33*). The generalized Wigner crystal features a

filling-factor dependent lattice structure so that the electron lattice can be commensurate with the host lattice. More details about the this generalized Hubbard model and its correlated phases will be discussed in Chapter 4 and 5.

1.3 Scanning Tunneling Microscopy and Spectroscopy

One direct way to study the microscopic nature of moire interacting electrons is to perform high-resolution real-space imaging. However, such imaging tasks are beyond the capability of conventional optical microscopes due to their diffraction limit. One suitable tool used during my PhD is the scanning tunneling microscope (STM), a powerful microscopic technique widely used in condensed matter physics and surface science. A short introduction to STM will be given here.

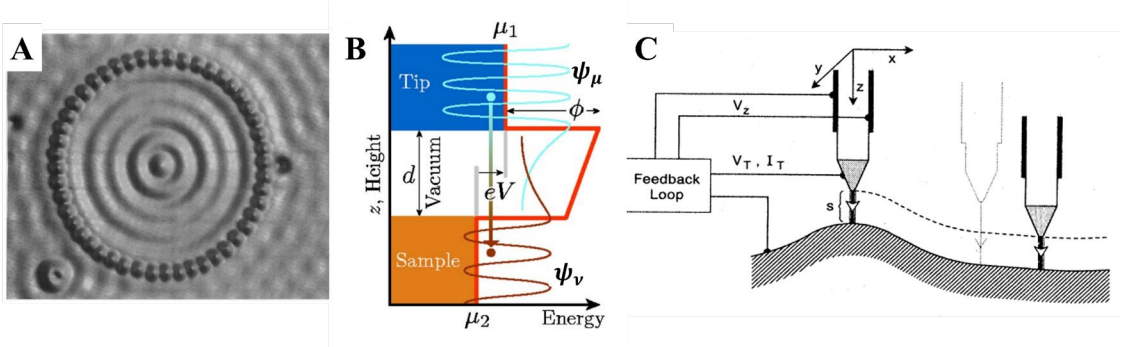

Figure 1-7 Scanning tunneling microscope. **A**. Image of the quantum corral constructed by iron atoms on copper surface. Adapted from reference(*34*). **B**. Energy diagram of the quantum tunneling through the vacuum barrier between a STM tip and the sample. Adapted from reference(*35*). **C**. Schematic of the scanning tunneling microscope working in constant current mode. Adapted from reference(*36*).

First demonstrated by G. Binnig and H. Rohrer at IBM Zurich in 1981, STM showed its powerful imaging capability that can even resolve a single atom, which soon yielded a Nobel Prize in 1986. For example, Figure 1-7A shows the famous image of the quantum corral of irons atoms by M. F. Crommie *et.al.* STM relies on the quantum tunneling of electrons across a small vacuum gap between a sharp metallic tip and the sample surface (Figure 1-7B). By measuring the tunneling current in different modes, STM can provide rich microscopic information of the sample surface. Particularly it can not only image surface topography but also probe local electronic structures through scanning tunneling spectroscopy (STS), the two most widely used measurements in STM studies.

We first provide a quantitative review of the quantum tunneling current in STM measurement following the methods by J. Tersoff and D. R. Hamann(*37*) as well as J. Bardeen(*38*). The tunneling current given by Bardeen's formalism is

$$I = \frac{2\pi e}{\hbar}\sum_{\mu,\nu} f(E_\mu)[1 - f(E_\nu - eV)]|M_{\mu\nu}|^2 \delta(E_\mu - E_\nu), \qquad (1.14)$$

where $f(E)$ is the Fermi-Dirac distribution, V is the bias applied between the sample and the tip, $M_{\mu\nu}$ is the tunneling matrix element between state ψ_μ and ψ_ν in the tip and sample (Figure 1-7B), respectively, and E_μ (E_ν) is the energy of state ψ_μ (ψ_ν). Here the term $f(E_\mu)[1 - f(E_\nu + eV)]$ represents that only tunneling from an electron filled state to an empty state is allowed by the Pauli exclusion principle, and the term $\delta(E_\mu - E_\nu)$ indicates the tunneling is elastic. The tunneling matrix element term $|M_{\mu\nu}|^2$ can be calculated with the time-dependent pertubation theory, and J. Bardeen gave a symmetric form of $M_{\mu\nu}$ as

$$M_{\mu\nu} = \frac{\hbar^2}{2m} \int d\boldsymbol{S} \cdot \left(\psi_\mu^* \boldsymbol{\nabla} \psi_\nu - \psi_\nu \boldsymbol{\nabla} \psi_\mu^*\right), \tag{1.15}$$

where the integral is over any surface within the vacuum gap region that separates the tip and sample. Since within a small energy range the tunneling matrix element is almost independent of energy and at low temperature $f(E)$ can approximated as a step function, Eq. (1.14) can be further approximated as

$$I = \frac{2\pi e}{\hbar} |M|^2 \int_0^{eV} \rho_t(E_F - eV + \varepsilon) \rho_s(E_F + \varepsilon)\, d\varepsilon, \tag{1.16}$$

where ρ_t and ρ_s are the local density of states (LDOS) for the tip and sample and respectively. Here we have neglected the subscript for the tunneling matrix element. Therefore, the tunneling current depends mostly on the tunneling matrix element and the available density of states for the sample and tip.

STM can measure the sample surface topography by scanning the tip over the surface while maintaining a constant tunneling current (constant-current mode) (Figure 1-7C). The tip is mounted on a piezoelectric scanner that can be moved in three dimensions with sub-Å precision. As the tip approaches the surface, the tunneling current between the tip and the surface increases exponentially due to the decrease in vacuum gap and hence the increase the tunneling matrix element. The tunneling current is measured by the STM and is used to control the position of the tip to maintain a constant current. As the tip is scanned over the surface, it follows the contour of the surface, maintaining a constant distance and tunneling current between the tip and the surface. In this way, STM can measure the topography of a sample surface. Due to the short-range nature of the quantum tunneling and its exponential dependence of the tip-sample distance, STM can easily achieve atomic-resolution imaging.

STM can also be used in combination with spectroscopic techniques to perform scanning tunneling spectroscopy (STS), which allows for the measurement of the LDOS of sample surface. Since most STM tips are made of metal with large and nearly constant density of states around its Fermi level, we can approximate ρ_t in Eq. (1.16) as a constant and it yields

$$|M|^2 \rho_t \int_0^{eV} \rho_s(E_F - eV + \varepsilon)\, d\varepsilon, \tag{1.17}$$

Therefore, the derivative of the tunneling current with respect to the bias directly reflects the sample density of states,

$$\frac{dI}{dV} \propto \rho_s(E_F - eV)d\varepsilon, \tag{1.18}$$

Overall, STS is a powerful technique that allows for the measurement of the LDOS at the atomic scale. By combining STS with other techniques, such as spin polarized STM, researchers can gain a detailed understanding of the electronic structure and properties of materials.

Beyond topography imaging and STS measurement of LDOS, STM can also provide some other measurement capabilities. Exploring the novel application of STM is one of the main themes of this thesis, where we have developed multiple different STM techniques to locally probe interacting electrons. Here I will just introduce one feature about STM measurement that is important but may not be widely realized in the condensed matter community, STM tip local gating effect (or local band bending effect). This feature enables us to achieve many important applications of STM as discussed later.

Besides the quantum tunneling, the STM tip also performs a non-negligible pertubation to the sample surface due to the local electric field near tip apex. In most conventional STM measurements, it is simply assumed such local electric field does not significantly affect the measurements. This assumption works fine for samples with large density of states (such as metals), where the tip local electric field is easily screened by the sample and the local properties are not affected very much. However, this assumption fails for the STM measurements of samples with finite density of states or energy gaps near the Fermi level, such as molecules on insulating substrate, where the screening the tip local electric field may not be enough. Consequently, it can change the number of electrons filled in the sample locally (local doping level) and hence alter the sample's Fermi level position. In this case, the tip also plays the role of a local electrostatic gate. Such an effect has been noticed in previous STM studies of systems such as molecules(*39*) and defects(*40*) where the so-called charging/discharging effects have been observed.

1.4 Outline of This Thesis

This thesis mainly focuses on exploring the quantum behavior of interacting electrons in 2D moiré heterostructure through developing novel microscopic imaging techniques based on STM. It is organized as follows.

Chapter 2 describes our work on probing the atomic and electronic (single-particle level) structures of a TMD moiré heterostructure with STM and STS. The moiré superlattice and electronic minibands are spatially visualized. We found that a 3D atomic reconstruction exists in the moiré heterostructure and provides the moiré potential for valence band edge states.

Chapter 3 studies the electron Coulomb interactions in TMD moiré superlattice. Using STM tip as local gate, we can control the cascade discharge of nearby moiré

electrons, through which the nearest-neighbor Coulomb interaction can be experimentally measured.

Chapter 4 describes our efforts on imaging an exotic correlated phase of electrons, generlazied Wigner crystal, in TMD moiré heterostructure. We innovatively employed a non-invasive graphene-sensing-layer assisted STM probe method, and for the first time saw the images of electron crystals after its prediction about 90 years ago.

Chapter 5 discusses our further development of the sensing-layer assisted STM imaging technique. We demonstrated it to be a local thermodynamic measurement of correlated electrons. Through controlling the STM tip bias, we can locally excite an electron or hole quasiparticle and measure the local thermodynamic gap. This technique is the so far one of the thermodynamic probes with the highest spatial resolution (~nm).

Chapter 6 studies the photoexcited states of interacting electrons in TMD moiré superlattice. Through combing laser excitation with STM, we directly imaged the internal electron and hole distribution within photoexcited charge-transfer moiré excitons.

2 Imaging moiré flat bands in 3D reconstructed WSe_2/WS_2 superlattices

2.1 Introduction and Background

Moiré superlattices in two-dimensional (2D) heterostructures provide an attractive platform to explore novel correlated physics since nearly flat electronic bands can be engineered to enhance the effects of electron-electron correlations. This was first seen in graphene-based moiré superlattices where correlated insulator states, superconductivity, and ferromagnetic Chern insulators have been observed in both twisted bilayer(*16, 19, 20, 41, 42*), double bilayer(*43-45*), and ABC trilayer(*21, 24, 46*) moiré system. The TMD-based moiré superlattice can have even flatter minibands, thus enhancing the role of the long-range Coulomb interactions. They have recently emerged as a new model system to explore novel strongly correlated quantum phenomena, such as the correlated insulators and generalized Wigner crystal(*47-51*). More exotic emerging states, such as charge transfer insulators and pair density waves, have been predicted to emerge from theoretical models of hole-doped WSe_2/WS_2 moiré heterostructures(*52, 53*). These correlated phenomena, however, depend sensitively on the precise structural and electronic properties of the underlying moiré superlattice due to the delicate interplay among atomic geometry, moiré band structure and Coulomb interactions. Fundamental understanding and quantum control of TMD-based moiré phenomena thus require both quantitative knowledge of 3D superlattice reconstructions at the atomic level and flat band electronic structure at the meV energy level, something that has hitherto been missing.

Scanning tunneling microscopy (STM) provides a powerful tool to characterize the atomic and electronic structure of moiré superlattices. Previous STM studies have successfully observed localized moiré flat bands and correlated electronic gaps in twisted bilayer graphene(*54-57*), and demonstrated moiré site-dependent electronic structure in TMD moiré superlattice(*58-60*). Narrow moiré flat bands at the valence band edge of TMD heterostructure, however, have not yet been reported. Part of the challenge is the difficulty in fabricating high-quality exfoliated TMD moiré heterostructures on insulating substrates that are suitable for STM characterization. As a result, previous STM studies often focused on chemical vapor deposition (CVD) grown TMD heterostructures on conducting graphite. CVD growth, however, yields lower sample quality and very limited control of stacking order and twist angle of the TMD heterostructure compared to exfoliation and stacking techniques. A graphite substrate can also pin the Fermi level of the TMD material and induce undesirable electronic screening and modification of TMD band structure(*61-63*).

In this chapter, I will describe our efforts in determining the moiré flat band electronic structure of three-dimensional (3D) reconstructed WSe_2/WS_2 moiré superlattices by combining scanning tunneling spectroscopy (STS) of high quality exfoliated TMD heterostructure devices with *ab initio* simulations of both atomic geometry and electronic

band structure of TMD moiré superlattices. Our STM imaging and theoretical simulations reveal a striking 3D buckling reconstruction of the WS_2/WSe_2 heterostructures that is accompanied by strong strain redistribution within the moiré superlattice. We observe multiple moiré flat bands at the valence band edge that originate from the K-point, as well as a separate set of deep lying moiré flat bands that originate from the Γ-point (Our convention is to refer the K- and Γ-points of the unfolded WSe_2 Brillouin zone (BZ) instead of the moiré BZ). The top-most valence flat band from K-point is prominently narrow with a width of only 10 meV and is expected to be responsible for recently observed novel correlated insulator behavior and generalized Wigner crystal states(*47-49, 51*). The strong localization of this band at the $B^{Se/W}$ stacking site revealed by STS spatial mapping contradicts previous simplified density functional theory (DFT) calculations which predict localization at the AA site(*52, 53, 58, 59*). The STS results, however, are fully consistent with our DFT results obtained using calculated large 3D reconstructed moiré superlattice. Our results show that the unexpected 3D moiré reconstruction and strain redistribution play a dominant role in determining the lowest energy moiré flatbands in WS_2/WSe_2 heterostructures.

This work cannot be finished without a close collaboration between different groups. The STM work was mainly done by Shaowei and me with the support from the Wang group and Crommie group, while the theoretical calculation was done by Mit in the Louie group. Part of the discussion is also presented in a published paper(*64*).

2.2 Gate Tunable TMD Device for STM Study

To perform STM study of a gate tunable TMD moiré heterostructure on an insulating substrate, that enables electrostatic doping and further study of its strongly corelated physics, we designed and fabricated a special device. The schematic of our designed WSe_2/WS_2 heterostructure device is shown in Figure 2-1. We used an array of graphene nanoribbons (GNRs) as contact electrodes, and the silicon substrate as a back gate to control the carrier density of the heterostructure. However, to make such a gate tunable TMD heterostructure device for STM study is a nontrivial task. To achieve this, we developed a series of novel sample fabrication techniques. The graphene/WSe_2/WS_2/hBN stack is fabricated using the micro-mechanical stacking techniques. A poly(propylene) carbonate (PPC) film stamp was used to pick up all exfoliated 2D material flakes in the following order: hBN, WS_2, WSe_2, and then graphene nanoribbons. The PPC film together with the stacked sample was then peeled, flipped over, and transferred onto a SiO_2/Si substrate (SiO_2 thickness 285nm). The PPC layer is subsequently removed using ultrahigh vacuum annealing at 230 °C, resulting in an atomically-clean heterostructure suitable for STM measurements. The GNR array here provides a relatively low drain resistance for STM measurement of the TMD heterostructure on an insulating substrate, since graphene electrodes have lower contact resistance compared to deposited metal(*65*), and the STM tip can be placed very close to the graphene boundary. The graphene nanoribbon arrays were fabricated before the stacking process by cutting exfoliated graphene using the electrode-free local anodic oxidation technique(*66*). 50nm Au and 5nm Cr were evaporated onto the graphene to make electric contact.

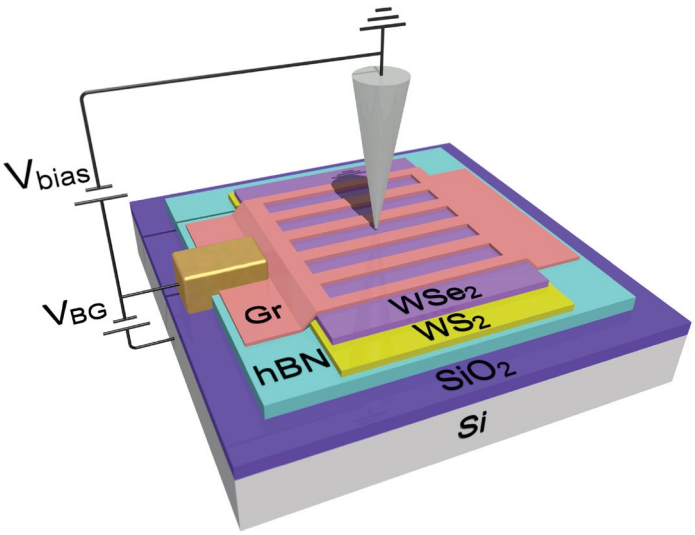

Figure 2-1 Schematic of gate-tunable WSe_2/WS_2 heterostructure device used for STM study. Graphene nanoribbons (Gr) are placed on top of the WSe_2/WS_2 as contact electrodes.

Figure 2-2A shows an ambient AFM image of the top surface of the fabricated device: an array of GNRs (each separated by 100~200 nm) partially covers the WSe_2/WS_2 heterostructure. Figure 2-2B shows an enlarged large scale ultra-high vacuum (UHV) STM image of the heterostructure. The moiré superlattice can be clearly resolved in both the exposed TMD and GNR-covered areas, demonstrating the high quality of the heterostructure device.

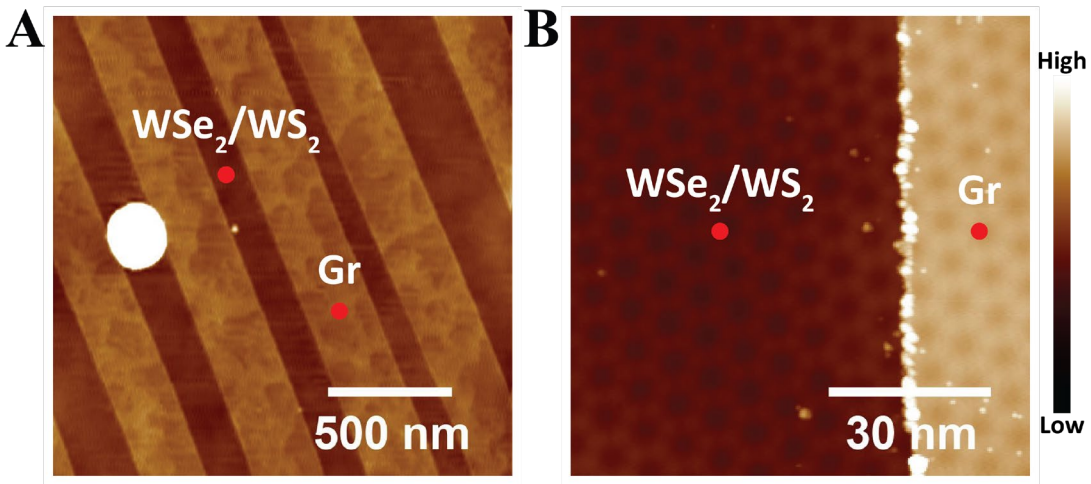

Figure 2-2 Topography of the interface between the WSe_2/WS_2 hetetrostructure and GNRs. **A**. Room temperature ambient AFM image of the sample surface. Exposed WSe_2/WS_2 and graphene-covered areas are labeled. **B**. UHV STM image of the exposed WSe_2/WS_2 and graphene-covered area (T = 5.4K). A Moiré superlattice can be seen clearly in both areas. V_{bias} = -3V, I = 100pA.

2.3 Atomic Structure: Three-dimensional Moiré Reconstruction

With STM measurement, we can first investigate the atomic structure of this WSe_2/WS_2 moiré heterostructure. Figure 2-3A shows a zoom-in STM image of the moiré superlattice in the exposed TMD area. It shows a moiré period of 8.16 nm, consistent with the period expected for an aligned WSe_2/WS_2 heterostructure with a near-zero twist angle. Importantly, the heterostructure shows large height variation at different sites within a moiré unit cell, resulting in an overall honeycomb lattice characterized by a large valley at each hexagon center that is surrounded by six peaks. The apparent height variation in an STM image always results from a convolution of geometric height change and electronic LDOS change, making it difficult to determine "true" height variation via STM. To eliminate this complication, we exploited the graphene covered TMD region, where the thin graphene layer covers the moiré superlattice conformally, but the electronic LDOS of graphene remains nearly constant. Figure 2-3B displays an STM topography image of the moiré superlattice in the graphene covered area using a bias of -0.19V. This bias lies within the TMD gap, and so all of the tunneling current flows through the graphene layer. The similarity between Figure 2-3A and Figure 2-3B confirms that the WSe_2/WS_2 topographical landscape does, in fact, feature six peaks surrounding one valley. The moiré superlattice is formed by a periodic change in the layer stacking configurations between the top WSe_2 and the bottom WS_2 layers. Three high-symmetry stacking configurations are illustrated in Figure 2-3C, and denoted as the $B^{W/S}$, $B^{Se/W}$, and AA stackings, respectively. $B^{W/S}$ and $B^{Se/W}$ correspond to AB stackings.

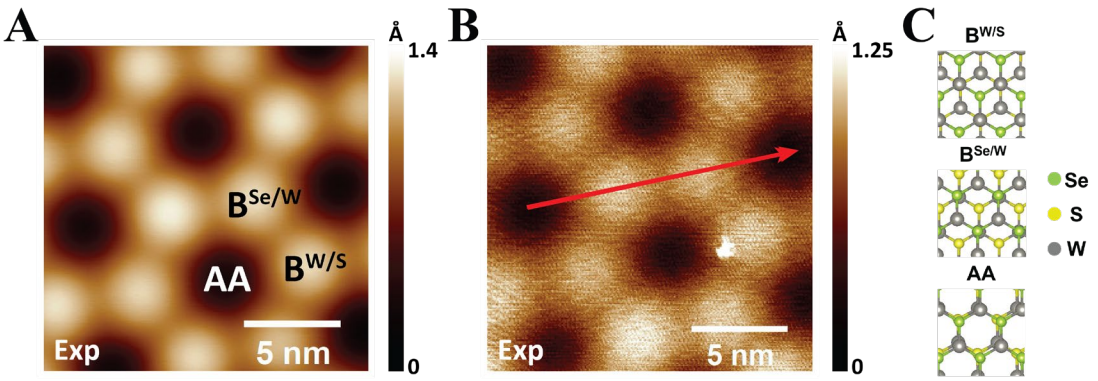

Figure 2-3 High-resolution STM topography image of the moiré superlattice. **A**. STM image of the exposed WSe_2/WS_2 area shows a moiré period of ~8nm. Vbias = -3V, I = 100pA. **B**. STM image of the graphene-covered area (Vbias = -0.19V. I = 100pA). The STM image here better reflects the true topography of the heterostructure (see text). **C**. Schematic of the three types of stacking: BW/S, BSe/W and AA.

A common explanation for height modulation in TMD heterostructures is the stacking-dependent layer separation: the AA stacking has the largest interlayer spacing due to steric hindrance from the overlap of Se atoms in the WSe_2 layer and S atom in the WS_2 layer, while the $B^{Se/W}$ and $B^{W/S}$ stacking sites have smaller interlayer separations. To better understand the structural reconstruction of the moiré pattern, we first carried out a forcefield-based simulation of the superlattice. Figure 2-4 shows the resulting interlayer spacing distribution in a vertical-only relaxed, free-standing simulated WS_2/WSe_2

superlattice which indeed exhibits a peak at the AA stacking site. This stacking-dependent layer separation, however, does not explain our experimental data since it predicts a peak (AA) surrounded by six valleys ($B^{W/S}$ and $B^{Se/W}$), exactly the opposite of the STM images shown in Figure 2-3A and Figure 2-3B.

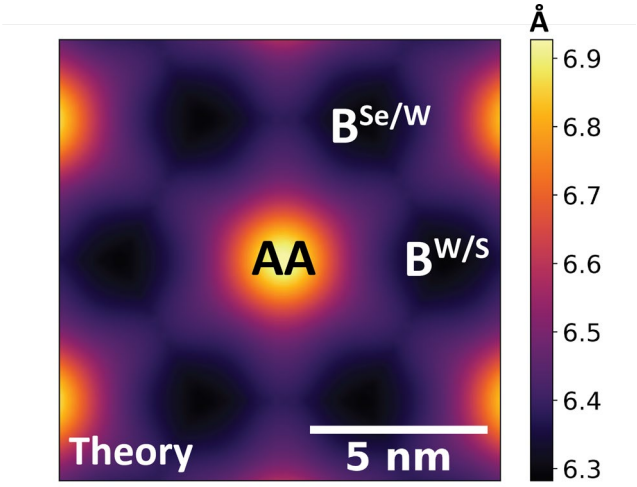

Figure 2-4 Simulated interlayer spacing distribution. The AA sites show the highest interlayer spacing while the $B^{Se/W}$ and $B^{W/S}$ sites have the lowest interlayer spacing. This result cannot explain the observed height variation in Figure 2-3.

To account for our experimental observation, we must consider additional 3D reconstruction of the moiré heterostructure. Recent studies have suggested that 3D reconstruction of TMD moiré superlattices may be significant(*67*), but there have been no *ab initio* simulations of this effect. Our *ab initio* simulations of the WSe_2/WS_2 heterostructure reveal a strong moiré superlattice reconstruction that includes both a large in-plane strain distribution and a prominent out-of-plane buckling. Figure 2-5A shows the calculated in-plane strain distribution within the WSe_2 layer of the heterostructure. The heterostructure tends to increase the area of the interlayer locked AB stacking regions due to its lower energy than AA stacking. As a result, the WSe_2 layer gets locally compressed at the AB stacking regions due to its larger lattice constant compared with WS_2. The residual tensile strain localizes to the AA stacking region (Figure 2-5A). The WS_2, with smaller lattice constant, hence, has the opposite strain distribution. To partially release this strain, the hetero-bilayer reconstructs in 3D by an in-phase buckling in the out-of-plane direction (Figure 2-1A and Figure 2-1B). The simulated height distribution of the top WSe_2 layer (Figure 2-5B) perfectly reproduces our STM image (Figure 2-3A and Figure 2-3B). Figure 2-5C shows a side view of the 3D reconstructed heterostructure from both experiment and theory. The buckling above the AA "valley" causes the AB sites to rise. It is noteworthy that the presence of a hBN substrate only slightly reduces the buckling effect (black curves in Figure 2-5C). The simulated line profile agrees well with our experimental data (Figure 2-5C).

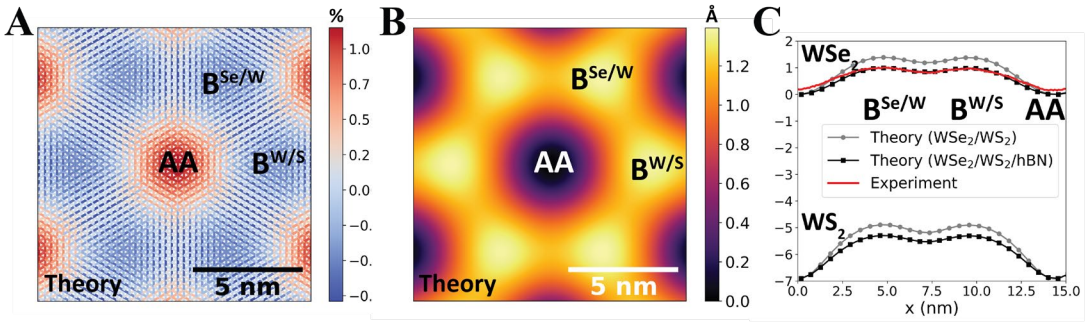

Figure 2-5 Buckling effect induced by an in-plane strain field in the WSe_2/WS_2 heterostructure. **A**. Theoretical in-plane strain distribution (in %) for the WSe_2 layer from simulation. **B**. Theoretical height profile of the W atoms in the top WSe_2 layer from simulation. **C**. Calculated 3D buckling of the heterostructure and comparison to experiment. Black and gray dots show the simulated positions of W atoms for a freestanding heterostructure and a heterostructure supported by hBN, respectively. Red trace shows the experimental line-cut from Figure 2-3B.

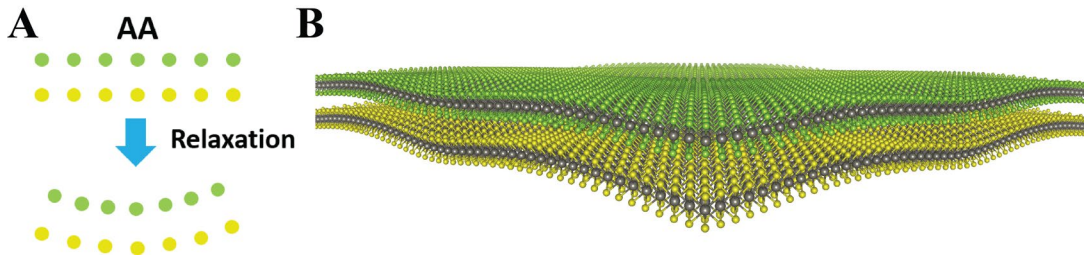

Figure 2-6 Three-dimensional reconstruction of the moiré superlattice. **A**. Schematic of the buckling process. **B**. 3D view of the reconstructed WSe2/WS2 moiré superlattice from simulation.

2.4 Electronic Structure: Spatially localized Moiré Flat Bands

The moiré superlattice reconstruction has a profound impact on the electronic structures of this moiré heterostructure. To observe this effect, we used STS to probe the local electronic structure of the WSe_2/WS_2 heterostructure. Figure 2-7 displays the STS dI/dV spectra acquired at different moiré sites for -3 V < V_{Bias} < 2V. Differences are seen in the spectra obtained at different moiré sites, consistent with previous studies performed on bilayer heterostructure grown on graphite(*16, 56*).

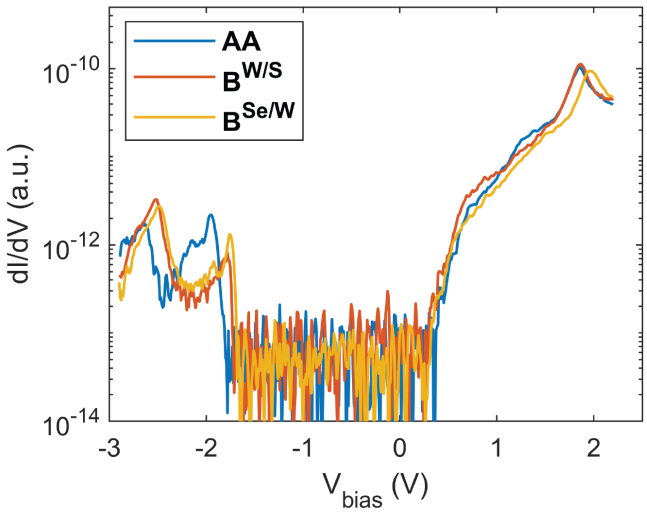

Figure 2-7 Scanning tunneling spectra measured at different stacking sites. Blue: AA staking. Red: $B^{W/S}$ stacking. Yellow: $B^{Se/W}$ stacking. Peaks in the -2V < Vbias < -1.7V range show strong moiré site-dependent peak positions. A low current setpoint is used here (V_{bias}=-3V, I=70pA).

We first focus our analysis of the STS spectra on the moiré flat band closest to the valence band edge, where the effects of strongly correlated states have been observed previously(*18, 47, 48*). A challenge in the STM study of TMD materials is how to distinguish electronic states arising from K or Γ points in the single-layer BZ(*55, 56*). Here we utilize two distinct features of the K-point states to identify them as discussed in details below.

We first use the fact that, due to the much larger in-plane momentum of K-point states, their wavefunction decays faster outside the TMD layer. It can be described by Eq. (2.1):

$$\boldsymbol{k}_{||}^2 - \boldsymbol{\kappa}^2 = \frac{2m_e(E - E_g)}{\hbar^2}, \tag{2.1}$$

where $\boldsymbol{k}_{||}$ is the in-plane wavevector, $\boldsymbol{\kappa}$ is the decay constant in the out-of-plane direction, m_e is the electron/hole effective mass, E is the electron/hole energy, and E_g is the energy of the band edge. This should result in a much faster dI/dV signal decay rate with increased tip-sample distance for K-point states. Figure 2-8A shows the height dependent dI/dV spectra measured at one of the AB sites (ultimately confirmed as $B^{Se/W}$ site) in the moiré pattern. Two prominent peaks are observed near V_{bias} = -1.7 V and V_{bias} = -1.5 V. The peak near -1.5 V exhibits a much stronger height dependence than the peak near -1.7V, suggesting that the peaks at -1.5 V and -1.7 V correspond to electronic states at the K and Γ points, respectively.

We next use the two facts that the TMD K-point electron wavefunctions have large in-plane momentum, and are mainly contributed by W *d* orbital with angular momentum m = $\pm$ 2. As a result, these states gain a $4\pi/3$ phase when rotated by a $2\pi/3$ angle in

space (-$4\pi/3$ phase gain for K' state). Second, due to the plane wave part $e^{i\boldsymbol{k}\cdot\boldsymbol{r}}$ of the Bloch wave, there will be a 2π phase winding for adjacent three W atoms (illustrated in Figure S9a). There phase factors, together, will induce atomic-scale alternating constructive and destructive interference pattern in the LDOS maps of the K(K')-point states. If we take the K-point state as an example, at the hollow circle points shown in the left panel in Figure 2-8B, the contribution of their nearby three adjacent W atoms will be,

$$1 \cdot 1 + e^{\frac{2\pi i}{3}} \cdot e^{-\frac{4\pi i}{3}} + e^{\frac{4\pi i}{3}} \cdot e^{-\frac{8\pi i}{3}} = 0, \tag{2.2}$$

where the first factor in each term in the left-hand-side of the equation is the phase from the Bloch wave, while the second factor is from the angular momentum. Therefore, we will have destructive interference at the hollow circle points. For the solid circle points, the phase contribution from the Bloch wave keeps the same while the phase contribution from the angular momentum is reversed. The net effect will be,

$$1 \cdot 1 + e^{\frac{2\pi i}{3}} \cdot e^{\frac{4\pi i}{3}} + e^{\frac{4\pi i}{3}} \cdot e^{\frac{8\pi i}{3}} = 3. \tag{2.3}$$

Therefore, we will have constructive interference at the solid circle points. For the K'-point state, both the wave vector of the Bloch wave and the angular momentum of the *d* orbital are reversed, inducing that the final interference pattern is the same as the one of the K-point state. On the other hand, the Γ-point states are mainly contributed by the p_z orital of the Se atoms, which has m = 0, and its Bloch wave has 0 wave vector. Therefore, all sites share the same phase and only have constructive interference (right panel in Figure 2-8B), which will make the LDOS spatial distribution of the Γ-point state smoother than the that of the K-point states. Experimentally, we found the high-resolution dI/dV mapping at -1.5 V shows pronounced dI/dV signal oscillation over atomic-scale distances that match the WSe_2 lattice (Figure 2-8C), while the dI/dV mapping at -1.7 V more smoothly varies (Figure 2-8D). This behavior confirms that the -1.5 V peak originates from K-point states at the valence band edge, whereas the -1.7 V peak originates from Γ-point states. Such analysis based on the dI/dV mapping spatial oscillation amplitude is also supported by the numerical calculation results(*64*).

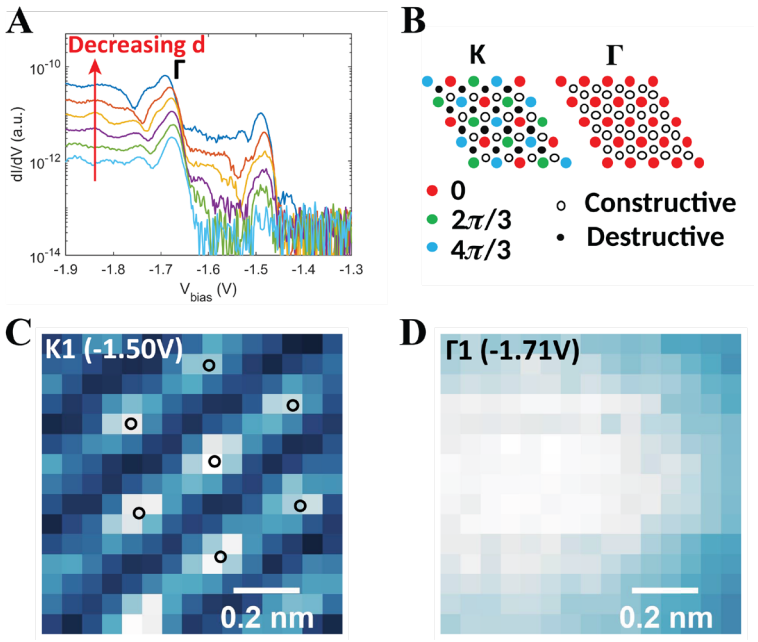

Figure 2-8 Resolving moiré flat bands folded from different points in in the unit-cell Brillouin zone. **A**. Tip-sample distance (d) dependent STS at the $B^{Se/W}$ site (V_{bias} = -2.15V, I=50, 100, 200, 400, 800, 1600pA). A second peak near V_{bias} = -1.5V emerges with decreased d, indicating that it has a larger decay constant and originates from K-point states. **B**. Illustration of the atomic-scale wavefunction interference pattern. K-point states have a 2π phase-winding over adjacent three W atoms, while Γ-point states have identical phases over all Se atoms sites. **C,D**. High resolution dI/dV mappings measured at the same $B^{Se/W}$ region with biases corresponding to (**C**) the K-point (-1.50V) and (**D**) the Γ-point (-1.71V) peaks. Black hollow circles in e show the atomic-scale constructive interference points as illustrated in (**A**).

Next we performed larger-scale dI/dV mapping to directly visualize the localization of the flat bands in the real-space. Figure 2-9A and Figure 2-9B show dI/dV maps obtained at the two peak energies -1.52 V (labeled K1) and -1.73 V (labeled Γ1). The local density of states (LDOS) for both of these flat band states are found to be strongly localized at the $B^{Se/W}$ site. Atomic-scale site dependence in the dI/dV signal for K-point states is again reflected in the K1 dI/dV mapping. Figure 2-9C and Figure 2-9D show the dI/dV mapping at slightly lower energies. The LDOS distribution is seen to change dramatically and now shows LDOS minima where previously there were maxima at the $B^{Se/W}$ site.

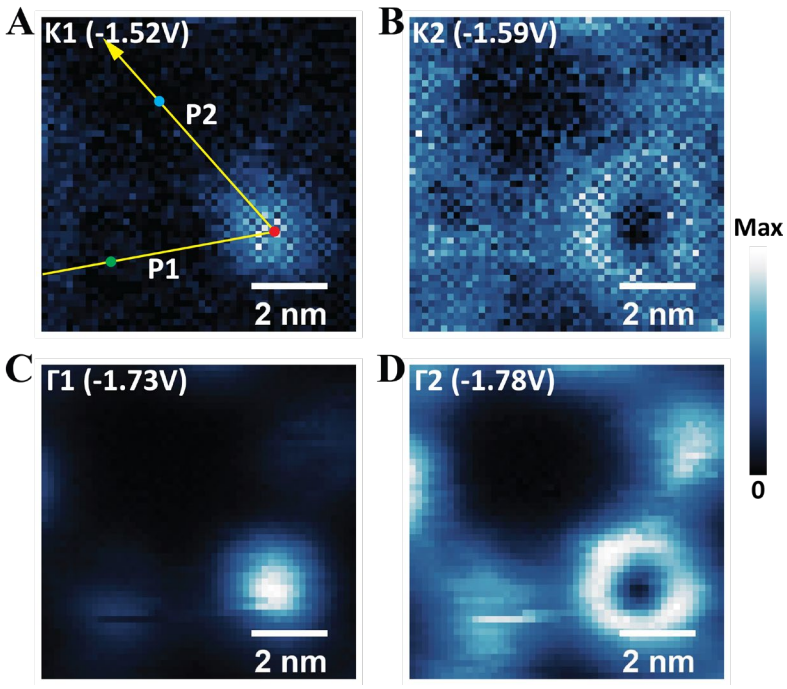

Figure 2-9 Imaging moiré flat bands. **A,B**. Large scale dI/dV mappings of K-point states for (**A**) V_{bias} = -1.52V and (**B**) V_{bias} = -1.59V. **C,D**. Large scale dI/dV mappings and Γ-point states for (**C**) V_{bias} = -1.73V and (**D**) V_{bias} = -1.78V.

To better determine the energy-dependent LDOS of the moiré flat bands, Figure 2-10A shows a density plot of dI/dV spectra for the bias range -1.72V < V_{bias} < -1.42 V along the $B^{W/S}$-$B^{Se/W}$-AA direction, indicated by the yellow path marked in Figure 2-9A. Figure 2-10B shows the same plot, but over a different bias range: -1.86 V < V_{bias} < -1.63V. Figure 2-10A shows a prominent moiré flat band at the valence band minimum that is strongly localized at the $B^{Se/W}$ site. This K-point moiré flat band is isolated from deeper moiré flat bands by a gap of ~50 meV. Figure 2-10C displays a high-resolution dI/dV spectum at the $B^{Se/W}$ site which exhibits a peak having a full width at half maximum (FWHM) of 12mV ± 1mV. After a deconvolution eliminating the impact of the modulation voltage (using 5meV FWHM Gaussian kernel to approximate the modulation voltage), the FWHM of the dI/dV peak is 10mV ± 1mV, which sets an upper limit on the bandwidth of the moiré flat band of WSe_2/WS_2. The occupied moiré miniband in twisted bilayer graphene by comparison has an experimental bandwidth of 10~40 meV(*21, 53, 54, 68*). The narrowness of the WSe_2/WS_2 moiré flat band in combination with the strong long-range Coulomb interactions in 2D semiconductors makes this TMD heterostructure an excellent platform to explore highly correlated quantum phenomena.

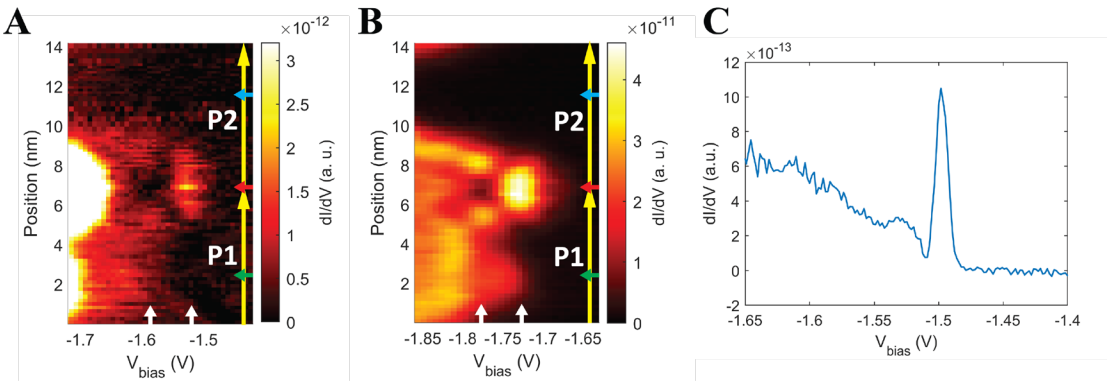

Figure 2-10. Spatial characteristics of different moiré flat bands. **A**,**B**. dI/dV density plot of (**A**) K-point and (**B**) Γ-point states along the two-segment yellow path shown in Figure 2-9A. Horizontal arrows label the positions of the $B^{W/S}$ (green), $B^{Se/W}$ (red) and AA (blue) sites. White vertical arrows label the energies used in Figure 2-9. V_{BG}=50V for all measurement shown. The tip-sample distance is determined by the setpoint V_{bias} = -2.15V, I=800pA for all spectroscopies shown. Lock-in modulation = 20mV. **C**. High-resolution dI/dV spectrum measured at the $B^{Se/W}$ site. A sharp peak with full width at half maximum (FWHM) of 12mV ± 1mV can be observed near V_{bias} = -1.5 V (uncertainty in the FWHM of this peak comes from the standard deviation of widths extracted from spectra obtained at different $B^{Se/W}$ sites). Lock-in modulation = 5mV

In addition to the valence band edge moiré flat band, Figure 2-10A shows that deeper moiré flat bands having different wavefunction spatial characteristics are present, but these bands are not well isolated. One such flat band can be tentatively identified near -1.6 V in Figure 2-9B. The dI/dV map of this flat band (labeled K2) shows a ring around the center of the $B^{Se/W}$ site and a weak plateau at the $B^{W/S}$ site. The ring-shaped electron wavefunction around the $B^{Se/W}$ site is reminiscent of the first excited states of a harmonic oscillator for a potential well centered on this site.

Figure 2-10B shows deeper flat bands mostly originating from the Γ point. The Γ point moiré flat band closest to the valence band edge lies at -1.73 V and is localized to the $B^{Se/W}$ site. At the slightly deeper energy of -1.78 V a new wavefunction distribution is seen and the LDOS now shows a minimum at the $B^{Se/W}$ site (Figure 2-9D). The ring-shaped electron wavefunction around the $B^{Se/W}$ site in this case is once again reminiscent of the first excited states of a harmonic oscillator.

2.5 Origin of Moiré Potential

Although we directly observed the moiré flat bands and its spatial characteristics, it is still desirable to figure out their microscopic origins. To achieve this, we performed large-scale density functional theory (DFT) calculations on the forcefield-reconstructed moiré superlattice. Figure 2-11A shows the calculated valence band structure for the WSe_2/WS_2 moiré superlattice in the mini-BZ (left) and the corresponding plot of the density of states (DOS) (right). The valence band edge is set at E = 0. The bands closest to the valence band edge (0 ~ -0.18eV) are folded from the K-point, whereas the deeper bands below -0.18 eV have mixed origins from both the K-point and the Γ-point. Their

origins can be distinguished by their LDOS distributions in the out-of-plane direction. Figure 2-12 shows the planar-averaged plot of the charge density of representative flat band states arising from the K and Γ point. The K point states do not hybridize between the layers and are well localized in the WSe_2 layer. The Γ point states, on the other hand, are strongly hybridized between the layers and hence have charge density on both layers.

We labeled four important energy ranges (E1-E4) in Figure 2-11A. The top-most valence band (within E1) has a bandwidth of only ~10 meV and is separated from the next band (within E2) by ~30 meV. The narrow, energetically isolated nature of the top-most band is in quantitative agreement with our experimental observations (Figure 2-10C). The deeper bands tend to mix with each other and are thus hard to distinguish experimentally. The top-most bands folded from the Γ-point is within E3, while the next set of deeper bands are within E4. The states in the gap between E3 and E4 are folded from the K-point.

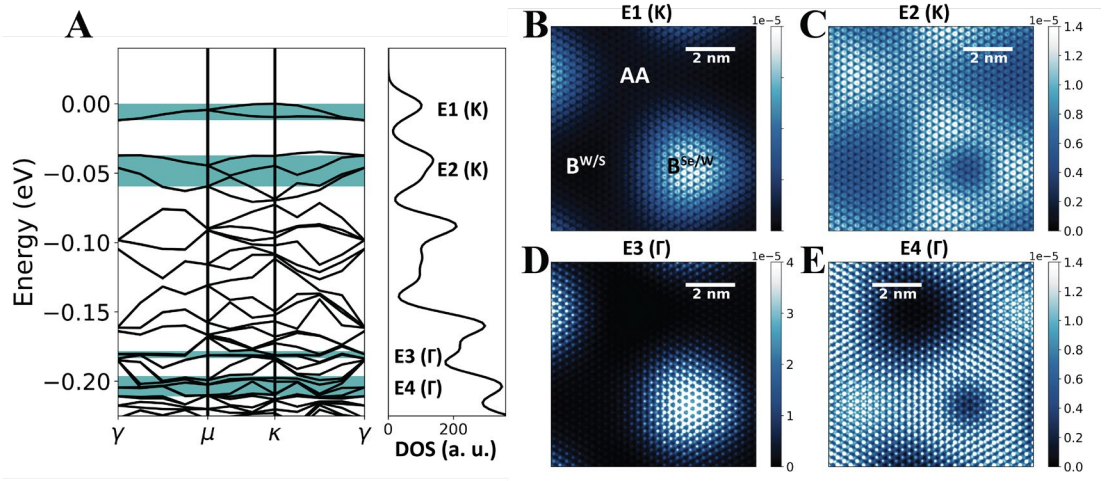

Figure 2-11 *Ab initio* calculations of the electronic structure in reconstructed moiré. **A**. Calculated electronic band structure plotted in the folded mini-BZ (left) and the corresponding plot of the density of states (DOS) with 10 meV Gaussian broadening (right). Four important energy ranges (E1-E4) are labeled (green shaded areas) to highlight the top-most states folded from the K-point (E1, E2) and Γ-point (E3, E4). **B-E**. Calculated LDOS maps over a patch of area corresponding to the region used for dI/dV maps in Figure 2-9. The LDOS maps are averaged over different energy ranges as labeled in panel A: **B**. E1, originating from K-point, **C**. E2, originating from K-point, **D**. E3, originating from Γ-point, and **E**. E4, originating from Γ-point. The maps are also averaged over the out-plane direction.

The spatial distribution of the calculated charge density for the flat band states agrees well with the STS results. Figure 2-11B-E show the calculated LDOS distribution averaged over the four different energy ranges E1-E4, as well as averaged over the out-of-plane direction. Figure 4b shows the calculated LDOS for E1, mainly the top-most flat band from the K-point. The LDOS is observed to localize strongly in the $B^{Se/W}$ region of the moiré unit cell. This matches the experimental behavior quite well (Figure 2-9A), and, in fact, allows us to distinguish the $B^{Se/W}$ region from the $B^{S/W}$ region in our experimental images. As we move deeper into the valence bands (E2) our simulation

reveals a delocalization of the K-point LDOS and the formation of a node at the center of the $B^{Se/W}$ region (Figure 2-11C). This closely matches our experimental observations (Figure 3h). The Γ-point LDOS behaves similarly, as seen by the comparison of theoretical Figures 4d,e with experimental Figure 2-9C,D. Once again, we see the top-most Γ-point states (E3) showing strong localization in the $B^{Se/W}$ region, as well as increased delocalization accompanied by the formation of a node at slightly deeper energies (E4). The calculated energy separation between the top-most K and the Γ states (180 ± 20 meV between E1 and E3) is also very similar to the experimental energy separation between the K1 and Γ1 states (205 ± 18 meV). We thus observe very reasonable agreement between experiment and theory for both the flat band energy separation and the flat band spatial LDOS distribution.It is conventionally believed that the interlayer interaction variation is the dominant effect in modulating the electronic structure of moiré superlattices(*50*). However, our DFT calculation reveals that the flat bands at the K-point are mainly a result of the deformation of the monolayer instead of a hybridization-induced interlayer potential. Similar K-point flat band behavior can be reproduced by calculating the electronic structure of a puckered monolayer WSe_2 extracted from the relaxed moiré superlattice (as shown in Figure 2-13). The Γ-point flat bands, on the other hand, do arise from inhomogeneous interlayer hybridization within the moiré superlattice. The difference mainly originates from the fact that the K-point wavefunctions, being of W-*d* character, are highly localized within the WSe_2 layer and almost do not hybridize in the bilayer, while the Γ-point wavefunctions, on the other hand, have a strong Se-p_z character, leading to a stronger interlayer hybridization(*69, 70*). The spatial varying interlayer spacing (larger at AA sites and smaller at AB sites) causes inhomogeneous interlayer hybridization for Γ-point states and thus the splitting of the Γ-point bands at different moiré sites(*71, 72*).

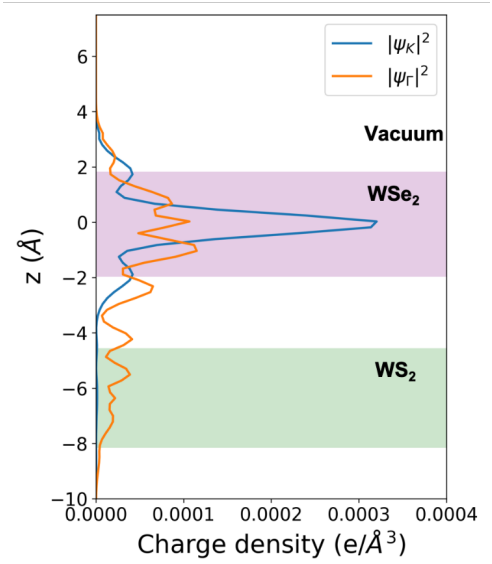

Figure 2-12 Comparison of the charge density of states arising from the K and Γ points. Planar-averaged charge density of moiré flat band states folded from the G and K valleys,

respectively. The charge density of the K state is strongly localized on the WSe_2 layer while the Γ state is present on both layers because of hybridization. The WSe_2 layer and WS_2 layer regions are labeled with purple and green respectively.

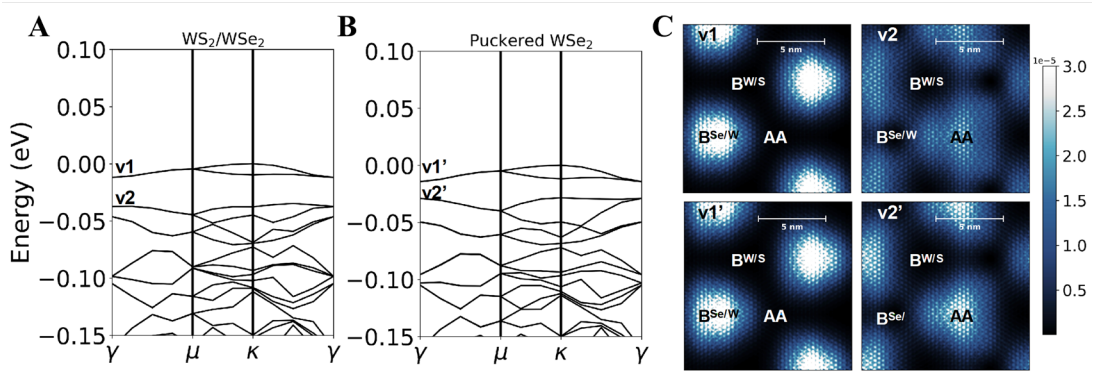

Figure 2-13 Comparison of the electronic structure of a reconstructed WS_2/WSe_2 hetero-bilayer and an isolated puckered WSe_2 monolayer. **A,B**. Comparison of the electronic band structures for (**A**) a relaxed WSe_2/WS_2 heterostructure and (B) an isolated puckered WSe_2 monolayer. The geometry of the puckered WSe_2 monolayer is extracted from the reconstructed hetero-bilayer moiré superlattice. **C**. Comparison of the LDOS spatial distribution of the γ-point states near the valence band edge marked in (**A**) and (**B**). The LDOS maps are averaged over the out-plane direction.

2.6 Summary and Outlook

In this chapter, we explored the atomic and electronic structures of a WSe_2/WS_2 moiré heterostructure. We found that 3D moiré reconstruction dominates the low-energy moiré electronic structure, resulting in a narrow moiré flat band with 10 meV bandwidth at the valence band maximum in WS_2/WSe_2 heterostructures. Such quantitative understanding of the atomic and electronic structure within a moiré superlattice is crucial for simulating Hubbard model and for further control of novel correlated phenomena in TMD-based moiré heterostructures.

3 Imaging local discharge cascades for correlated electrons in WS2/WSe2 moiré superlattices

3.1 Introduction and Background

Compared with graphene-based moiré heterostructures, semiconductor TMD moiré superlattices feature flatter moiré minibands and stronger long-range Coulomb interactions, thus leading to new emergent correlated electronic states that are absent in graphene-based moiré systems(*16, 41-43, 45, 46*). Indeed, several recent studies have revealed correlated states in TMD moiré superlattices, including charge-transfer insulator states(*53, 68*) and a rich variety of extended Wigner crystal states at fractional fillings(*48, 73-75*). Direct local characterization of the correlated states and physical parameters of the extended Hubbard model in TMD moiré heterostructures, however, has so far been lacking. In Chapter 2 we performed a local probe of the lattice and orbitals in the WSe_2/WS_2 moiré heterostructure that host interacting electrons. However, the role of electron interactions, an important factor in shaping the strongly correlated physics in such systems, has not been discussed yet. For example, little is known about the strength of nearest-neighbor electron-electron interactions or the magnitude of inhomogeneity in onsite energies within TMD moiré superlattices.

In this chapter, we describe a new STM-based technique for imaging and manipulating the charge states of correlated electrons in gated WS_2/WSe_2 moiré superlattices that enables the determination of the nearest-neighbor Coulomb interaction energies and onsite energy fluctuations. Using this we are able to image the charge state of moiré sites via their influence on the tunneling current between an STM tip and the WS_2/WSe_2 heterostructure. By combining a back-gate voltage with the STM bias this mechanism enables us to locally charge and discharge correlated moiré electrons. Gradually ramping the STM bias under these conditions results in a cascade of discharging events for correlated electrons at multiple neighboring moiré sites. Investigation of this discharge cascade allows us to determine the nearest-neighbor Coulomb interactions as well as onsite energy fluctuations within the moiré superlattice.

The work in this chapter, as a natural extension of the last chapter, is finished through a close collaboration between the Wang and Crommie group. The STM work was mainly done by Shaowei and me while the theoretical calculation was done by Mit in the Louie group. Part of the discussion is also presented in a published paper(*76*).

3.2 Local Discharging of Moiré Electrons by an STM Tip

We first characterized our gated WSe_2/WS_2 heterostructure via scanning tunneling spectroscopy (STS) under various charge carrier densities. Figure 3-1A and Figure 3-1C show plots of the differential conductivity (dI/dV) at the $B^{Se/W}$ and $B^{W/S}$ sites respectively as a function of both the STM tip bias V_b (for convenience, the STM tip bias notation is changed to V_b in chapter 3) and backgate voltage V_g. Here we focus on the electron-

doped regime of the moiré heterostructure at positive V_g, with the Fermi level located in the conduction band. The dI/dV spectra show negligible signal for $0 < V_b < 0.4$V due to very small tunneling probability to conduction band-edge states which lie at the K point of the bottom WS_2 layer and which feature a large out-of-plane decay constant(*64, 77*). At $V_b > 0.4$ V tip electrons can more readily tunnel into the conduction band Q-point states which protrude further into the vacuum.

In addition to a general increase in dI/dV signal for $V_b > 0.4$ V, we observe sharp dispersive dI/dV peaks at the different moiré sites (the bright features labeled by blue arrows in Figure 3-1A and Figure 3-1C). These dispersive peaks can be more clearly observed in the density plot of the second order derivative (d^2I/dV^2), as shown in Figure 3-1B and Figure 3-1D. To better understand the origin of these peaks we performed 2D dI/dV mapping at STM bias voltages of $V_b = 0.775$ V (Figure 3-2A) and $V_b = 0.982$ V (Figure 3-2B) for a fixed gate voltage of V_g=45V. In these images, the dispersive dI/dV peaks in Figure 3-1A and Figure 3-1C correspond to periodic circular rings surrounding the $B^{Se/W}$ sites that expand upon increased V_b. This behavior can be explained by discrete charging and discharging events for localized moiré electrons at the $B^{Se/W}$ sites, controlled by the application of V_g and V_b, as discussed below.

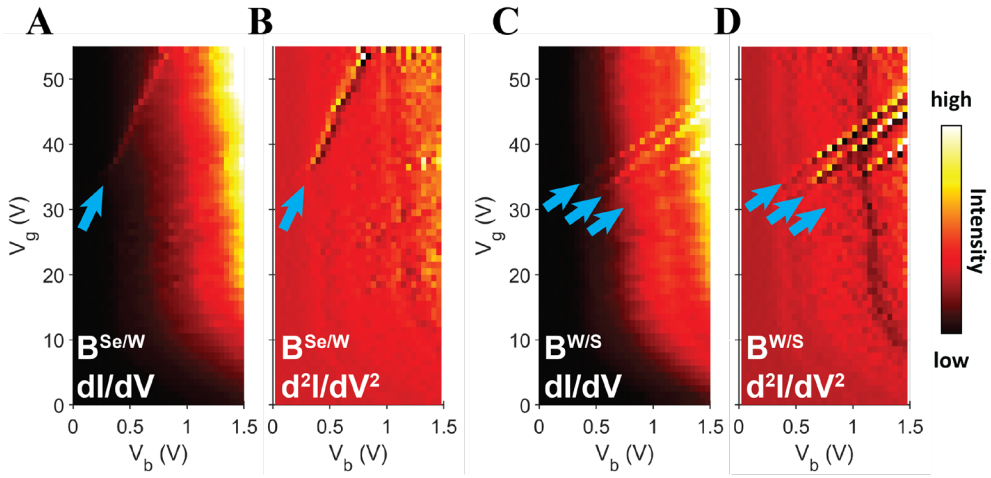

Figure 3-1. Gate-dependent dI/dV spectra measured at different stacking sites. **A**. $B^{Se/W}$ site, and **C**. $B^{W/S}$ site. The bright dispersive features labeled by blue arrows correspond to tip-induced charging/discharging of electrons at adjacent $B^{Se/W}$ moiré sites. To highlight the dispersive feature, the corresponding second order derivative (d^2I/dV^2) spectra are plotted in (**B**) and (**D**), respectively.

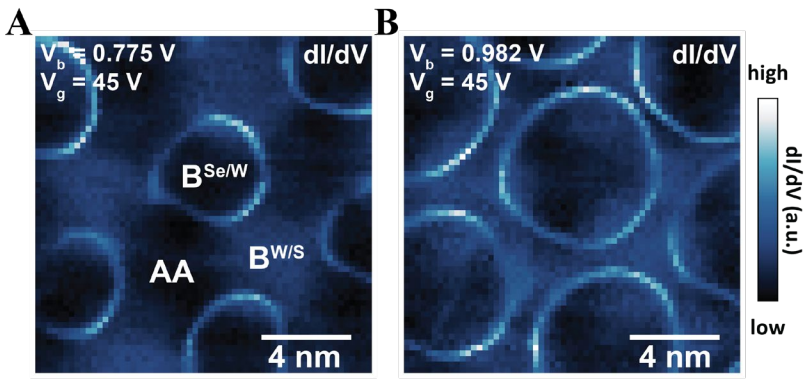

Figure 3-2 dI/dV mapping of the WSe_2/WS_2 moiré superlattice. **A**. V_b = 0.775 V, V_g = 45 V and **B**. V_b = 0.982 V, V_g = 45 V. The tip-sample distance for the dI/dV mappings is controlled by the setpoint: V_b = -3V, I = 100 pA. Discharge of the moiré electron causes a dI/dV peak which appears as a circular ring surrounding each $B^{Se/W}$ site in the moiré superlattice. The periodic discharging rings expand with V_b.

The STM tip plays two roles in the discharging events: (1) First, it acts as a source electrode for the tunneling current between the tip and the heterostructure, thereby injecting electrons into the excited states of the conduction band. (2) Second, it acts as a local gate that can change the charge state of conduction band edge states localized at $B^{Se/W}$ moiré sites (illustrated in Figure 3-3). The gain or loss of an electron at a $B^{Se/W}$ moiré site modifies the electron tunneling rate between the STM tip and the heterostructure surface due to the resultant change in Coulomb potential. Charging and discharging events at the $B^{Se/W}$ sites thus lead to a corresponding jump in the STM tunneling current and result in sharp peaks in the dI/dV spectra. Similar ring-like charging behavior has been seen via STM in other nanoscale systems(*39, 78-81*).

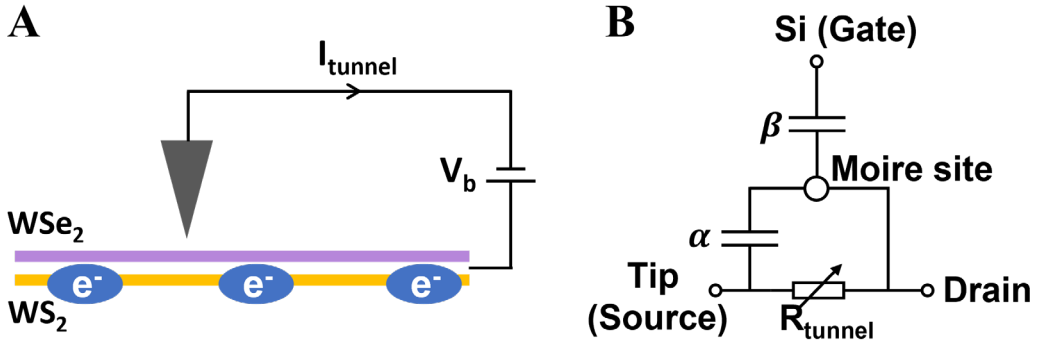

Figure 3-3 Mechanism of the discharging events. **A**. Illustration of the experimental setup (back gate not plotted here). The WSe_2/WS_2 moiré heterostructure is electron doped with localized electrons confined in the bottom WS_2 layer. The STM tip bias voltage V_b has two effects on the heterostructure: (1) It acts as a source electrode for the tunneling current between the tip and the heterostructure, where electrons are injected to the excited states in the conduction band. (2) It acts as a local gate that can change the charge state of the localized electrons at the conduction band edge of the moiré heterostructure, which is

confined to the WS_2 layer. The charging state of the localized electrons in the WS_2 layer will affect the tunneling current between the tip and the TMD heterostructure through the Coulomb interaction. **B**. The effective circuit model showing the dual role played by the tip, which gates the moiré electron in the WS_2 layer and drives the tunneling current. The charge distribution of the moiré electron will affect the local tunneling current via its induced Coulomb potential.

Ab initio calculations show that the WSe_2/WS_2 moiré flat band states at the conduction band edge are strongly localized at the $B^{Se/W}$ sites in real space (see Figure 3-4). For $V_g > 25V$, the moiré global filling factor n/n_0 is greater than 1, where n is the gate-controlled carrier density and n_0 is the carrier density corresponding to a half-filled moiré miniband with one electron per moiré lattice site. At this gate-voltage there is thus at least one electron localized at each $B^{Se/W}$ site. At positive sample bias, V_b, negative charge accumulates at the tip and repels nearby electrons, thus causing electrons localized to $B^{Se/W}$ sites to discharge when V_b exceeds a threshold value (see the sketch in Figure 3-5). The efficiency with which the STM tip discharges nearby localized electrons depends sensitively on their distance to the tip, and thus results in circular discharging rings for a given V_b (Figure 3-2B). These rings expand continuously with increased V_b since larger V_b enables the discharge of localized electrons at larger tip-electron distances (Figure 3-2B). When the tip is inside a discharge ring the circled moiré site is empty whereas it contains an electron when the tip is outside the ring.

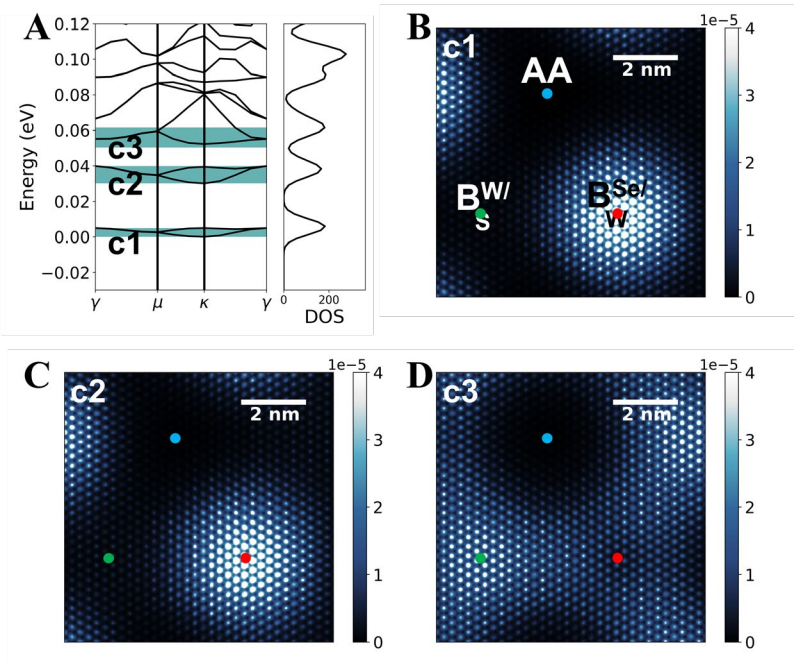

Figure 3-4 DFT calculation of the WS_2/WSe_2 conduction flat bands. **A**. DFT-calculated band structure for the conduction bands and the corresponding density of the states (DOS). The three lowest-energy flat bands are labeled c1, c2 and c3, respectively. **B-D**. Distribution of the local density of states for (**B**) c1, (**C**) c2, and (**D**) c3. Each map is integrated over the energy range indicated by the corresponding green stripe shown in A.

The three stacking types (AA, $B^{Se/W}$, and $B^{W/S}$) are labeled in the maps. The lowest-energy flat band (c1) is localized at the $B^{Se/W}$ site.

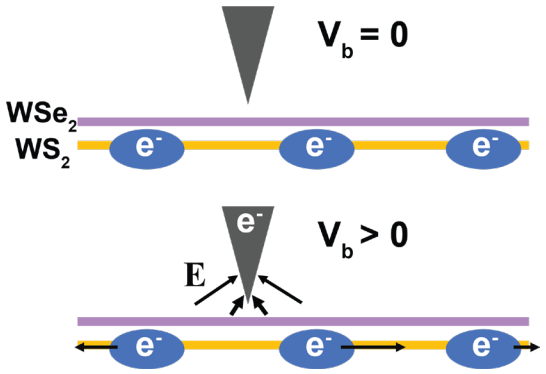

Figure 3-5 Sketch of tip-induced moiré electron discharging. The STM tip acts as a local top gate that modifies the electron energy at nearby $B^{Se/W}$ moiré sties and discharges them for bias voltages greater than a local threshold value.

3.3 Cascade Discharging of Multiple Correlated Electrons

The STM tip can discharge multiple correlated electrons at neighboring moiré sites in a cascade fashion with increased V_b, thus providing a powerful tool to probe electron correlation in moiré systems. We have systematically examined the discharge cascade of correlated electrons in a WSe_2/WS_2 flat-band by performing 2D dI/dV mapping of the moiré pattern as a function of V_b. Figure 3-6 shows the evolution of discharge rings as V_b is increased from 0.57 V to 1.25 V for fixed V_g = 52 V. The discharge rings expand with increased V_b and begin crossing each other at V_b = 0.66 V. Near a crossing point, the STM tip couples effectively to multiple adjacent moiré sites and can generate a cascade of discharging events. Intricate new patterns emerge as the rings cross each other with increasing V_b. These patterns differ distinctly from a simple superposition of ever-increasing rings as expected from a non-interacting picture, thus providing a manifestation of electron correlation in TMD moiré superlattices.

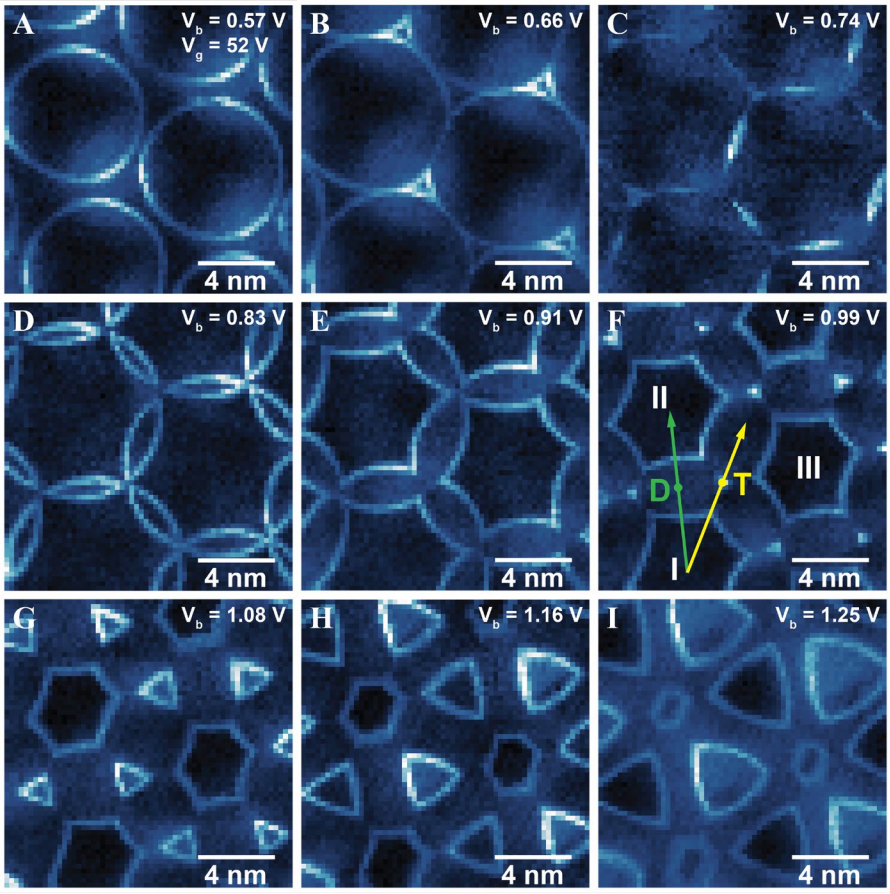

Figure 3-6 Discharging correlated electrons. **A-I**. Evolution of moiré discharging rings with increasing sample bias V_b (gate voltage fixed at V_g = 52 V). The rings expand with increased V_b and intricate new patterns emerge when they cross each other. The complex patterns indicate discharging cascades of multiple correlated electrons in neighboring moiré sites. dI/dV spectra along the green and yellow lines in (**F**) are shown in Figure 3-8. Here D and T denote the 2-ring and 3-ring crossing points, respectively. dI/dV mapping setpoint: V_b = -3V, I = 100 pA, V_g = 52 V. (T = 5.4 K).

The effects of electron correlation on cascade discharging can be more effectively visualized in position-dependent dI/dV spectra. Figure 3-8A shows position-dependent dI/dV spectra along the green line in Figure 3-6F. This line passes through a high-symmetry 2-ring crossing point (marked D) which is equidistant to neighboring $B^{Se/W}$ sites I and II. For positions near D sites I and II are both occupied at low V_b (i.e., $n = 2$ where n is the total electron count for adjacent moiré sites). As V_b increases, however, the tip successively discharges the two sites and n changes from 2 to 1 and then from 1 to 0 as V_b crosses two dI/dV discharge peaks. At D one would expect by symmetry that these two discharging events should occur at the same value of V_b for a non-interacting picture. The data of Figure 3-8A, however, show that these two discharging events occur at different V_b values, with a discharging gap of $\Delta V_b^D = 122 \pm 9$ mV (obtained via high-resolution dI/dV spectra measured at the discharging ring crossing points, as shown in Figure 3-7A).

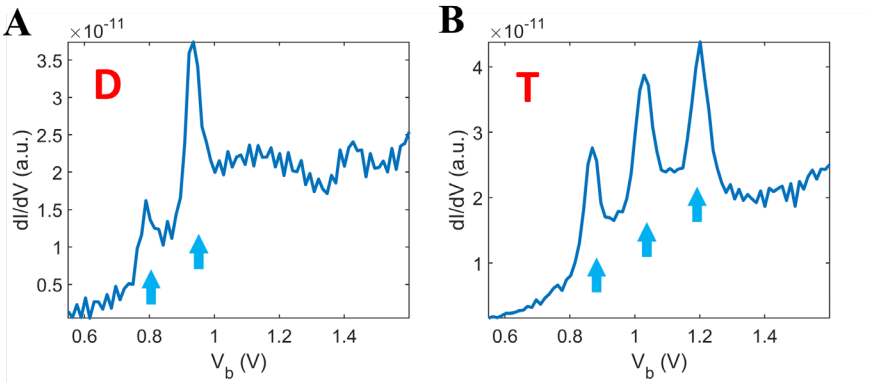

Figure 3-7 High-resolution dI/dV spectra measured at the discharging ring crossing points. **A**. T point, **B**. D point. The cascade discharging peaks are labeled with blue arrows. V_b step size < 14 mV.

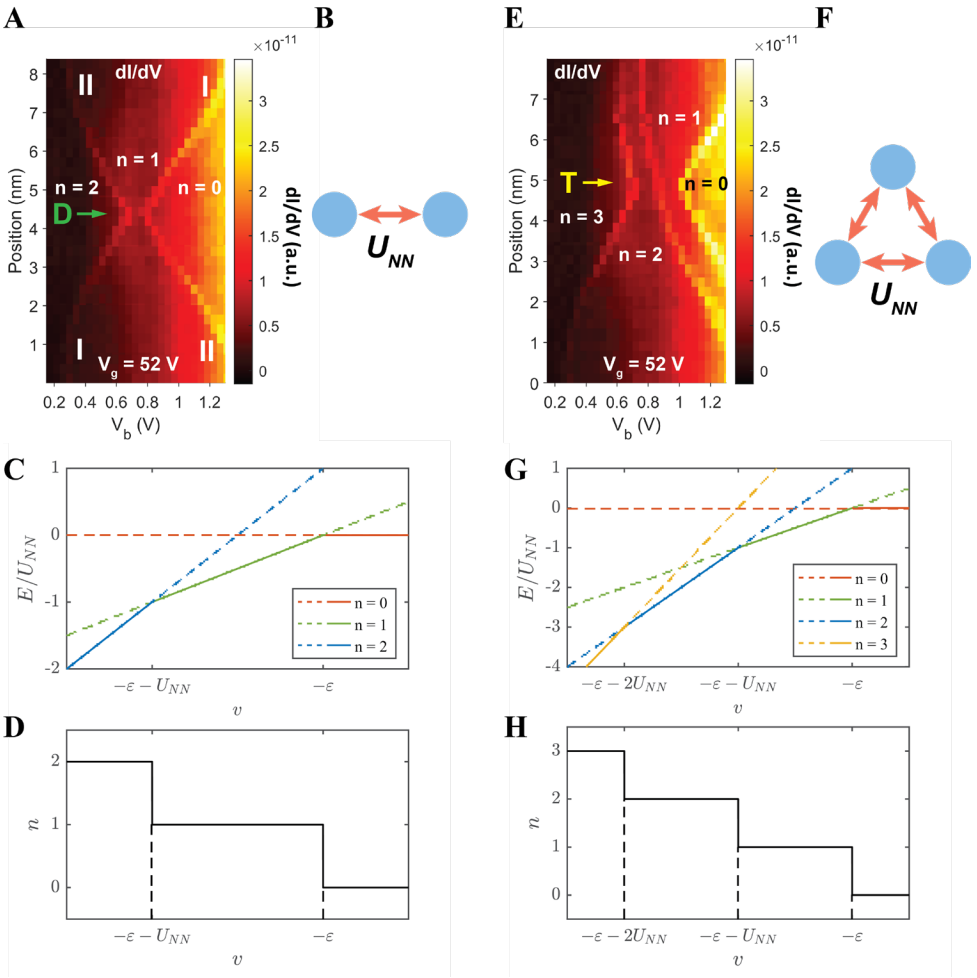

Figure 3-8 Correlation effects on cascade discharging of moiré sites. **A**. Position-dependent dI/dV spectra along the green line shown in Figure 3-6F which passes through D. dI/dV peaks indicated by bright lines correspond to discharging events where the total electron number decreases from 2 to 1 and from 1 to 0 from left to right. I and II indicate

the moiré sites being discharged as labeled in Figure 3-6F. **B**. Sketch of simplified 2-site cluster model for analysis of discharge behavior at D. U_{NN} indicates the nearest-neighbor Coulomb interaction. **C**. Calculated energy levels and (**D**) total electron number (n) of cluster ground state as a function of v for the 2-site model. States with different electron number are labeled by color. The discrete changes of n in D correspond to discharge peaks at B. **E**. Position-dependent dI/dV spectra along the yellow line shown in Figure 3-6F. This line cut passes through T. Bright lines indicate discharging events at three distinct bias voltages. **F**. Sketch of simplified 3-site cluster model for analysis of discharge behavior at T. **G,H**. Calculated energy levels (**G**) and total electron number (**H**) of cluster ground state as a function of v for the 3-site model.

Similar behavior can be seen at another high symmetry point, marked T in Figure 3-6F. Here the STM tip is equidistant to three neighboring $B^{Se/W}$ sites marked I, II, and III, and so the discharge cascade involves three electrons. Figure 3-8E shows position-dependent dI/dV spectra along the yellow line in Figure 3-6F which passes through T. Three dI/dV peaks are seen in the spectra, corresponding to a cascade of three discharging events that decrease the total number of electrons (n) in sites I-III from 3 to 2 to 1 and then, finally, to 0. At T we observe the voltage difference between the 3→2 and 2→1 discharge peaks to be identical to the difference between the 2→1 and 1→0 discharge peaks within the uncertainty of our measurement: ΔV_b^T = 166 mV ± 11 mV (see dI/dV spectra shown in Figure 3-7B).

The cascade discharging and gap splitting at the D and T points directly reflect the moiré electron interactions. To see this in a more clear and quantitative way, we will need to investigate a more specific model on interacting moiré electrons, which will be discussed in the next section.

3.4 Probe the Nearest-neighbor Coulomb Interactions

In order to interpret the discharge cascade of correlated electrons in our TMD moiré system in terms of physically significant parameters, we employ a simplified N-moiré-site model that includes on-site and nearest-neighbor interactions. The Hamiltonian describing our system is

$$H = \sum_{i=1}^{N} (\varepsilon_i + v_i) n_i + \frac{1}{2} U_{NN} \sum_{<ij>} n_i n_j, \tag{3.1}$$

Here U_{NN} is the nearest-neighbor Coulomb interaction term and $< ij >$ only sums over nearest neighbors and N represents the number of moiré sites close to the tip (equals to 2 or 3 in our system). n_i is the electron number at moiré site i, ε_i is the onsite energy at site i, and v_i is the potential energy shift induced by V_b and V_g at site i. v_i has the form

$$v_i = \alpha_i \cdot eV_b - \beta_i \cdot eV_g, \tag{3.2}$$

where $e = 1.6 \times 10^{-19} C$, and α_i and β_i are dimensionless coefficients describing the electrostatic potential on site i induced by V_b and V_g, respectively. We note that α_i

depends sensitively on the tip position r_t, meaning $\alpha_i = \alpha_i(r_t)$. In this model we neglect intersite hopping due to the small bandwidth of the moiré flat band (~5meV). We also ignore on-site Coulomb interactions since the total number of electrons ($n = \sum_i n_i$) for sites near the tip is smaller than *N* and the energy of double occupancy for a single site is assumed to be prohibitively large. This Hamiltonian is meant to describe electrons in the lowest conduction band near the tip since higher-energy delocalized electrons are assumed to be swept away by tip repulsion for $V_b > 0$.

Our strategy for understanding the discharge phenomena observed here is to explore the consequences of this Hamiltonian for different electron occupation values *n*. By comparing the different total energies, E(*n*), we can identify the charge occupation, *n**, that has the lowest total energy and we assume that this is the ground state. A discharge event from the $n = n^* + 1$ state to the $n = n^*$ state occurs when $E(n^*) < E(n^* + 1)$. Since our measurements primarily involve discharging events, the largest relevant energy is U_{NN} which eclipses the energy associated with intersite hopping. As a result, the behavior induced by Eq. (3.1) can be treated within an essentially classical framework (in the context of discharge phenomena) that is adequate to extract information on the Hubbard model parameters ε_i and U_{NN} from our data, the main goal of this work.

We start by applying this model to analyze the discharge behavior that occurs when the STM tip is held at position D. Here the tip is equidistant from sites I and II (the closest moiré sites to the tip) and so we model the moiré system as an N = 2 cluster as illustrated in Figure 3-8B. The on-site energy (Eq. (3.1)) for sites I and II can be written as ε and the electrostatic potential energy (Eq. (3.2)) for each site is $\nu = e\alpha(r^D)V_b - e\beta V_g$ where r^D = 3.9 nm is equidistant from sites I and II. Straightforward energetic considerations allow the N=2 ground state energy for different *n* to be written as $E(n = 2) = 2(\varepsilon + \nu) + U_{NN}$, $E(n = 1) = \varepsilon + \nu$, and $E(n = 0) = 0$. Figure 3-8C shows a plot of *E*(2), *E*(1), and *E*(0) as a function of applied electrostatic potential, ν. Three different regimes can be seen where the ground state energy transitions from an *n* = 2 charge state to an *n* = 1 charge state and then to an *n* = 0 charge state as ν is increased. The boundaries between these different charge states mark the locations of electron discharging events. The first discharging event happens when *E*(2) = *E*(1), which occurs at the potential $\nu^1 = -U_{NN} - \varepsilon$. The second discharging event happens when *E*(1) = *E*(0), which occurs at the potential $\nu^2 = -\varepsilon$. The difference in electrostatic potential energy between these two discharge events is then $\Delta\nu = \nu^2 - \nu^1 = U_{NN}$. Using Eq. (2) and assuming that the gate voltage remains unchanged while ramping the bias voltage (typical for our experiments) allows U_{NN} to be expressed in terms of the first and second discharge bias voltages: $U_{NN} = e\alpha(r^D)(V_2 - V_1) = e\alpha(r^D)\Delta V^D$.

The discharge cascade behavior when the tip is located at T can be analyzed using similar reasoning, except for an N=3 cluster instead of an N=2 cluster. In this case $v = e\alpha(r^T)V_b - e\beta V_g$, where $r^T = 4.7nm$ is the distance between T and the three neighboring $B^{Se/W}$ sites. The resulting energy levels for different *n* are found to be $E(3) = 3(\varepsilon + v) + 3U_{NN}$, $E(2) = 2(\varepsilon + v) + U_{NN}$, $E(1) = \varepsilon + v$, and $E(0) = 0$, which are plotted in Figure 3-8G. Discharging events in the 3-site moiré system thus occur at $v_1 = -\varepsilon - 2U_{NN}$, $v_2 = -\varepsilon - U_{NN}$, and $v_3 = -\varepsilon - U_{NN}$ (Figure 3-8H). This provides an additional means of finding the nearest-neighbor Coulomb interaction energy

$U_{NN} = v_3 - v_2 = v_2 - v_1 = \alpha(r^T)e\Delta V_b^T$ by utilizing the voltage difference, ΔV_b^T, between discharge events at T.

We note that the only unknown quantity here is the tip coupling constant $\alpha(r)$. It is, however, difficult to directly obtain its value experimentally. We can alternatively estimate its value through an electrostatic simulation, which will be discussed in Section 3.6.

3.5 Mapping Moiré Potential Fluctuation

A similar analysis can be used to determine variations in the Hubbard on-site energy, ε_i, for a moiré superlattice. This comes from the fact that for small V_b the STM tip can only discharge a single moiré site whose energy is described by $E(1) = \varepsilon + v$ and $E(0) = 0$ (i.e., the N=1 limit). In this case, discharge happens when $E(1) = E(0)$, which occurs when $v = -\varepsilon$. Fluctuations in ε are thus directly related to fluctuations in the discharge potential, $\delta\varepsilon = -\delta v$, which (using Eq. (2)) leads to $\delta\varepsilon = -e\alpha(r_t)\delta V_b$ where δV_b represents spatial fluctuations in the measured single-site discharge voltage.

This type of behavior can be seen experimentally as shown in Figure 3-9. Figure 3-9A shows a dI/dV map of a pristine region of the WSe_2/WS_2 moiré superlattice for V_g = 50 V and V_b = 0.465 V. The discharge rings around the $B^{Se/W}$ moiré sites are quite uniform in this defect-free region. This uniformity is also seen in a dI/dV spectra linecut (Figure 3-9B) that goes through five moiré sites along the red line in Figure 3-9A. Figure 3-9C, on the other hand, shows a dI/dV map obtained near a point defect (marked by a red dot) for a similar set of parameters (V_g = 53 V and V_b = 0.740 V). Here the discharge rings are highly non-uniform (the defect moiré site itself does not show a clear discharge ring for this set of parameters due to the large change in its onsite energy). The magnitude of the effect of the defect on neighboring moiré sites can be seen through dI/dV spectra (Figure 3-9D) obtained along the red linecut shown in Figure 3-9C. As seen in Figure 3-9D, the defect causes significant changes in the onsite energies of adjacent moiré sites. The discharge bias (measured at the discharge ring center, $r_t = 0$) of sites I and II, for example, is ~200 mV lower than those for sites III and IV (see blue dashed line in Figure 3-9D). This implies that the on-site energy shift on sites I and II is $\delta\varepsilon \approx \alpha(0)(200meV)$. Again, the quantity $\alpha(0)$ is unknown here and will be determined through electrostatic simulation in Section 3.6.

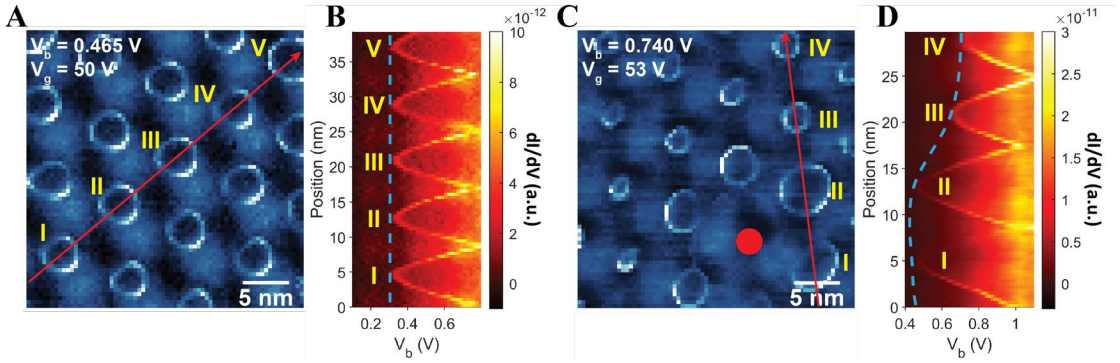

Figure 3-9 Inhomogeneity of moiré onsite energy. **A**. dI/dV map of a representative homogeneous region of the WS_2/WSe_2 moiré superlattice (V_b = 0.465 V, V_g = 50 V). **B**. dI/dV spectra measured along the red linecut shown in A. Discharge voltages at moiré sites I - V are seen to be nearly uniform. **C**. dI/dV map of discharge rings close to a point defect shows strongly non-uniform behavior. Solid red circle marks the position of the point defect (V_b = 0.740 V, V_g = 53 V). **D**. dI/dV spectra measured along the red linecut shown in (**C**). A significant reduction in discharge bias is observed for sites I and II near the defect. Tip-sample distance is determined by the setpoint: V_b = -3V, I = 100 pA.

3.6 Determination of the tip coupling coefficient α_i

As we have already mentioned above, a problem with our characterization of moiré Hubbard parameters up to now is that we cannot convert them to quantitative energies until we determine $\alpha(r_t)$, the geometric electrostatic conversion factor of Eq. (2). We require $\alpha(r^D)$, $\alpha(r^T)$, and $\alpha(0)$ to quantitatively determine U_{NN} and $\delta\varepsilon$. We can gain some experimental insight into the behavior of $\alpha(r_t)$ from the slopes of the lines representing discharge peaks in the dI/dV plots of Figs.1d Figure 3-1A andFigure 3-1B. The condition for discharge in these plots is $v = \alpha(r_t) \cdot eV_b - \beta \cdot eV_g = -C$, where C is a constant independent of V_b and V_g. This can be rewritten as $V_g = \frac{\alpha(r_t)}{\beta} V_b + \frac{C}{e\beta}$, which defines the linear discharge traces observed in Figs. 1d and 1e. The experimental slope of the discharge traces thus yields the ratio $\frac{\alpha(r_t)}{\beta}$. This does not provide the precise value of $\alpha(r_t)$ (since the back-gate factor β is still unknown), but by assuming that β is constant we can experimentally determine the proportionality of $\alpha(r_t)$ for different tip locations from the slopes of the discharge traces at those locations. We have done this for points D, T, and $B^{Se/W}$, thereby enabling us to determine the ratios $\alpha(r^D) : \alpha(r^T) : \alpha(0) = 0.53 : 0.39 : 1$.

Obtaining a quantitative value of $\alpha(r_t)$, however, remains difficult since the magnitudes of $\alpha(r_t)$ and β depend on non-universal details of the experimental setup. They involve, for example, capacitive coupling between the tip, back gate, and different layers of our device heterostructure. To overcome this problem, we utilized the COMSOL software package to numerically solve Poisson's equation for our specific device geometry.

Here we describe our determination of the values of α and β through the use of electrostatic simulations. The system geometry of our model is illustrated Figure 3-10A. The STM tip is approximated as a metallic cone with half angle θ.The apex-sample distance is H. The WS_2/WSe_2 heterostructure is approximated by two separate regions. The first region is a circular area with radius R_{hole} surrounding the moiré sites of interest (MSOI). The charge configuration in this region is set by the charging/discharging events described in the main text. The second region is the area outside the circle. The carrier doping in this region is relatively high and we can approximate it as a thin metal sheet. The Si back gate is regarded as an infinitely large metal plate and is separated from the TMD heterostructure plane by a distance d=320nm. The dielectric constants for the space above and below TMD heterostructure are assumed to be 1 (vacuum) and 4.2 (hBN and SiO_2).

As mentioned in the main text, the potential energy shift v induced by V_b and V_g has the form described by Eq. (3.2). We determine the values of α and β via the following method: first, to determine α we ground the tip and the metallic plane and apply a 1V potential to the Si back gate. The value of the induced electric potential at the position of the moiré electron (dot at the hole center) then equals α. To determine β, we ground the Si back gate and the metallic plane and apply a 1V potential to the tip. The resulting value of the electric potential at the hole center then equals β.

Here we describe how to interpret the simulation results and compare them to the experimental data. Our simulation results should be fitted to the variation of the slopes of the dispersive discharging peak (for example Figure 3-1) that equals to $\alpha(r_t)/\beta$. When the tip is close to the MSOI (for example at r_t=0) both H and θ significantly impact α. However, when r_t is large, the impact of the tip height, H, on α is negligible since H plays a negligible role in determining the distance between MSOI and the tip apex. Therefore, the shape of the curve $\alpha(r_t)/\beta$ vs r_t can help us to choose the correct H and θ to match our experimental results. Finally, the radius of the hole R_{hole} determines the screening strength of the surrounding TMD heterostructure on the external potential applied by the tip and the back gate. The value of R_{hole} therefore does not significantly affect the shape of the curve $\alpha(r_t)/\beta$ vs r_t (as long as r_t is smaller than R_{hole} (in order of magnitude as the moiré period), a condition that is satisfied here).

Our electrostatic simulations were performed using COMSOL. The distribution of $\alpha(r_t)/\beta$ as the function of r_t is well reproduced by using the following parameters: $\theta = 30°$, H=0.8 nm, and R_{hole}=8nm. Figure 3-10B shows the simulated α (blue) and β (orange) as functions of r_t. As expected, β has a negligible change with the increase of r_t. The simulated ratio $\alpha(r_t)/\beta$ is plotted in Figure 3-10C (orange curve) and is seen to compare well to the experimental data for $\alpha(r_t)/\beta$ (blue dots). The simulation yields $\alpha(r^T) \approx 0.18$, $\alpha(r^D) \approx 0.16$, and $\alpha(0) \approx 0.33$, with their ratio $\alpha(r^D) : \alpha(r^T) : \alpha(0) = 0.55 : 0.49 : 1$ in reasonable agreement with the experimental ratios above.

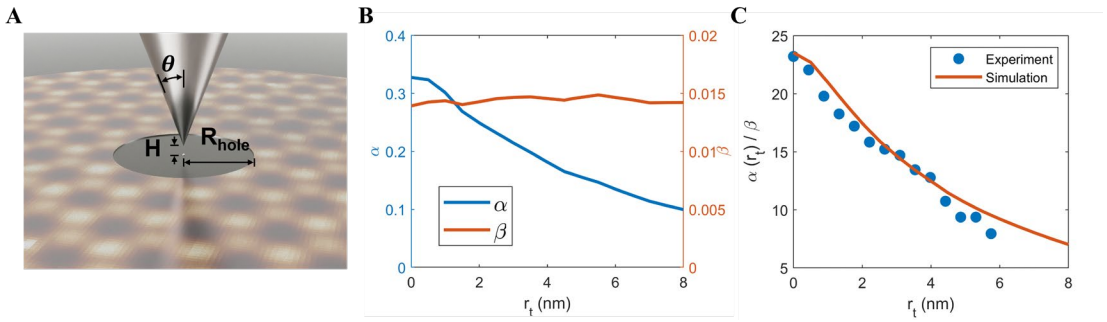

Figure 3-10 Electrostatic simulation of α and β. **A**. Electrostatic model of the tip-moiré system. The tip apex is taken as a metallic cone with half angle θ and height H above the moiré site of interest (MSOI). The surrounding TMD heterostructure is assumed to be an infinitely large metallic plane with a hole of radius R_{hole} around the MSOI (the dot located at the hole center). The Si back gate is regarded as an infinitely large metal plate and is separated from the TMD heterostructure plane by a distance d=320nm (not shown in A). **B**. Simulated α (blue) and β (orange) as functions of r_t. As expected, β is seen to be nearly independent of r_t in our simulation range. **C**. Experimentally measured (blue points) and simulated (orange curve) values of $\alpha(r_t)/\beta$ as a function of r_t. The experiment and simulation show good agreement for the values H = 0.8 nm, $\theta = 30°$, and R_{hole} = 8 nm.

3.7 Results and Discussion

After obtaining the value of $\alpha(r)$, we can extract a quantitative value of U_{NN} = 22 ± 2 meV from our measurements at D and U_{NN} = 27 ± 2 meV from our measurements at T. These two values of U_{NN} are in reasonable agreement with each other, a self-consistency check that helps to validate our overall approach. We are also able to determine the fluctuation in onsite energy of sites I and II around the point defect in Fig. 4c to be $\delta\varepsilon \sim 65\, meV$.

The expected value of U_{NN} can be roughly estimated by considering the energy difference associated with the initial position ($\vec{r}_i$) of the discharging electron and its final position ($\vec{r}_f$) after discharge. For an electron being discharged from the N=2 cluster discussed above for point D, the initial electrostatic energy is $E(\vec{r}_i) \approx \frac{1}{4\pi\epsilon_{eff}\epsilon_0} \cdot \frac{e^2}{l_m}$ (assuming each moiré site contains one electron). In order to discharge, an electron need only escape a screening distance away from the STM tip. Although the screening distance is difficult to determine accurately, since only two lattice sites participate in discharge events at D (Fig. 3a) we can estimate it to be on the order of l_m. An electron thus needs only to hop a distance ~l_m to escape, thus placing the electron in some final configuration with a residual Coulomb energy of the order of $\frac{e^2}{\eta \cdot l_m}$, where $\eta \cdot l_m$ is the distance of the escaped electron from the remaining electron. Taking η to be approximately 2, the electron's energy difference is then $U_{NN} = E(\vec{r}_i) - E(\vec{r}_f) \approx \frac{1}{4\pi\epsilon_{eff}\epsilon_0} \cdot \left(\frac{e^2}{l_m} - \frac{e^2}{2l_m}\right) = \frac{1}{4\pi\epsilon_{eff}\epsilon_0} \cdot \frac{e^2}{2l_m}$. Here the effective dielectric constant is $\epsilon_{eff} =$

$\frac{1}{2}(\epsilon_{vac} + \epsilon_{hBN})$ where $\epsilon_{vac} = 1$ and ϵ_{hBN} is the dielectric constant of hBN. Since the dielectric constant of hBN is anisotropic, we approximate it as $\epsilon_{hBN} = \frac{1}{2}(\epsilon_{\perp} + \epsilon_{\parallel})$ where $\epsilon_{\perp} = 4$ and $\epsilon_{\parallel} = 7$ are the out-of-plane and in-plane hBN dielectric constants, respectively(*82*).

Taken together, these parameters yield an expected value of $U_{NN} \approx 30$meV, reasonably consistent with our experimental value of $U_{NN} \approx 25$meV obtained by averaging the U_{NN} values measured at D and T. We note that this value of U_{NN} is significantly larger than the bandwidth $W \approx 5$meV obtained from *ab initio* calculations of the conduction miniband for WSe_2/WS_2 moiré heterostructures (Figure 3-4A). This confirms that WSe_2/WS_2 heterostructures lie in the strongly correlated limit, consistent with previous observations of the extended Wigner crystal states in TMD moiré superlattices(*48, 83-85*).

3.8 Summary and Outlook

In this chapter, we have demonstrated a new technique for imaging and manipulating the local charge state of correlated electrons in gated WS_2/WSe_2 moiré superlattices using the tip of an STM. Observation of a cascade of local electron discharging events enables us to obtain key microscopic parameters of the extended Hubbard model that describes this moiré system. This technique should be broadly applicable to other types of moiré systems, offering a powerful new tool for microscopic characterization and control of correlated electrons in moiré superlattices.

4 Imaging Two-dimensional Generalized Wigner Crystals

4.1 Introduction and Background

In Chapter 2 and 3 we have studied the orbitals and interactions of electrons in the TMD moiré superlattice. However, the resulting emergent quantum phases of multiple corelated moiré electrons such as correlated insulators or even electron crystals have not been explored microscopically yet. In this chapter, we will try to explore how the electron Coulomb interactions can greatly modify their collective behavior and induce new exotic quantum phases of matter such as the Wigner crystal.

A Wigner crystal is the crystalline phase of electrons stabilized at low electron density where long-range Coulomb interactions dominate over quantum fluctuations in electron motion. The long pursuit of Wigner crystals(*48, 74, 83, 86-91*) has motivated the study of 2D electron gases at high magnetic field where electron kinetic energy is quenched by degenerate Landau levels(*92, 93*) and has led to the discovery of new quantum hall states(*94, 95*). Electrical transport signatures of Wigner crystal states have been reported in extremely clean GaAs/AlGaAs quantum wells(*86, 87*) as well as graphene(*88*) at sufficiently low doping and high magnetic field. Signs of Wigner crystallization have also been detected for electrons trapped at the surface of liquid helium(*96-99*). Recently, the discovery of moiré flat minibands in van der Waals heterostructures has opened a new route to realize Wigner crystal states at zero magnetic field(*100*). Several optical and conductance measurements have provided evidence of rich generalized Wigner crystal states (generalized on a lattice background(*33*)) in different TMD moiré superlattices(*48, 74, 83, 90*). This evidence for 2D Wigner crystals, in the form of new transport and optical responses at fractional charge filling factors, is indirect and could potentially be explained by other quantum phases such as fractional quantum Hall states(*94*). The most direct evidence of 2D Wigner crystals would be real-space imaging of the 2D electron lattice, which has remained an outstanding experimental challenge.

Real-space imaging of 2D Wigner crystals places stringent requirements on the measurement technique. It must simultaneously have high spatial resolution, high single-electron sensitivity, and low perturbation to the electron lattice. The last two requirements conflict with each other since high sensitivity requires strong coupling to the Wigner crystal whereas a low perturbation requires weak coupling. For example, conventional STM measurements have excellent spatial resolution and charge sensitivity but can be highly invasive since inevitable tip-gating effects can destroy the delicate Wigner crystal lattice. Here we utilize a novel STM measurement scheme that strikes a balance between these two competing requirements, thus enabling real-space imaging of the n=2/3, n=1/2, and n=1/3 2D Wigner crystal states in WSe_2/WS_2 moiré heterostructures.

The work described in this chapter is mainly finished by Shaowei and me with supports from the Wang, Crommie group. Part of the discussion is also presented in a published paper(*101*).

4.2 STM Imaging Through a Sensing Layer

As mentioned above, imaging the fragile electron crystalline phases requires a technique that is sufficiently non-invasive, while conventional STM measurement may not satisfy this stringent requirement. To overcome this issue, we developed a new sensing-layer-assisted STM imaging method. Our new STM scheme employs a specially designed van der Waals heterostructure as illustrated in Figure 4-1A (the sample fabrication method is similar to the one described in Chapter 2). It integrates a gated WSe_2/WS_2 moiré heterostructure and a top graphene monolayer sensing layer that are separated by a hexagonal boron nitride (hBN) layer with a thickness d_t = 5nm. This separation is small enough that the STM tip and graphene layer can efficiently couple to individual moiré electrons in the WSe_2/WS_2 superlattice (moiré lattice constant ~8nm), but still large enough that the tip and graphene layer remain non-invasive with respect to the delicate Wigner crystal states. STM tunneling current into the graphene sensing layer can be modulated by the charge states of different moiré sites in the WSe_2/WS_2 superlattice through local Coulomb blockade effects(*102*). This technique allows us to detect the local charge distribution in the WSe_2/WS_2 heterostructure and to image the embedded Wigner crystal lattice.

Figure 4-1B shows a typical large-scale topography image measured on the top graphene surface. The top graphene and hBN layers cover the WSe2/WS2 heterostructure conformally and inherit the topography of the 3D reconstructed moiré superlattice(*64*) below. Figure 4-1C shows a zoom-in topographic image corresponding to the red dashed box area in Figure 4-1B. A red rhombus labels the primitive cell of the moiré superlattice with the four high points corresponding to AA stacking regions and the two inequivalent low points corresponding to distinct AB stacking regions (denoted AB_1 and AB_2)(*64*). However, we are not able to distinguish which AB stacking region corresponds to the $B^{Se/W}$ or $B^{W/S}$ site at this stage due to their similar topographic features and the hBN covered on it forbidding the direct STS measurement of the underlying TMD layer. The measured moiré lattice constant is LM = 8nm, yielding a near 0° twist angle through the formula $L_M = \frac{a}{\sqrt{\delta^2+\theta^2}}$, where $\delta = (a - a')/a$ is the lattice mismatch, a = 3.153 Å and a' = 3.28 Å are the atomic lattice constants of the WS2 and WSe2, respectively(*103*).

The WSe_2/WS_2 heterostructure is dual-gated by the top graphene sensing layer (top gate) and the silicon substrate (back gate) (Figure 4-1A). The top gate dielectric is defined by the top hBN flake (d_t = 5nm) while the bottom gate dielectric is defined by a combination of SiO_2 (d_{SiO2} = 285nm) and hBN (d_b = 70nm). The carrier densities in the WSe_2/WS_2 heterostructure and the top graphene can be controlled independently via the top gate voltage, V_{TG}, and bottom gate voltage, V_{BG} (due to the presence of two different gate voltages in this work we denote them in a way that is different from the previous

chapters). In this study we mainly focus on the electron-doped regime of the WSe_2/WS_2 heterostructure.

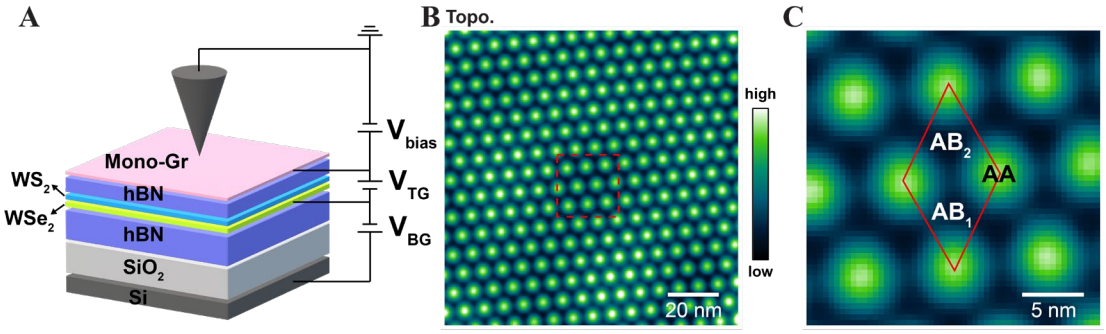

Figure 4-1 STM measurement of a dual-gated WSe_2/WS_2 moiré superlattice through sensing layer. **A**. Schematic of the dual-gated WSe_2/WS_2 moiré heterostructure device. The top hBN thickness (5nm) is slightly smaller than the moiré lattice constant (8nm). Top gate (V_{TG}) and bottom gate (V_{BG}) voltages are applied to separately control the carrier density in the WSe_2/WS_2 heterostructure as well as the top graphene sensing layer. **B**. A typical large-scale topography image measured on the top graphene surface. V_{bias} = 180mV and I = 300 pA. **C**. Zoom-in image of the red dashed box in (**B**). The red rhombus labels a primitive cell. Peaks correspond to AA stacking regions and the two inequivalent low points correspond to distinct AB stacking regions (denoted AB_1 and AB_2).

4.3 Spectroscopic Signatures of Generalized Wigner Crystals

We first try to probe the signatures of strongly correlated states in the WSe_2/WS_2 through scanning tunneling spectroscopy. For $V_{TG} = 0$, the Fermi level is within the band gap for the WSe_2/WS_2 heterostructure (see illustration in Figure 4-2A). In this case, tuning V_{BG} dopes charge carriers exclusively into the graphene layer. Figure 4-2B shows a 2D plot of the STM differential conductivity (dI/dV) spectra of graphene at $V_{TG} = 0$ for different values of V_{BG}. The dispersive feature labeled by the white dashed line shows the evolution of the graphene charge neutral point (CNP) in response to the electrostatic doping from V_{BG}(*40, 78, 104*). The persistent gap near $V_{bias} = 0$ arises from an inelastic tunneling gap that occurs at all gate voltages and causes the graphene CNP curve to abruptly shift as it ramps through the zero-bias region(*40, 104*).

We can dope electrons into the WSe_2/WS_2 heterostructure by applying a positive V_{TG} such that the WSe_2/WS_2 heterostructure Fermi level lies near the conduction band edge (see illustration in Figure 4-2C). Here we choose $V_{TG} \sim 0.5V$ so that the WSe_2/WS_2 heterostructure can be electron doped while the graphene sensing layer remains close to charge neutral. The reason for doing this is that the resulting small density of states for graphene provides the highest sensitivity for imaging Wigner crystal states in the moiré superlattice. Charge neutral graphene also has less of a screening effect on the moiré electron-electron interactions due to the long screening length of Dirac electrons at the CNP(*105*). Fig. 1g shows the resulting dI/dV spectra as a function of V_{BG} at a fixed V_{TG}

= 0.53V. This panel corresponds to the same (V_{BG}, V_{bias}) phase space outlined by the dashed white box in Fig.1e, but for nonzero V_{TG}.

Figure 4-2D shows that the graphene is hole-doped at $V_{BG} < 7V$, while the WSe_2/WS_2 heterostructure cannot be hole-doped under these conditions given the band alignment shown in Figure 4-2C. The graphene hole doping leads to dispersive movement of the graphene CNP at $V_{BG} < 7V$ (denoted by the white dashed line in Figure 4-2D). Electron doping for $V_{BG} > 7V$, however, leads to very different behavior. In a non-interacting single-particle picture, the electron doping would occur predominantly in the WSe_2/WS_2 heterostructure because its density of states (DOS) is orders of magnitude larger than the graphene DOS at the Dirac point. Therefore, one would expect the graphene Fermi energy to stay fixed near the Dirac point, as illustrated by the vertical dashed line at $V_{BG} > 7V$. Experimentally, however, we observe a non-trivial shift of the graphene CNP with respect to the Fermi energy at different V_{BG} values. The graphene layer undergoes electron doping when the WSe_2/WS_2 heterostructure experiences fractional filling of the moiré superlattice with n=1/3, 1/2, 2/3, and 1 (black dashed lines in Figure 4-2D). Figure 4-2E displays a vertical line-cut of the gate-dependent dI/dV spectra at $V_{bias} = 0.1V$, showing clear peaks at these fractional fillings. These features signify the correlated gaps in the WSe_2/WS_2 Mott insulator state at n=1 as well as the generalized Wigner crystal insulator states at n=1/3, 1/2, 2/3. This is because the correlated gaps make the WSe_2/WS_2 heterostructure electronically incompressible and so electrons are electrostatically forced into the graphene sensing layer. Similar effects have been observed for capacitance and single-electron-transistor measurements of electronic compressibility in different van der Waals heterostructure systems(*25, 42, 106-108*). Our STM configuration thus provides a new technique for mapping the local electronic compressibility of correlated insulating states in moiré superlattices. After observing the spectroscopic signatures of these generalized Wigner crystal states, then an natural following idea is to directly map them spatially, as discussed in the next section.

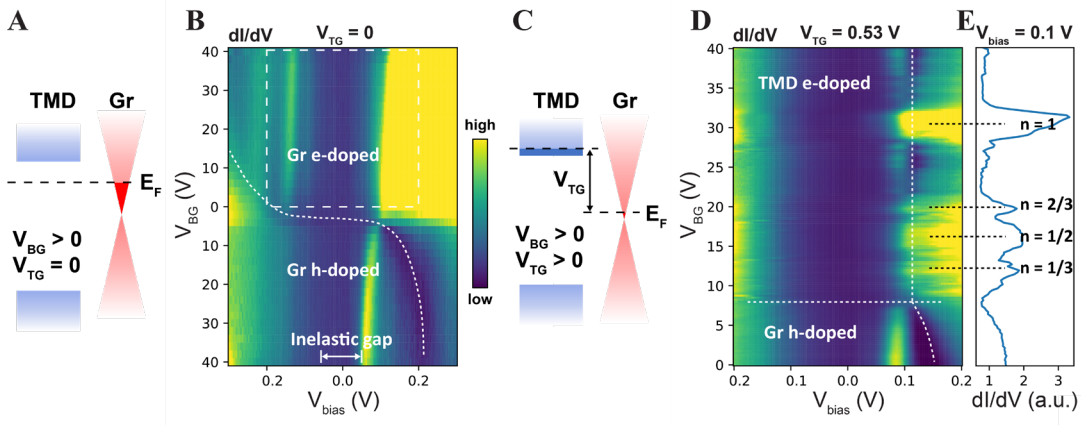

Figure 4-2 STS signatures of correlated states in the WSe_2/WS_2 moiré heterostructure. **A**. Schematic of the heterostructure band alignment and Fermi levels for $V_{TG} = 0$ and $V_{BG} > 0$. At zero V_{TG}, the Fermi level of the WSe_2/WS_2 heterostructure is located in the band gap. **B**. V_{BG}-dependent dI/dV spectra measured on the graphene sensing layer over an AA stacking site for $V_{TG} = 0$. The dispersive feature marked by the white dotted curve shows the evolution of the graphene charge neutral point (CNP) induced by electrostatic doping

from V_{BG}. The persistent gap near $V_{bias} = 0$ arises from an inelastic tunneling gap that exists at all gate voltages. Due to this inelastic tunneling gap, the graphene CNP curve shows an abrupt shift as it shifts over the zero-bias region. The tip height was set by the following parameters: V_{bias} = -300mV and I = 100 pA. **C**. Schematic of the heterostructure band alignment and Fermi levels for $V_{TG} > 0$ and $V_{BG} > 0$. Application of an appropriate positive V_{TG} allows the Fermi level of the WSe_2/WS_2 heterostructure to be lifted into the conduction band. **D**. V_{BG}-dependent dI/dV spectra measured on the graphene sensing layer over an AA stacking site for V_{TG} = 0.53V. This is a zoom-in of the electron doped regime corresponding to the phase space denoted by the white dashed box in e. The graphene is hole-doped in the region below the horizontal dashed line (V_{BG} < 7V), and the WSe_2/WS_2 is electron-doped in the region above it (V_{BG} > 7V). The vertical white dash curve indicates the expected movement of the graphene CNP for a non-interacting picture. Significant electron doping of the graphene layer takes place at n = 1/3, 1/2, 2/3, and 1 (denoted by horizontal black dashed lines in (**D**)). The tip height was set by the following parameters: V_{bias} = -200mV and I = 100 pA. E. Vertical line-cut through the V_{BG}-dependent dI/dV spectra in (**D**) at V_{bias} = 0.1V shows peaks at n=1, 2/3, 1/2, and 1/3.

4.4 Real-space Imaging of Generalized Wigner Crystals

To be able to directly image the 2D electron crystal for the first time would be one of the most exciting parts of this work. Real-space imaging of the 2D electron lattice of the Mott insulator and Wigner crystal states was performed through 2D dI/dV mapping of the graphene sensing layer, as illustrated in Figure 4-3A. The Mott and Wigner crystal states form periodic electron lattices in the WSe_2/WS_2 moiré heterostructure that couple to the graphene sensing layer and STM tip through long-range Coulomb interactions. The tunnel current between the STM tip and the graphene layer will vary spatially depending on the charge state of the WSe_2/WS_2 moiré site below the STM tip. As a result, the electron lattices of the Mott and Wigner crystal states can be imaged as periodic lattice structures in 2D dI/dV mappings of the graphene sensing layer.

Figure 4-3B displays the topographic image of a typical region of the WSe_2/WS_2 moiré superlattice. The triangular lattice formed by the AB_1 stacking sites have been marked with solid red dots. This region exhibits a lattice that is free of distortion or atomic defects, an essential condition for observing Mott and Wigner crystal states with long-range order.

Figure 4-3C shows a dI/dV mapping of the graphene layer when the WSe_2/WS_2 moiré heterostructure is in the n = 1 Mott insulator state (V_{bias} = 160mV, V_{BG} = 30V, and V_{TG} = 0.53 V; see Methods for more measurement details). A highly ordered triangular lattice of bright features can be clearly observed that corresponds to the AB_1 stacking sites of the moiré superlattice. Such AB_1 stacking sites are illustrated as red dots in Figure 4-3B. Since the AB_1 and AB_2 stackings sites are similar in topography, the centering of the bright features in Fig. 1c on the AB_1 stacking sites implies that these features do not originate from topography, but rather from the underlying electron lattice of the Mott insulator state. This is consistent with previous work showing that conduction flat band electrons in the WSe_2/WS_2 moiré heterostructure are localized at one of the AB stacking

sites(*102*). Figure 4-3D displays the fast Fourier transform (FFT) image of the dI/dV map in Figure 4-3C, showing sharp diffraction points associated with the electron lattice of the Mott insulator state. The reciprocal unit vectors of the moiré superlattice are marked by green dots in the FFT image and are seen to overlap perfectly with the lowest order diffraction points of the Mott insulator electron lattice.

We next imaged the generalized Wigner crystal states at fractional fillings. Figure 4-3E shows the dI/dV mapping of the n = 2/3 generalized Wigner crystal state (V_{bias} = 160mV, V_{BG} = 21.8V, V_{TG} = 0.458 V). FFT filtering has been performed on this and subsequent Wigner crystal images in Figure 4-3 to suppress periodic features associated with the moiré superlattice (i.e., the green dots in Figure 4-3F). The n = 2/3 dI/dV map exhibits a honeycomb lattice with lattice constant $\sqrt{3}L_M$. This is consistent with 2/3 of the available AB_1 sites being filled with electrons (i.e., the solid red dots located in bright regions of the image) and the other 1/3 AB_1 sites being empty (i.e., the open red circles located in dark regions of the image) so as to minimize total nearest-neighbor interactions. Such a honeycomb lattice matches previous predictions(*48, 74, 83, 90*) and confirms the existence of generalized Wigner crystal states where moiré electrons are stabilized by long-range Coulomb interactions and exhibit well-defined 2D crystalline order. The corresponding FFT image (Figure 4-3F) demonstrates the emergence of a new lattice: six sharp diffraction points associated with the generalized Wigner crystal lattice appear *inside* the reciprocal unit vectors (green dots) of the moiré superlattice.

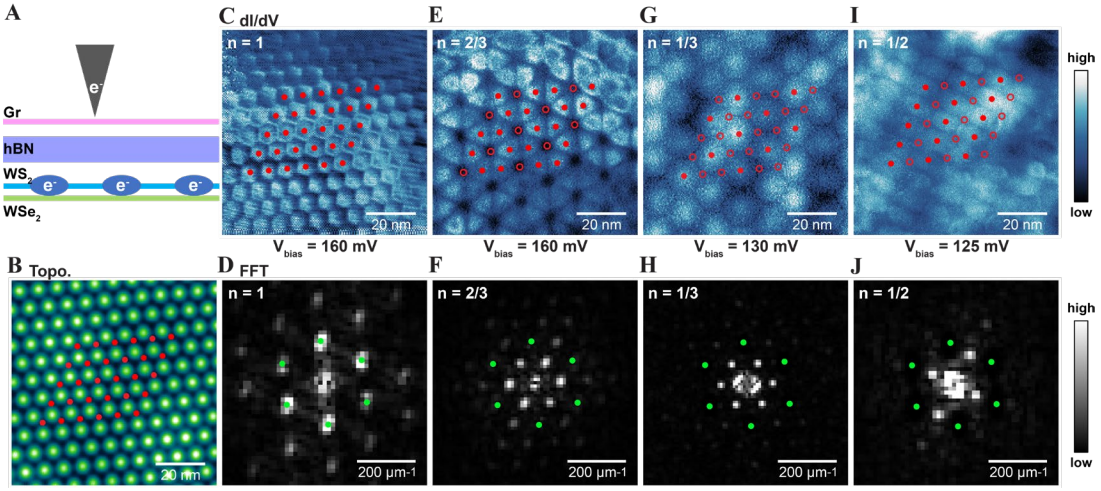

Figure 4-3 Imaging Mott and generalized Wigner crystal states. **A**. Schematic shows imaging of correlated states in a WSe_2/WS_2 moiré superlattice beneath a graphene sensing layer. dI/dV maps are acquired at the top graphene surface. **B**. A typical STM topographic image of the moiré superlattice shows a perfect lattice without distortion or defects. The triangular lattice formed by the AB_1 stacking sites is marked by solid red dots. **C**. dI/dV map of the n = 1 Mott insulator (V_{bias} = 160mV, V_{BG} = 30V, V_{TG} = 0.53 V). The triangular lattice formed by the AB_1 stacking sites is labeled with red dots. **D**. Fast Fourier transform (FFT) of the image shown in (**C**). The reciprocal unit vectors of the moiré superlattice are labeled by green dots. E-J. dI/dV maps of the generalized Wigner crystal states for different electron fillings and their corresponding FFT images: **E**. dI/dV map of n = 2/3 state (V_{bias} = 160mV, V_{BG} = 21.8V, V_{TG} = 0.458 V). F. FFT of n

= 2/3 state shown in (**E**). **G**. dI/dV map of n = 1/3 state (V_{bias} = 130mV, V_{BG} = 14.9V, V_{TG} = 0.458 V). **H**. FFT of n = 1/3 state shown in (**G**). **I**. dI/dV map of n = 1/2 state (V_{bias} = 125mV, V_{BG} = 18.7V, V_{TG} = 0.458 V). **J**. FFT of n = 1/2 state shown in (**I**). FFT filtering was performed in the Wigner crystal images (**E-J**) to suppress the periodic features associated with the moiré superlattice (i.e., green dots in (**F,H,J**); see Methods for unfiltered images). Electron-filled AB_1 sites are labeled with solid red dots and the empty AB_1 sites are labeled with open red circles in the real-space images (**E,G,I**). The locations of the reciprocal unit vectors of the moiré superlattice are marked by green dots in (**F,H,J**).

Figure 4-3G and Figure 4-3H show the dI/dV map and corresponding FFT image, respectively, of the n=1/3 generalized Wigner crystal state (V_{bias} = 130mV, V_{BG} = 14.9V, V_{TG} = 0.458 V). The real-space image demonstrates a new triangular electron lattice associated with a Wigner crystal state where 1/3 of the available AB_1 sites are filled with electrons (solid red dots) and the other 2/3 AB_1 sites are empty (open red circles). The FFT image shows a clear diffraction pattern of the generalized Wigner crystal state with a lattice constant of $\sqrt{3}L_M$. The n = 2/3 and n = 1/3 states have similar diffraction patterns since they share the same primitive cell and are linked by a particle-hole transformation.

Figure 4-3I shows a dI/dV map of the n = 1/2 generalized Wigner crystal state (V_{bias} = 125mV, V_{BG} = 18.7V, and V_{TG} = 0.458 V). The image reveals unambiguously that the C3 symmetry of the host moiré superlattice is spontaneously broken for this generalized Wigner crystal state. The n = 1/2 state features a stripe symmetry with electrons (solid red dots) filling the AB_1 sites in alternating lines (empty sites are marked by open red circles). The lattice constants of this stripe phase are L_M and $\sqrt{3}L_M$ along the parallel and perpendicular directions, respectively. The corresponding FFT image in Figure 4-3J shows a rhombus-like reciprocal unit vectors, further confirming the broken symmetry of this stripe phase for the n = 1/2 generalized Wigner crystal state.

The n=1/2 generalized Wigner crystal state is predicted to be highly degenerate, with multiple electron lattice configurations having the same energy in the case of only nearest-neighbor interactions(*83*). The spontaneous broken symmetry of the n = 1/2 state might therefore be governed by higher-order effects, such as next-nearest-neighbor interactions and/or accidental strain in the lattice (uniaxial strain ~ 0.39%, as shown in Figure 4-4). We have also noticed that the n = 1/2 electron lattice is more fragile than the n = 1/3 and 2/3 states.

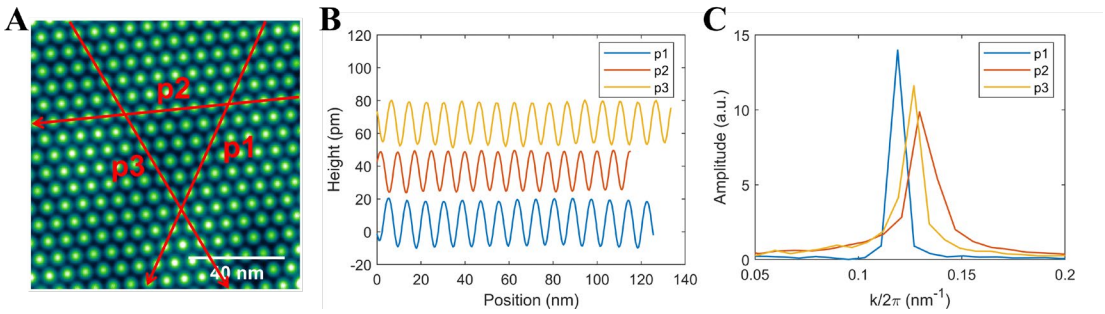

Figure 4-4 Uniaxial strain of the moiré superlattice. **A**. Topography image shown in Figure 4-1B. Three height line profiles (p1-3) labeled with red arrows in (**A**) are plotted in (**B**), and the corresponding fast Fourier transform results are shown in (**D**). The different wavevector amplitudes along the three different directions reflect the moiré superlattice uniaxial strain. A 3.9% uniaxial strain is present within the moiré heterostructure.

4.5 First Trial on Exploring the Imaging Mechanism

We last present a short discussion about the imaging mechanism underlying the dI/dV mapping of generalized Wigner crystal lattices assisted by a graphene sensing layer. As illustrated in Figure 4-3A, the STM tunneling current into the graphene layer can be coupled to moiré electrons below the tip through long-range Coulomb interactions. This coupling can affect the tunnel current in two different ways: (1) the localized moiré electrons can induce local band bending in the graphene sensing layer, thus changing the graphene local density of states and hence the dI/dV signal. (2) application of V_{bias} can discharge the moiré electron right below the tip once V_{bias} exceeds a threshold value. This mechanism is helped by the fact that electrical screening by the top monolayer graphene is weak when its Fermi level is close to the Dirac point. A resulting moiré electron discharging event could then lead to a sudden increase in the STM tunneling current due to the elimination of the Coulomb blockade effect, hence contributing to a stronger dI/dV signal(*102*).

To distinguish between these two mechanisms, we systematically examined the dI/dV map evolution with changing V_{bias}. Figure 4-5 show dI/dV maps of the n = 2/3 Wigner crystal state as V_{bias} is increased from 130mV to 190mV. No FFT filtering was performed on these images. The honeycomb lattice associated with the n = 2/3 state is not so clearly seen at V_{bias} = 130 mV (Figure 4-5A) but emerges when V_{bias} is increased to 145 mV (Figure 4-5B). The dominant features are the bright dots centered on the AB_1 stacking sites. These features expand with increased V_{bias} (Figure 4-5C) and ultimately form ring-like features (Figure 4-5D and Figure 4-5E). Such behavior (i.e. expanding rings with increased tip bias) is characteristic of tip-induced electrical discharging rings(*39, 79-81, 102*) and occurs because electrical discharging for larger tip-electron distances requires larger tip biases. This indicates that mechanism (2) discussed above is the dominant contrast mechanism for imaging Wigner crystal lattices in our dI/dV maps.

The STM tip locally discharges the moiré electron localized at the AB_1 site closest to the tip apex once V_{bias} is large enough and the tip-electron distance is short enough. This enables discharge features centered around *filled* AB_1 sites to be observed in dI/dV maps of the graphene sensing layer. A more detailed exploration on the imaging mechanism and its application in probing more physical properties of the generalized Wigner crystal states will be discussed in the next chapter.

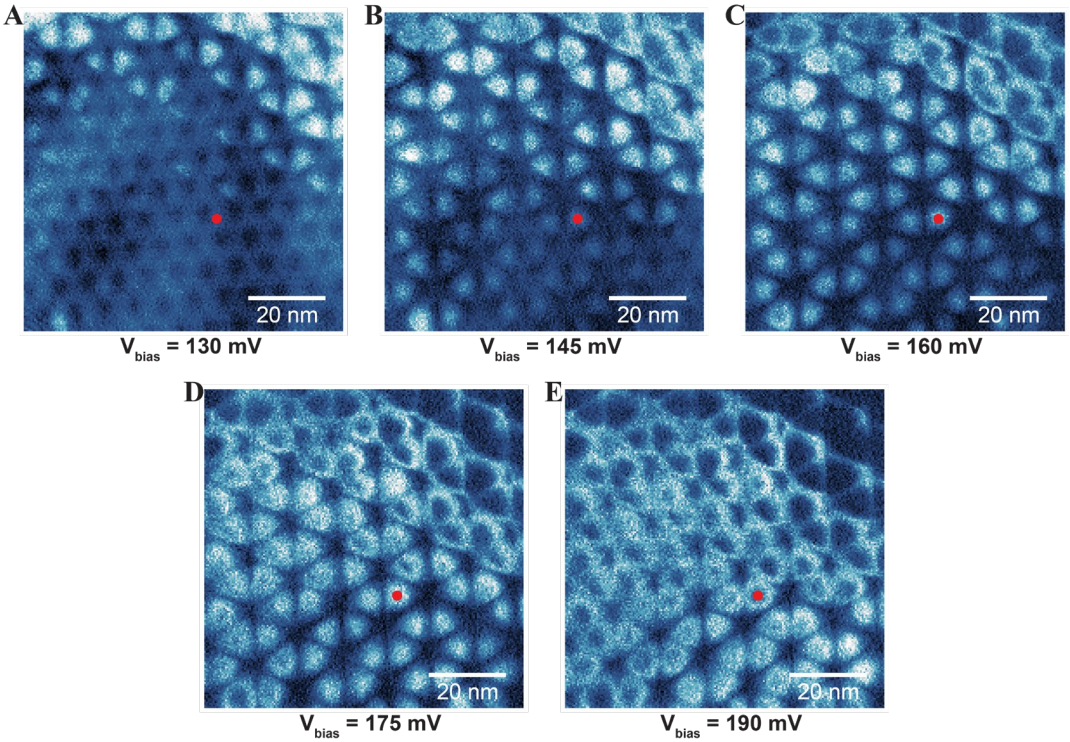

Figure 4-5 Evolution of dI/dV maps for the n = 2/3 state with increased V_{bias}. dI/dV maps of the n = 2/3 generalized Wigner crystal state measured for (**A**) V_{bias} = 130mV, (**B**) V_{bias} = 145mV, (**C**) V_{bias} = 160mV, (**D**) V_{bias} = 175mV, and (**E**) V_{bias} = 190mV. Gate voltage parameters: V_{BG} = 21.8V, V_{TG} = 0.458 V. All five maps are measured in the same region and no filtering has been performed. The map in (**C**) (V_{bias} = 160mV) shows the same data as Figure 4-3E, but with no filtering. The red dot labels one typical electron-filled AB_1 site where a discharging ring can be observed that gets larger with increased V_{bias} (a common characteristic of discharging phenomena).

4.6 Summary and Outlook

In conclusion, our new STM imaging technique combines high spatial resolution and sensitivity with minimal perturbation and allows direct imaging of 2D generalized Wigner crystals in real space. This technique should be generally applicable to a wide variety of van der Waals moiré heterostructures and provides a powerful tool for imaging real-space electron configurations of novel correlated quantum phases in 2D systems.

5 Mapping Charge Excitations in Generalized Wigner Crystals

5.1 Introduction and Background

In Chapter 4 we discussed imaging generalized Wigner crystals with a new sensing-layer assisted STM technique. However, at that stage we only know that the probe relies on a long-range Coulomb interaction between the electrons in the underlying TMD layer the tip-graphene tunneling junction. However, a full understanding of the imaging mechanism is still lacking which hence hinders its further application in measuring more quantitative properties of the generalized Wigner crystals as well other fragile correlated states. Therefore, in this chapter we will uncover the imaging mechanism and show that it is essentially a local thermodynamic measurement of the correlated states. Particularly, it could be one of the thermodynamic probe methods with the highest spatial resolution.

As mentioned previously, a variety of generalized Wigner crystal states have been reported in transition metal dichalcogenide (TMDC) moiré superlattices(*48, 73-75, 101*), and real-space imaging of the electron lattice of generalized Wigner crystals has been performed using a new form of non-invasive STM imaging(*101*). A microscopic understanding of elementary excitations in generalized Wigner crystal, however, is still lacking. Theoretical studies predict that unusual quasiparticle excitations across the correlated gap between upper and lower Hubbard bands can arise due to long-range Coulomb interactions in generalized Wigner crystal states(*68, 100, 109*). However, because of the fragile electron lattice and small energy scale, it is challenging to image quasiparticle (e.g., electron/hole) wavefunctions and to spectroscopically determine the correlated gaps of generalized Wigner crystals.

Several scanning probe microscopy techniques have previously been developed to probe fragile correlated states, such as scanning charge accumulation microscopy(*110-112*) and scanning single-electron transistor microscopy(*25, 26, 42*). The spatial resolution of these microscopy tools, however, is typically limited to ~100nm, and so is not sufficient to image generalized Wigner crystal quasiparticle states at the single unit cell level. Here we describe a new scanning single-electron charging (SSEC) spectroscopy that has ~1 nm spatial resolution as well as single electron sensitivity. SSEC spectroscopy technique combines STM with a monolayer graphene sensing layer and enables local manipulation of individual electron- and hole-quasiparticles in generalized Wigner crystals via STM tip-based local gating. It enables direct visualization of quasiparticle excitations and spectroscopic determination of the thermodynamic gap of generalized Wigner crystals. Using this technique, we observe that electron and hole quasiparticles excitations exhibit complementary wavefunction distributions and that thermodynamic gaps of order 50meV exist for the 1/3 and 2/3 generalized Wigner crystal states.

The work described in this chapter is mainly finished by Ziyu and me with supports from the Wang, Crommie group.

5.2 Principle of Scanning Single-electron Charge Spectroscopy

To demonstrate the new SSEC spectroscopy, here we investigate a device with similar configuration to the one studied in Chapter 4. Figure 5-1A shows the sample design and the measurement scheme. We note that here the sample is a near-60° twisted WS_2 (t-WS_2) moiré heterostructure encapsulated in hBN layers which is different from the 0°-degree-aligned WSe_2/WS_2 moiré heterostructure used in Chapter 3 and 4. The near-60° twisted WS_2 exhibits stronger moiré potential and flatter moiré minibands(*71*), making its correlated physics easier to observe. Similarly, it is dual gated by a monolayer of graphene on top (the top gate) and graphite on the bottom (the bottom gate). The hBN dielectric layer thicknesses for the top and bottom gates are 5.8nm and 37nm, respectively. The sample fabrication shares the same method as the one used in Chapter 4. Similarly, the charge carrier densities of the t-WS_2 and the top graphene sensing layer are tuned independently by applying a bottom gate voltage V_{BG} and a top gate voltage V_{TG}. A bias voltage (V_{bias}) is applied between the graphene top gate (otherwise known as the sensing layer) and the STM tip. Application of V_{bias} allows electrons in the t-WS_2 moiré heterostructure to be manipulated by local tip-gating and to be detected through charging events measured via the tunnel current to the graphene sensing layer.

Conventional STM measurement of the graphene sensing layer provides information on the corrugation of the heterostructure sample as shown in Figure 5-1B. The thin top graphene and hBN bend conformally and thus inherit the topography of the t-WS_2 moiré superlattice. Two sets of moiré superlattices with distinct periods are observed. The larger periodicity (9 nm) originates from the t-WS_2 moiré superlattice which has a twist angle of 58°, while the smaller periodicity (~1.5 nm) corresponds to the moiré superlattice formed by the top graphene and hBN which has a twist angle of 9.6°. The 58° t-WS_2 moiré superlattice exhibits a triangular lattice with three types of high symmetry stacking regions in each unit cell: a bright region ($B^{S/S}$ stacking), a dark region (AB stacking), and a medium height region ($B^{W/W}$ stacking)(*71*) (see Figure 5-1B inset). The bonding arrangements of the $B^{S/S}$, AB, and $B^{W/W}$ stacking orders are sketched on the left side of Figure 5-1B.

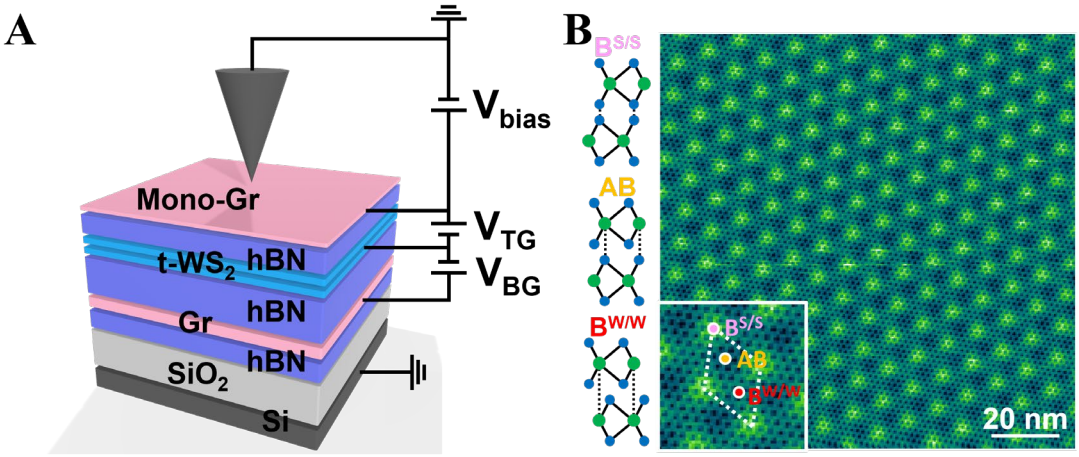

Figure 5-1 SSEC spectroscopy measurement of a moiré superlattice. **A**. Schematic of the dual-gated near-60° twisted bilayer WS_2 (t-WS_2) moiré superlattice device. The top hBN thickness (5nm) is slightly smaller than the moiré lattice constant (9nm). Top gate (V_{TG}) and bottom gate (V_{BG}) voltages are separately applied to independently control the carrier densities in the t-WS_2 superlattice and top graphene sensing layer. **B**. A typical large-scale topography image of the top graphene (V_{bias} = -0.62V and I = 150 pA). Three different stacking regions are labeled in the close-up image in the inset: $B^{S/S}$ stacking (pink dots), AB stacking (yellow dots), and $B^{W/W}$ (red dots). The structures of the $B^{S/S}$, AB, and $B^{W/W}$ stacking are illustrated in the left panel.

Figure 5-2 illustrates the dual role of the STM tip in SSEC spectroscopy. In Figure 5-2A the biased STM tip is seen to act as a local gate on the t-WS_2 because its electrical field partially penetrates the monolayer graphene. This is because graphene has a small electron density of states and weak screening, especially when its Fermi level is near the Dirac point. When the sample-tip bias V_{bias} matches the work function difference between the tip and the graphene the tip exerts no local gating effect (Figure 5-2B). With a decreased (increased) V_{bias}, positive (negative) charge accumulates at the tip apex and generates local band bending in the t-WS_2 due to E-field penetrating through the monolayer graphene (Figure 5-2C and Figure 5-2D). With sufficiently strong band bending a single electron (hole) quasiparticle will be injected into the t-WS_2. The added charge due to this tip-induced quasiparticle excitation will, in turn, alter the tip-graphene tunnel current via long-range Coulomb interactions. SSEC spectroscopy has some similarity to capacitance spectroscopy in that the tip bias voltage drives charging of the t-WS_2. However, unlike conventional capacitance spectroscopy, SSEC spectroscopy locally manipulates individual electrons/holes in the heterostructure and is responsive to individual charge excitation through the tunnel current to the graphene sensing layer. A spatial resolution of ~ 1 nanometer can be achieved in SSEC spectroscopy for thin top hBN layers having a thickness of several nanometers.

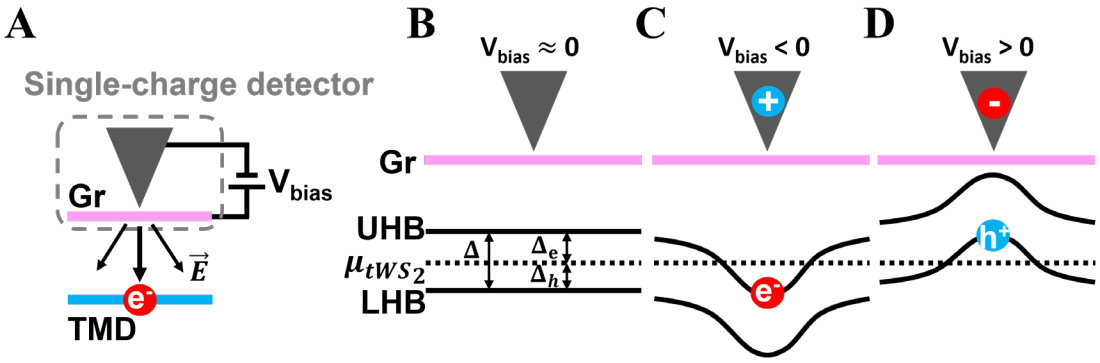

Figure 5-2 Probe mechanism of SSEC spectroscopy. **A**. Illustration of scanning single-electron charge (SSEC) spectroscopy. The electric field from the tip bias partially penetrates the graphene and induces quasiparticle excitations in the t-WS_2. The tip-graphene tunnel junction detects changes in the number of electrons in the t-WS_2 due to long range Coulomb interactions. **B-D**. Illustration of tip-induced quasiparticle excitation in a correlated insulator. Solid curves represent the lower Hubbard band (LHB) and upper Hubbard band (UHB), while dashed line represents the chemical potential μ_{tWS_2}. (**B**) For $V_{bias} \approx 0$, the LHB and UHB are uniform. (**C**) For large $V_{bias} < 0$ the UHB is pushed beneath E_F by tip-gating, inducing a local electron excitation. (**D**) For large $V_{bias} > 0$ tip-gating induces a local hole excitation. For simplicity, we have neglected the work function difference between the tip and the sensing layer graphene in (**B-D**) which may induce a small offset for V_{bias}. The gap between the UHB and LHB is labeled as Δ while the gap between μ_{tWS_2} and UHB (LHB) is labeled as Δ_e (Δ_h).

5.3 Local Thermodynamic Probe of Correlated Electrons

This SSEC spectroscopy enables us to perform a local thermodynamic measurement of the moiré correlated states. To see this, we first performed a backgate (V_{BG}) dependent scanning tunneling spectroscopy measurement on the sample surface. Figure 5-3 shows the V_{BG} dependence of the dI/dV spectra of the tip-graphene tunnel junction when the tip is placed over the $B^{S/S}$ site of the moiré unit cell. We started by setting the top gate voltage to $V_{TG} = 0.52V$, which shifts the t-WS_2 chemical potential up to the conduction band edge while keeping the graphene Fermi level close to the Dirac point(*101*). Under these conditions increasing the backgate voltage, V_{BG}, increases the global electron doping in the t-WS_2 layers. The resulting dI/dV measurement of the sensing layer is dominated by a broad increase in the dI/dV signal for increased V_{bias} regardless of polarity, which mostly reflects the local density of states of graphene and does not show an obvious dependence on V_{BG} (i.e. on the t-WS_2 doping).

The impact of electrical charge added to the t-WS_2 moiré superlattice is better seen by normalizing the dI/dV spectra at each V_{BG} by the averaged dI/dV spectrum (which average out the fast-changing charging peaks). The normalization process is described as follows. We divide the raw dI/dV spectra (several typical raw dI/dV spectra are shown in Figure 5-4A as red curves) by the averaged dI/dV spectra over all V_{BG} values (blue curve

in Figure 5-4A) to obtain the normalized dI/dV spectra. Several typical normalized dI/dV spectra are shown in Figure 5-4B.

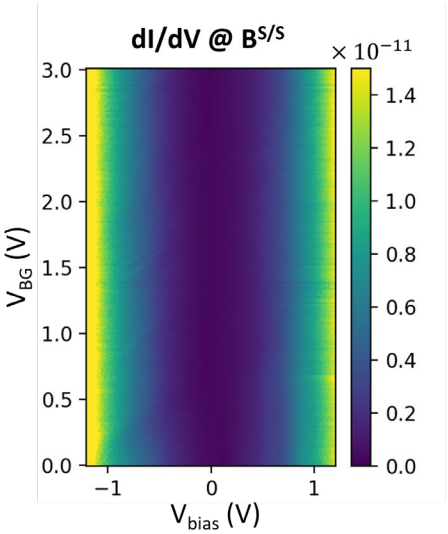

Figure 5-3 STS on the graphene sensing layer. dI/dV spectra measured on the graphene sensing layer as a function of sample-tip bias (V_{bias}) and backgate voltage (V_{BG}) (measured with tip held over the t-WS_2 $B^{S/S}$ site). V_{TG} is fixed at 0.52V.

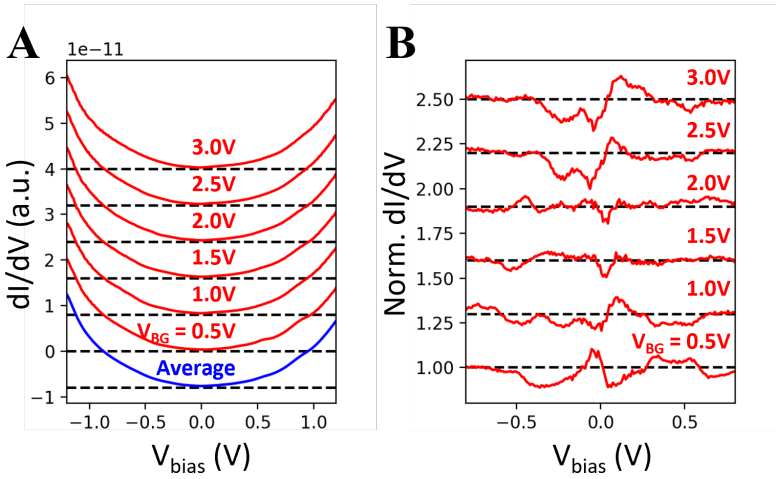

Figure 5-4 Normalization of the V_{BG}-dependent dI/dV spectra. **A**. The red curves show typical dI/dV spectra measured at different V_{BG}, while the blue curve shows the mean dI/dV spectra averaged over all individual spectra (). **B**. Normalized dI/dV spectra obtained by dividing the raw spectra (red curves) by the averaged spectra (blue curves) shown in (**A**). Spectra in (**A,B**) are shifted vertically for clarity, with the corresponding zero reference point labeled by black dashed lines.

Using the normalization process mentioned above, we can obtain the complete normalized dI/dV spectra 2D plot as a function of V_{BG} (Figure 5-5A) which removes the broad rising background and reveals multiple dispersive bright lines that correspond to

peaks in dI/dV that shift in energy with applied V_{BG}. These peaks are clustered around several electron doping levels in the t-WS_2 moiré superlattice (i.e., different V_{BG} values), as denoted by horizontal arrows in Figure 5-5B. Their V_{BG} values correspond to t-WS_2 electron filling factors of n = 0, 1/3, 2/3, 1 (as labeled in red), where n is the number of electrons per moiré site. The filling factors shown here are based on carrier densities extracted using the device capacitance as described in reference(*101*). Our SSEC imaging (see next section) is also consistent with these filling factors.

The dI/dV spectra of Figure 5-5A show two or more dispersive lines clustered around each correlated insulating state at n = 1/3, 2/3, and 1. To better understand this behavior Figure 5-5B shows higher resolution V_{BG}-dependent dI/dV spectra near the n = 2/3 generalized Wigner crystal state (the phase space inside the white dashed box in Figure 5-5A). Two bright dispersive lines with similar slope move together through the V_{BG} region associated with the n = 2/3 state, as well as several weaker features nearby. Figure 5-5C displays a horizontal line cut of Figure 5-5B at V_{BG} = 1.60V, where clear dI/dV peaks (labeled with vertical arrows) can be observed at the V_{bias} positions of the bright lines in Figure 5-5B. These dI/dV peaks do not mark the energy locations of resonances in the local density of states (LDOS), but rather arise from electron and hole charging events in the generalized Wigner crystal states of t-WS_2.

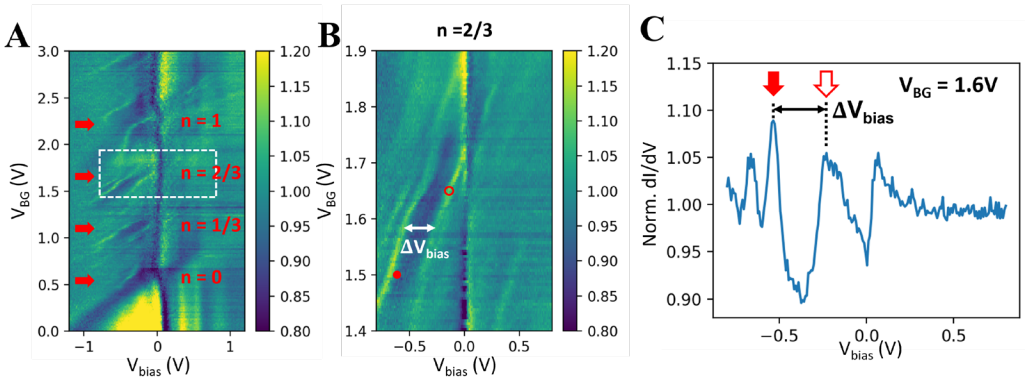

Figure 5-5 Normalized dI/dV spectra 2D plot. **A**. Normalized form of the dI/dV spectra shown in a. The dI/dV spectrum at each V_{BG} is normalized by the average dI/dV spectrum for all V_{BG} values (see SI for details). Dispersive bright lines corresponding to dI/dV peaks are clustered around the filling factors n = 0, 1/3, 2/3, 1 (labeled in red). **B**. High-resolution dI/dV spectra corresponding to the n = 2/3 state measured over the range enclosed by the white box in (**A**). **C**. dI/dV line-cut of c at V_{BG} = 1.60V shows peaks corresponding to dispersive features in (**B**) labeled with a solid arrow (electron charging) and an open arrow (hole charging) that are offset from each other by ΔV_{bias}.

To understand this, we look to the sketch in Figure 5-6A that illustrates the charging diagram of the t-WS_2 moiré superlattice in the n = 2/3 state. There are three different regimes as shown in Figure 5-6B: the "intrinsic" generalized Wigner crystal insulator phase (I) (solid red dots mark the locations of electrons in the moiré unit cell while open circles mark empty cells), the electron excitation regime (E) where an electron (blue solid dot in Figure 5-6B) is injected below the tip at a large negative V_{bias}, and the hole excitation regime (H) where a hole (blue open circle in Figure 5-6B) is injected at a large

positive V_{bias}. These regimes are separated by two dispersive lines in the V_{BG}-V_{bias} parameter space in Figure 5-6A with the slope of the dispersive lines being determined by the efficiency of the tip as an effective top gate relative to chemical potential shifts induced by the bottom gate. Starting from the intrinsic regime (e.g., Figure 5-2B), a reduction of V_{bias} causes the tip to become positively charged. Crossing the boundary from (I) to (E) corresponds to pushing the UHB energetically below the t-WS_2 chemical potential μ_{tWS_2} and locally inducing an electron charging event (Figure 5-2C). Similarly, if V_{bias} is increased and crosses the boundary from (I) to (H) then the LHB is energetically pushed above μ_{tWS_2}, resulting in a local hole charging event (Figure 5-2D). These charge excitations alter the tunnel junction conductance and result in a peak in the dI/dV spectra. The dispersive dI/dV peaks in Figure 5-5B and Figure 5-5C correspond to the electron/hole excitation boundaries sketched in Figure 5-6A. The reason that the intrinsic region does not bracket $V_{bias} = 0$ is most likely because of the work function difference between the tip and the graphene sensing layer. Additional weaker dI/dV peak features observed in Figure 5-5B at higher positive (negative) V_{bias} correspond to the injection of additional electrons and holes at nearby moiré cells adjacent to the tip location.

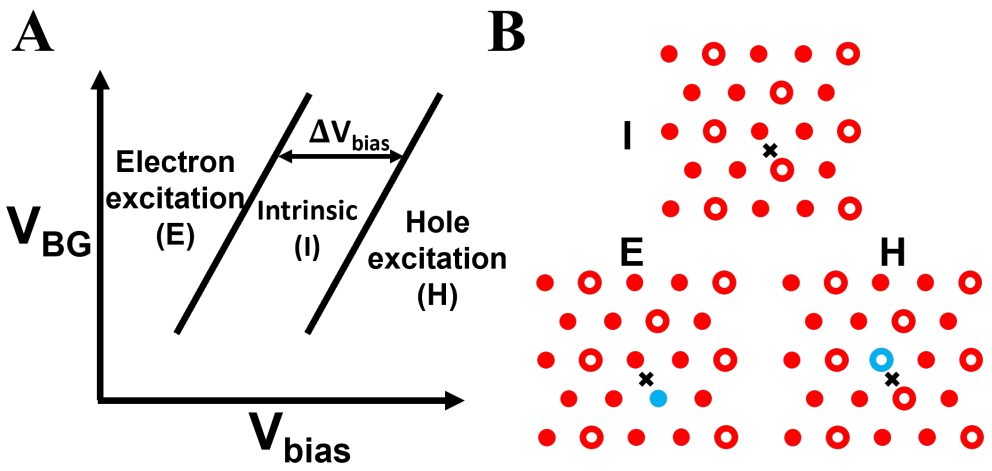

Figure 5-6 Thermodynamic measurement enabled by SSEC spectroscopy. **A**. Schematic shows the charging regimes of the t-WS_2 moiré superlattice near the n = 2/3 state. (I) marks the intrinsic generalized Wigner crystal insulator phase, (E) marks the electron excitation regime, and (H) marks the hole excitation regime. The charging regimes are separated by two dispersive lines in the V_{BG}-V_{bias} parameter space that are offset from each other by ΔV_{bias}. **B**. Real space sketch of the intrinsic (I), electron excitation (E), and hole excitation (H) regimes. Electron-filled sites (solid dots) and empty sites (open circles) of the n = 2/3 generalized Wigner crystal as shown. Tip-induced electron excitation is marked by a solid blue dot and hole excitation by a blue open circle. The back cross labels the tip position.

5.4 Mapping Electron and Hole Excitations of Generalized Wigner Crystals

To establish our assignment of the features seen in the last section (Figure 5-5) as electron and hole excitations of the generalized Wigner crystal, we directly image these charging events using SSEC spectroscopy. Figure 5-7A displays an STM topography image of a highly defect-free t-WS_2 moiré region chosen for imaging electron/hole excitations. Figure 5-7B shows a dI/dV map measured over this same area at V_{BG} = 1.50V, V_{TG} = 0.52V, and V_{bias} = -0.59V, which corresponds to the electron excitation boundary denoted by the filled circle in Figure 5-5B. A triangular lattice of bright dots is seen with a period larger than the underlying moiré superlattice by a factor of $\sqrt{3}$. This new triangular lattice reflects the wavefunction distribution of the excited electron in the generalized n = 2/3 Wigner crystal. To confirm that this pattern originates from tip-induced electron excitations we tested how it evolves with V_{bias}. A typical aspect of charging features is "ring expansion" with increased bias(*39, 79-81, 102*) because the tip can then induce charging events from more distant positions. Figure 5-7D-G show the evolution of the charging rings with increasing $|V_{bias}|$, obtained at V_{BG} = 1.50V and V_{TG} = 0.52V. The electron charging signal at the different moiré unit cells is seen to expand into a wide charging ring with increasingly negative V_{bias}, precisely as expected for electron injection.

Figure 5-7C shows a dI/dV map taken at the hole excitation boundary for n = 2/3 filling, corresponding to the open circle in Figure 5-5B (V_{BG} = 1.65V, V_{TG} = 0.52V, and V_{bias} = -0.14V). A honeycomb lattice of bright dots (open circles) here reflects the wavefunction of hole excitations in this generalized Wigner crystal. The tip bias dependence of this pattern also confirms its origin as shown in Figure 5-7H-K. Here the hole charging signal in the different moiré unit cells is seen to expand into a wider charging ring for increasingly positive V_{bias}.

The complementarity of the electron and hole excitation wavefunctions of the generalized Wigner crystal state can be seen by overlaying the hollow circles and solids dots of Figure 5-7B,C onto the topography of Figure 5-7A. Both the hollow *and* solid circles are seen to be localized in the $B^{W/W}$ stacking regions, where the lowest-energy conduction moiré flat bands are predicted to reside(*71*). The electron excitation distribution (red dots) and the hole excitation distribution (open circles) combine perfectly to yield the full moiré superlattice. Hole excitations correspond precisely to the filled electron locations for an n = 2/3 generalized Wigner crystal (i.e., a honeycomb lattice) whereas electron excitations occur at the hollow centers of the honeycomb lattice. This is the pattern that one might intuitively expect from classical electrostatic reasoning.

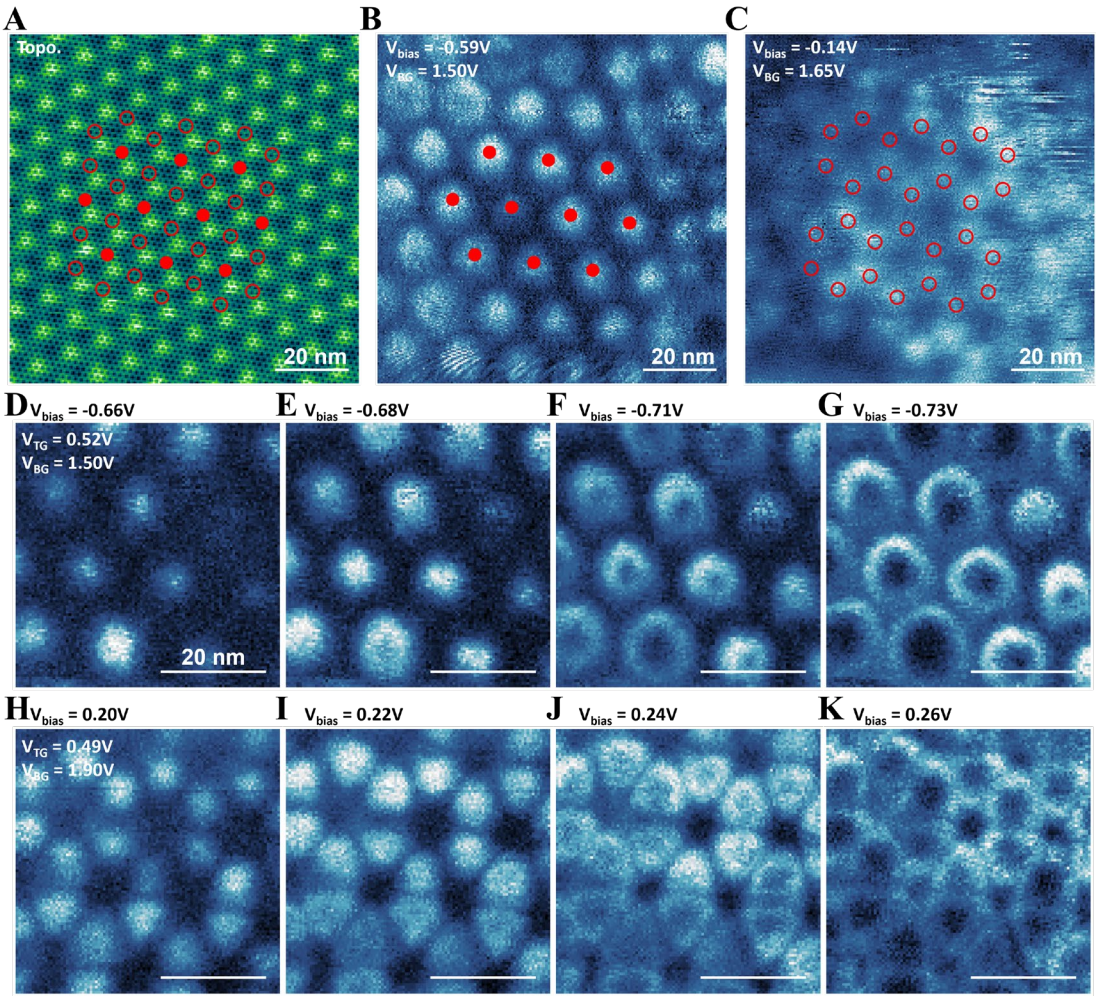

Figure 5-7 Mapping electron and hole excitations of the n = 2/3 generalized Wigner crystal. **A**. STM topography image of graphene sensing layer shows the t-WS2 moiré superlattice (V_{bias} = -0.59V, I = 150pA). **B**. dI/dV map of same area as (**A**) for applied voltages corresponding to the electron excitation boundary (V_{BG} = 1.50V, V_{TG} = 0.52V, V_{bias} = -0.59V). Sites of electron excitations are marked with solid red dots. **C**. dI/dV map of same area as (a) for voltages corresponding to the hole excitation boundary (V_{BG} = 1.65V, V_{TG} = 0.52V, V_{bias} = -0.14V). Sites of hole excitations are marked with open circles. **D-G**. Evolution of dI/dV maps of the electron charging peak of the n = 2/3 state with increasingly negative V_{bias}. The electron charging signals widen into a growing circle at each moiré site as V_{bias} becomes more negative. **H-K**. Evolution of dI/dV maps of the hole charging peak of the n = 2/3 state with increasingly positive V_{bias}. The hole charging signal widens into a growing circle as V_{bias} becomes more positive. The solid dots in (**B**) and open circles in (**C**) are overlaid in (**A**) and are seen to be perfectly complementary. (**D-K**) share the same scale bar.

5.5 Determining the Thermodynamic Gaps of Generalized Wigner Crystals

In this section, we will try to quantitatively determine the thermodynamic gaps of these Wigner crystal states from our SSEC spectroscopy measurements. Since the thermodynamic gap of a correlated state is the chemical potential difference for adding a single hole or electron, it is possible to extract the thermodynamic gap of generalized Wigner crystals from our SSEC spectra. To see this we define the energy difference between the chemical potential and LHB as Δ_h (Figure 5-2B), and the bias applied to the tip to create a hole excitation as V_h. We then write $\Delta_h = \alpha_h e V_h$, where α_h is a geometric constant defined by the tip-gating efficiency when the tip is above a hole site (e is the charge of an electron). Similarly, we can write $\Delta_e = \alpha_e(-e)V_e$ where Δ_e is the energy difference between the chemical potential and UHB, and the factors V_e and α_e are defined for electron excitations. If $\alpha_e = \alpha_h = \alpha$, then the thermodynamic gap, $\Delta = \Delta_e + \Delta_h$, can be written as

$$\Delta = \alpha e(V_h - V_e) = \alpha e \Delta V_{bias}, \tag{5.1}$$

where ΔV_{bias} is the experimental sample-tip bias difference measured between the hole excitation and electron excitation boundaries as shown in Figure 5-6A. A key requirement in this analysis is that the capacitive coupling between the tip and surface is equivalent for electron and hole excitations (i.e., $\alpha_e = \alpha_h$). This requirement is satisfied in the measurements shown in Fig. 2 which were performed with the tip positioned above the $B^{S/S}$ site in the t-WS_2 moiré unit cell, which is the same distance to the nearest excited electron or hole.

In order to obtain a quantitative value of the generalized Wigner crystal thermodynamic gap, Δ, we must determine the value of α. This is obtained through numerical simulation of the tip-surface electrostatics, which will be discussed in detail in section 5.6. The simulation yields a value of $\alpha = 0.16 \pm 0.02$. From Eq. (5.1) this results in the following experimental thermodynamic gaps for the n = 1/3, 2/3, and 1 correlated states: $\Delta_{n=1/3} = 52 \pm 8\text{meV}$, $\Delta_{n=2/3} = 47 \pm 8\text{meV}$, and $\Delta_{n=1} = 107 \pm 16\text{meV}$ (the uncertainty here is calculated from both the standard deviation in our measurement of ΔV_{bias} and the uncertainty in the simulation of α).

5.6 Electrical Simulation of the Tip Coupling Constant

We note that to obtain the tip coupling constant α here is a nontrivial task which is essentially different from the one performed in section 3.6. The reason is that the existence of the screening by Dirac electrons in the graphene sensing layer makes the simulation more complicated.

Here we introduce details for the electrostatic simulation of the tip-t-WS_2 coupling constant α, including a graphene quantum capacitance effect. As illustrated in Figure 5-8A, the tip is approximated by be an ideal metallic cone with a half cone angle θ and tip height h (separation between tip apex and the graphene surface). The backgate graphite is modeled by an infinitely large metallic plate. The t-WS_2 moiré heterostructure is regarded as a thin insulator since it is in a correlated insulating state. The t-WS_2 is incorporated into the surrounding hBN and regarded as an insulator with the same

dielectric constant as the hBN. The graphene is modeled by a special boundary condition whose electrical potential V_{Gr} is related to its charge density ρ_{Gr} due to the graphene quantum capacitance: $V_{Gr} = V_{Gr}(\rho_{Gr})$, as described below.

The graphene surface electrical potential $V_{Gr}(\rho_{Gr})$, namely its vacuum level, can be determined in the following way. Since the graphene is connected to a voltage source, meaning its chemical potential is fixed externally, then the change of the graphene surface electrical potential $\Delta V_{Gr} = V_{Gr} - V_{Gr0}$ can be determined as $\Delta V_{Gr} = \Delta E_f / e$, where $\Delta E_f = E_f - E_{f0}$ is the graphene Fermi level change. Here V_{Gr0} and E_{f0} are the graphene surface electrical potential and Fermi level at charge neutrality ($\rho_{Gr} = 0$). For simplicity, we assume $V_{Gr0} = 0$ and $E_{f0} = 0$. Therefore, we have $V_{Gr} = E_f / e$. The relation between the graphene Fermi level E_f and its carrier density n_{Gr} is determined by

$$n_{Gr} = \begin{cases} \int_0^{E_f} DOS_{Gr}(E)dE\,, & (E_f \geq 0) \\ \int_{E_f}^{0} DOS_{Gr}(E)dE\,, & (E_f < 0) \end{cases}, \tag{5.2}$$

where $DOS_{Gr}(E) = \frac{2}{\pi} \cdot \frac{|E|}{(\hbar v_F)^2}$ is the graphene density of states per unit area. Here $v_F = 10^6 m/s$ is the Femi velocity of the graphene. Using $\rho_{Gr} = -en_{Gr}$, we obtain the following boundary condition for the graphene plane

$$V_{Gr}(\rho_{Gr}) = \begin{cases} \frac{\sqrt{\pi}\hbar v_F}{e} \cdot \sqrt{-\frac{\rho_{Gr}}{e}}, & (\rho_{Gr} < 0) \\ -\frac{\sqrt{\pi}\hbar v_F}{e} \cdot \sqrt{\frac{\rho_{Gr}}{e}}, & (\rho_{Gr} \geq 0) \end{cases}, \tag{5.3}$$

This boundary condition reflects the quantum capacitance of the graphene and its partial screening effect.

In the simulation, the boundary conditions for the tip and backgate are set at $V = V_{bias}$ and $V = V_{BG}$, respectively. To make the simulation more computable we have a cylindrically truncated grounded surface enclose the simulation center. The dielectric constants in the region above and below the graphene are set to $\varepsilon_{vac} = \varepsilon_0$ and $\varepsilon_{hBN} = 4.2\varepsilon_0$, respectively, where ε_0 is the vacuum dielectric constant.

We note that although the tip height and tip cone angle are two independent parameters, they work together to control the value of α for the charged site. Therefore, in the simulation we fix one parameter and tune the other parameter to fit the experiment results. Here we fix the tip height at $h = 1nm$ and vary the value of θ. This selected tip height is close to the STM tip tunneling distance used in the experiment. However, we note that the selection of h here does not significantly affect the final obtained values for α and β, as discussed later. In the simulation α and β are obtained via monitoring the responses of the electrical potential change $\Delta\Phi$ at the position of the charged site ($r = 5.4nm$ when the tip is fixed at the three-site symmetric point) in the TMD layer with the following parameters: α: V_{bias} = 145mV and V_{BG} = 0, and β: V_{bias} = 0 and V_{BG} = 71 mV.

The simulated electrical potential map at V_{bias} = 0 and V_{BG} = 71mV is shown in Figure 5-8B while the simulated electrical potential map at V_{bias} = 145mV and V_{BG} = 0 is shown in Figure 5-8C.

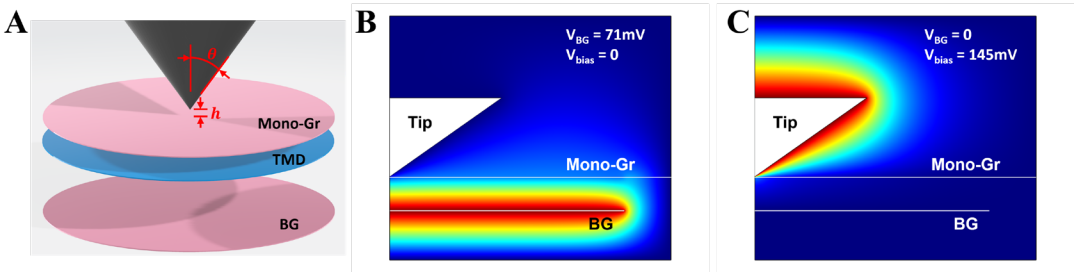

Figure 5-8 Electrostatic simulation of the tip-TMD coupled system. **A**. Schematic of the simulation model. The tip is represented by an ideal metallic cone with half cone angle θ and tip height h (separation between tip apex and the graphene surface). The backgate is modeled by an ideal metallic plate. The graphene is modeled as follows: We set the boundary conditions on the graphene surface to be that the electrical potential is determined by the charge density so that the quantum capacitance of the graphene can be correctly treated. **B,C**. Simulated electrical potential with (**B**) V_{BG} = 71mV and V_{bias} = 0, and (**C**) V_{BG} = 0 and V_{bias} = 145mV. The simulation parameters used are $\theta = 54.95°$ and $h = 1nm$. The position of the t-WS_2 layer is not depicted here since it is regarded as an insulator with a dielectric constant equivalent to that of hBN.

The simulated ratio between α and β can be compared with the experimentally measured charging peak slope $\frac{\alpha}{\beta} = 0.507$. The parameters that yield results most consistent with experimental results are as follows: $\theta = 54.95°$, and $h = 1nm$ (Figure 5-9A). The simulated tip coupling constant (α) and backgate coupling constant (β) are $\alpha = 0.16$ and $\beta = 0.32$ for the charged site in the TMD layer ($r = 5.4nm$). We note that this simulated coupling constant is close to values reported in previous work(*102*).

The potential response of the charged site $\Delta\Phi$ is not exactly linear with the change of V_{bias} and V_{BG}. This is shown in Figure 5-9B ($\Delta\Phi$ as a function of V_{bias}) and Figure 5-9C ($\Delta\Phi$ as a function of V_{BG}). This effect occurs because at large tip bias or backgate voltage the graphene is strongly doped and has a larger density of states at the Fermi level and behaves more like a metal. However, in the measurement range V_{bias} < 200mV and V_{BG} <100mV the response can still be approximately regarded as being linear.

The selection of the tip height does not significantly affect the final value for α in the simulation process above. This is seen in Figure 5-9D and Figure 5-9F, which show the simulated tip cone half angle θ (Figure 5-9D) and the corresponding α values (Figure 5-9F) for different tip heights. Including the uncertainty in the top hBN thickness and the hBN dielectric constant, we have an estimated value of $\alpha = 0.16 \pm 0.02$.

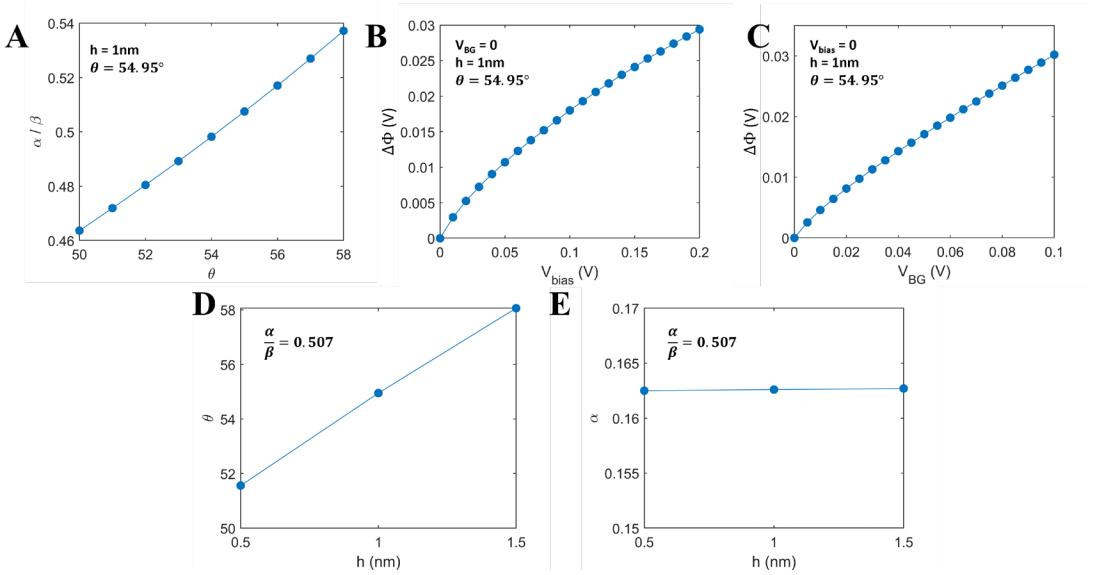

Figure 5-9 Determination of the tip coupling constant α. **A**. Simulated ratio α/β as a function of θ at h = 1nm. Here α (β) is obtained through monitoring the potential change $\Delta\Phi$ at r=5.4nm in the TMD layer by setting V_{bias} = 145mV and V_{BG} = 0 (V_{bias} = 0 and V_{BG} = 71mV). **B**. Potential change $\Delta\Phi$ at r=5.4nm in the TMD layer for different V_{bias} values at V_{BG} = 0. **C**. Potential change $\Delta\Phi$ at r=5.4nm in the TMD layer for different V_{BG} values at V_{bias} = 0. h = 1nm and $\theta = 54.95°$ for both (**B**) and (**C**). **D**. Fitted values for θ as a function of the tip height h with the ratio α/β fixed at 0.507. **E**. Fitted values for α as a function of the tip height h with the ratio α/β fixed at 0.507. The fitted value for α is nearly independent of the selected tip height h.

5.7 Summary and Outlook

In summary, in this chapter we have demonstrated the non-invasive high-resolution SSEC spectroscopy technique that enables us to study the local electron/hole excitations in 2D generalized Wigner crystal systems. It further allows us to measure the local thermodynamic gaps of generalized Wigner crystals having different filling factors and to map their electron and hole excitations. Particularly, among all the microscopic thermodynamic measurement techniques, this one has realized the highest spatial resolution (sub-nm). This technique should be broadly applicable to the characterization of other fragile correlated electron systems.

6 Visualizing In-plane Charge-Transfer Moiré Excitons

6.1 Introduction and Background

In Chapter 4 and 5, we studied the microscopic nature of the ground states for interacting moiré electrons, e.g. Mott insulator and Wigner crystals. However, the interaction between electrons can also induce a wide range of important excited states and non-equilibrium quantum phenomenon. One of the typical examples is the exciton physics, which has been studied for many years in pristine TMD materials. The presence of a moiré superlattice can greatly modify how electron and hole are bound with each other and lead to the emergence of new exotic exciton states, which will be studied in this chapter.

TMD moiré superlattices exhibit rich quantum phenomena(*15, 48, 74, 90, 101, 113-117*) that include exotic excited states such as moiré excitons(*114-118*). The moiré superlattice has a significant effect on strongly interacting electron-hole bound states, signatures of which have been observed through various optical spectroscopic studies(*114-117*). However, a clear understanding of the microscopic structure of moiré excitons and their non-equilibrium dynamics at the moiré scale remains elusive. Imaging moiré excited states is experimentally challenging because it requires probing transient excited states with nanometer spatial resolution, which is beyond the capability of typical optical spectroscopy techniques. Recently, moiré excitons have also been studied using photoemission spectroscopy(*118*) and electron excitation(*119*), but such measurements still cannot spatially resolve the internal structures of the photoexcited holes and electrons. Combining laser excitation with scanning tunneling microscopy (termed laser-STM) provides a means to overcome this challenge. Laser-STM was pioneered in previous studies of individual molecules and has enabled atomic-scale imaging of molecular photo-response(*119-122*). It has also been utilized for the study of conventional bulk semiconductors(*123-128*). Here we employ laser-STM to directly image the internal microscopic structure of moiré excitons.

A moiré superlattice modifies exciton behavior in different ways depending on the strength and shape of the moiré potential. Weak moiré potentials, for example, generate Umklapp scattering of the pristine Wannier excitons that leads to some spatial modulation while retaining their overall Wannier characteristics(*129*). Strong moiré potentials, such as those created by strain-induced reconstructions in TMD bilayers, not only induce Umklapp scattering of excitons but can also alter the internal structure of moiré excitons(*115*). For example, if the photoexcited electron and hole feels different moiré potentials, with minima located at different positions, a new type of in-plane charge transfer (ICT) moiré exciton can emerge(*115, 130*). Here we describe measurements employing laser-STM that probe the microscopic structure of such exciton states and demonstrate the presence of ICT moiré excitons in near-60-degree twisted WS_2 (t-WS_2) bilayers. Our scanning tunneling spectroscopy (STS) and *ab initio* calculations

reveal a strong moiré potential in t-WS_2 that causes the single-particle electron and hole states to be confined to different positions within a moiré unit cell. Combining laser excitation with STM enables us to perform photocurrent tunneling microscopy (PTM) imaging of t-WS_2 photoexcited excitons with sub-nm spatial resolution. Our tunneling photocurrent maps show spatially alternating behavior with opposite current polarities located at different positions within the moiré unit cell even for the same STM bias voltage. Such behavior provides direct evidence of ICT excitons by showing spatial separation of the excited electron and hole. Positive tunnel current occurs when the STM tip is above a hole position and negative current occurs when the tip is above an electron position. Our experimental results agree well with the *ab initio GW*-BSE calculations of the lowest-energy exciton wavefunctions in t-WS_2 moiré superlattices. The *ab initio* calculations are performed by extending a recently developed novel computational method(*115*) designed to fully account for the electron-hole interaction of all ~4000 atoms in the reconstructed moiré unit-cell.

The work described chapter is the result of a close collaboration multiple experimental and theoretical groups including the Wang group, Crommie group and Louie group. Particularly. The experimental work is mainly performed by Ziyu and me while the theoretical simulation is mainly finished by Mit.

6.2 Device and Setup

We chose a near-60-degree t-WS_2 moiré superlattice to study ICT moiré excitons because our *ab initio* calculations predict that it should feature a moiré potential where conduction and valence band edge state wavefunctions are confined to different positions within the moiré unit cell (illustrated in Figure 6-1A), thus providing an ideal platform to host ICT excitons. Figure 6-1B shows an illustration of our gate-tunable t-WS_2 device and laser-STM setup. The optical images of the tip-sample tunneling junction are shown in Figure 6-1C (white light illumination) and Figure 6-1D (520nm laser illumination). The t-WS_2 sits on top of a 49 nm thick layer of hexagonal boron nitride (hBN) which is placed above a graphite back gate. A back gate voltage (V_{BG}) is applied between the t-WS_2 and the graphite back gate to control the carrier density in the t-WS_2. We follow the method introduced in Chapter 2 and place a graphene nanoribbon array electrode on the t-WS_2 surface to make the sample conductive enough(*64*). A bias voltage (V_{bias}) is applied to the t-WS_2 relative to the STM tip. The device fabrication follows the same procedure as the one described in section 2.2.

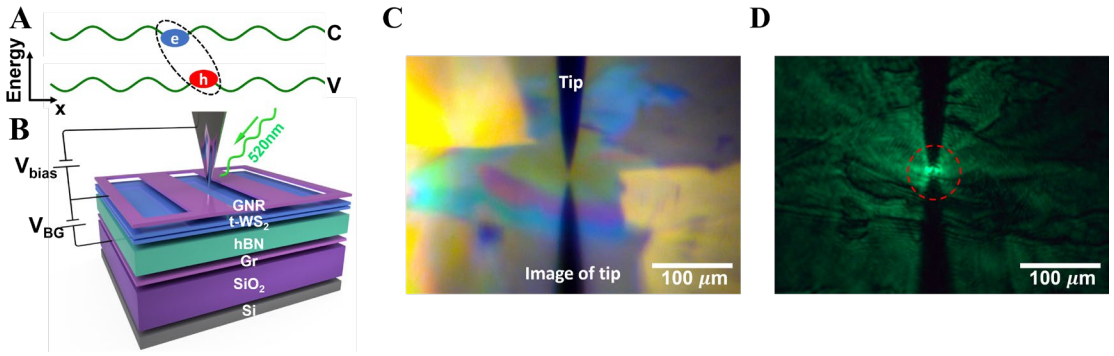

Figure 6-1 Laser-STM measurement of a twisted bilayer WS_2 moiré superlattice. **A**. Sketch of band-edge energies as a function of real-space position (lines) as well as the location of the excited electron and hole position of an in-plane charge-transfer (ICT) exciton. The moiré superlattice modulates the pristine unit-cell conduction band edge (labeled C) and valence band edge (labeled V) so that electrons and holes are concentrated in separate regions. **B**. Sketch of experimental setup for laser-STM measurement of a near-58-degree twisted bilayer WS_2 (t-WS_2) device. The t-WS_2 is placed on top of 49nm thick hBN and a graphite substrate (these serve as the gate dielectric and back gate). A back gate voltage V_{BG} is applied between the t-WS_2 and the graphite back gate. A graphene nanoribbon (GNR) array is placed on top of the t-WS_2 to serve as the contact electrode. A sample-tip bias V_{bias} is applied between the t-WS_2 and the STM tip to induce a tunnel current. A 520nm wavelength continuous-wave laser is focused on the tip tunnel junction. **C**. Optical image for gated twisted WS_2 device and laser-STM setup using white light illumination. The positions of the tip and its reflected image by the substrate are labeled. **D**. Optical image of the device and setup with a 520nm continuous-wave laser focused onto the tip-sample tunneling junction. The laser spot (diameter ~10μm) is labeled with a red dashed-line circle.

Figure 6-2A shows a typical STM topography image of the t-WS_2 surface and features a moiré superlattice with a moiré period of ~9 nm. Three high-symmetry stacking regions can be seen within the moiré unit cell: the dark (bright) areas correspond to AB ($B^{S/S}$) stacking regions while the intermediate height area is a $B^{W/W}$ stacking region. Model structures for the AB, $B^{S/S}$, and $B^{W/W}$ stacking regions are illustrated in Figure 6-2B. This topography agrees well with our calculated height distribution map (Figure 6-2C) and arises due to an out-of-plane reconstruction that leads to strong variation in the local interlayer spacing (see SI for details). The $B^{S/S}$ stacking regions have the largest interlayer spacing due to steric hindrance arising from the S atoms of the top and bottom layers facing each other(*71*). In-plane reconstruction of the superlattice leads to a noticeably larger area for the low-energy AB stacking region and results in strain redistribution in the two WS_2 layers (shown in Figure 6-2D). The final relaxed structure reflects a trade-off between the energy gain from forming large-area AB stacking regions and the energy cost of strain redistribution.

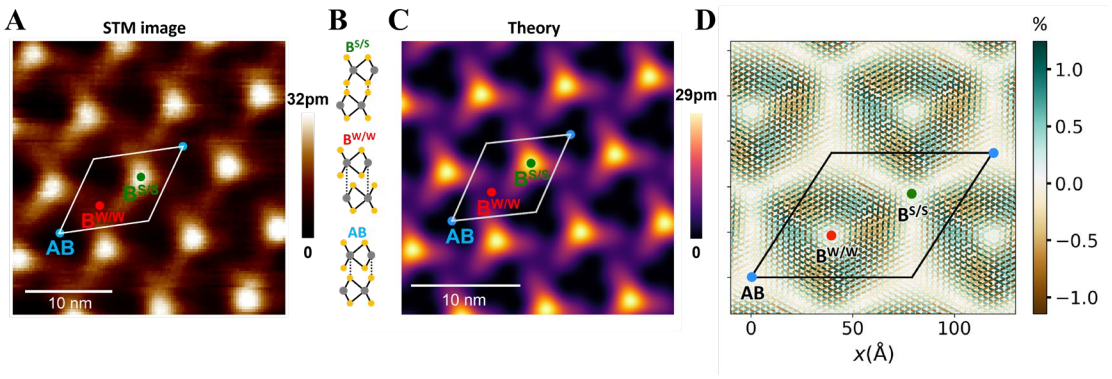

Figure 6-2 Topography for the t-WS_2 moiré superlattice. **A**. A typical STM topography image of the t-WS_2 surface exhibits the triangular moiré lattice. V_{bias} = -4V, I = 100pA. Three high-symmetry stacking regions are labeled with solid dots: $B^{S/S}$, $B^{W/W}$, and AB. **B**. Illustration of the $B^{S/S}$, $B^{W/W}$, and AB stacking structures (yellow and gray dots represent S and W atoms respectively). **C**. Theoretically calculated surface height variation for t-WS_2. C. Simulated strain redistribution in the bottom layer of the moiré superlattice. The strain is plotted as the percentage change in the local W-W distance from the pristine monolayer lattice constant.

6.3 Electronic Structure Revealed by Scanning Tunneling Spectroscopy

We first characterized the single-particle electronic structure of t-WS_2 by measuring scanning tunneling spectroscopy (STS) and comparing it to theoretical calculations. Figure 6-3A shows the calculated electronic band structure of a t-WS_2 moiré superlattice with 9nm period including spin-orbit coupling. Here we are mainly concerned with the moiré flat bands at the valence band top (VBT) (labeled v1) and the conduction band bottom (CBB) (labeled c1), which host the lowest-energy holes and electrons, respectively. The computed flat bands arise from a deep triangular quantum well potential due to the inhomogeneous layer hybridization and structural reconstruction(*71, 131*) which yield narrow bandwidths of 1 meV and 5 meV for the v1 and c1 bands, respectively. The v1 band is derived from states near the Γ point in the pristine unit-cell Brillouin zone (BZ) and is two-fold degenerate, while the c1 states are folded from around the Q point of the pristine unit-cell BZ and comprise two closely spaced bands (each with six-fold degeneracy). The small splitting in energy of these two sets of c1 bands is induced by interlayer hybridization. The spatial distribution of these moiré flat bands is experimentally reflected by the dI/dV spectra measured at the $B^{W/W}$ and AB sites (Figure 6-3B and Figure 6-3E). On the valence band side (Figure 6-3B) the AB site shows a sharp peak around V_{bias} = -1.75V while the $B^{W/W}$ site exhibits almost no signal until V_{bias} = -1.85V, indicating that the two-fold degenerate v1 band is mainly localized on the AB site. This spatial distribution was confirmed by dI/dV mapping measured at V_{bias} = -1.75V (Figure 6-3C) which matches the calculated v1 band's charge density (ρ) distribution (Figure 6-3D), both of which show maximum density at the AB site. On the conduction band side (Figure 6-3E), the lowest energy dI/dV peak appears at the $B^{W/W}$ site at V_{bias} = 0.60V while the AB site exhibits a small signal until V_{bias} = 0.75V,

indicating that the c1 band states are mainly localized on the $B^{W/W}$ site. This was also confirmed by dI/dV mapping measured at V_{bias} = 0.62V (Figure 6-3F) which matches the calculated c1 bands' charge density distribution (Figure 6-3G), both of which show maximum density at the $B^{W/W}$ site. These results show that a strong moiré potential exists in t-WS_2 and that the lowest-energy single-particle electron and hole states are spatially separated.

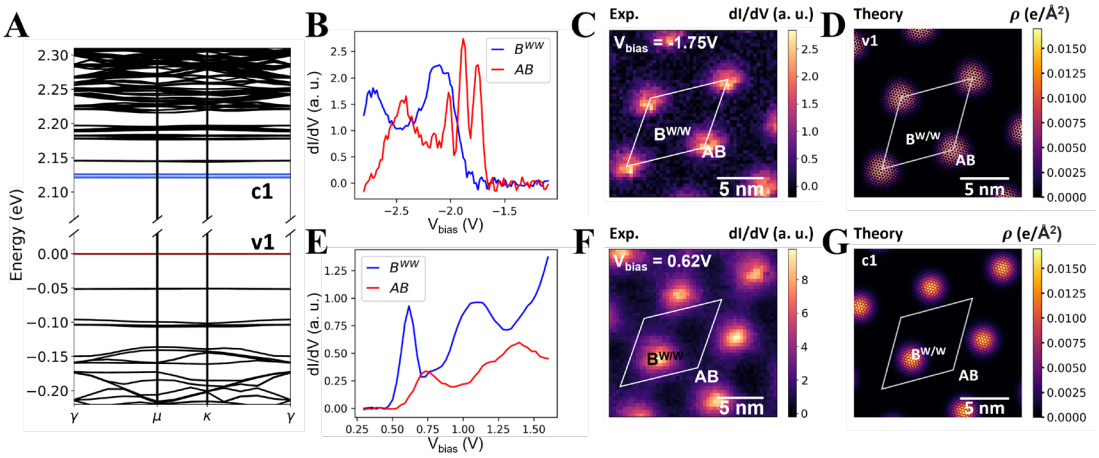

Figure 6-3 Electronic structure of twisted bilayer WS_2. **A**. Calculated electronic band structure for the t-WS_2 moiré superlattice. The moiré flat bands at the valence band top (VBT) and conduction band bottom (CBB) are labeled v1 and c1. **B**. dI/dV spectra measured at the $B^{W/W}$ (blue) and AB (red) stacking sites for the valence band. The AB site shows a first sharp peak near V_{bias} = -1.75V. (**C**) t-WS_2 dI/dV map measured at V_{bias} = -1.75 V and (**D**) calculated charge density (ρ) distribution for v1 both show strong hole localization at the AB site. V_{BG} = -2V for (**B,C**). **E**. dI/dV spectra measured at the $B^{W/W}$ (blue) and AB (red) stacking sites for the conduction band. The $B^{W/W}$ site shows a first sharp peak near V_{bias} = 0.60V. (**F**) t-WS_2 dI/dV map measured at V_{bias} = 0.62V and (**G**) calculated charge density (ρ) distribution for c1 both show strong electron localization at the $B^{W/W}$ site. V_{BG} = 1.5V for (**E,F**).

6.4 Charged-transfer Exciton Imaged by Tunneling Photocurrent Measurement

To experimentally probe the excitonic states we illuminated our t-WS_2 device with a 520nm continuous-wave laser focused on the tip-sample tunnel junction (as shown in Figure 6-1D). In order to overcome laser misalignment induced by STM thermal drift during the PTM measurement (usually lasting ~10 hours), a home-built auto laser alignment system with feedback control was developed. The laser spot position is detected with camera and corrected via a piezo-driven mirror every 20s. Photoexcited electrons and holes in t-WS_2 relax quickly (on the time scale of ps) to the lowest-energy moiré exciton state through phonon emission(*132-134*). Here we set the back gate voltage V_{BG} near 0 to keep the t-WS_2 undoped so as to avoid free carrier scattering that could decrease the exciton lifetime(*135*). The spatial charge distribution of the lowest-energy (long-lived) moiré exciton state was probed through STM tunneling photocurrent

measurement (electron tunneling processes occur on the time scale of ns). Figure 6-4A and Figure 6-4B show the absolute value of the tunnel current (I) as a function of V_{bias} measured at $B^{W/W}$ and AB stacking sites with (blue) and without (orange) laser illumination (the laser power for this measurement was P=600μW and the laser illumination area is around 80 μm^2). When the laser is off the tunnel current for both stacking sites shows a large semiconducting bandgap for -2V < V_{bias} < 1V. However, when the laser is turned on a photocurrent emerges even when V_{bias} lies in this gap region and the photocurrent response at the $B^{W/W}$ and AB sites show very different behavior.

To investigate the spatial dependence of the tunneling photocurrent, we performed 2D photocurrent mapping with V_{bias} = -0.6V and V_{BG} = 0 as shown in Figure 6-4C (laser power was held at P = 600uW). Surprisingly, the photocurrent changes sign at different locations even for fixed V_{bias}: positive photocurrent (red) appears at AB sites while negative photocurrent (blue) appears at $B^{W/W}$ sites. This spatially alternating photocurrent polarity provides direct experimental evidence for the emergence of in-plane charge transfer (ICT) moiré excitons.

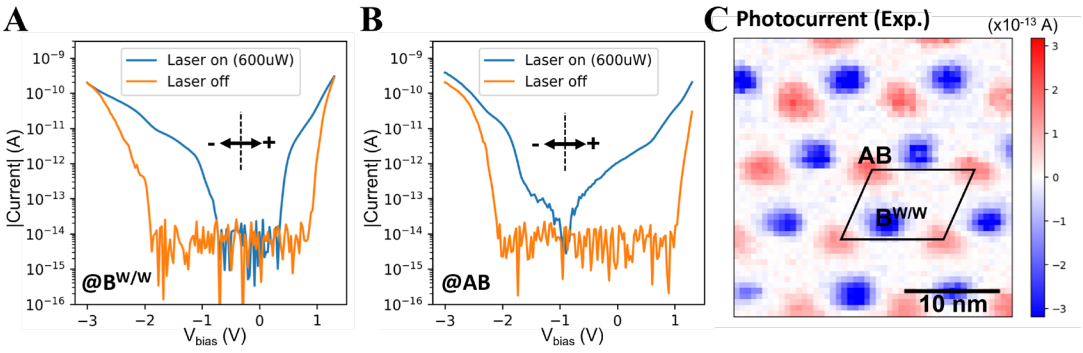

Figure 6-4 Tunneling Photocurrent measurement of t-WS_2. **A, B**. STM tunnel current spectra measured at the (**A**) $B^{W/W}$ and (**B**) AB stacking sites with the laser turned off (orange) and on (blue). V_{BG} = 0. The absolute value of the current is plotted on a logarithmic scale (the left and right branch of the spectra correspond to negative and positive current respectively). For the laser-off case, the current at both the $B^{W/W}$ and the AB sites reflect an energy gap for -2V <V_{bias} < 1V. For the laser-on case (P = 600uW) photocurrent emerges in the energy gap region and the $B^{W/W}$ and AB sites show different photocurrent spectral shapes. **C**. A photocurrent map of t-WS_2 measured with the laser on (P = 600uW) for V_{bias} = -0.60V and V_{BG} = 0 shows positive (negative) photocurrent at the AB ($B^{W/W}$) sites.

6.5 *Ab initio* Calculation of the Exciton States

To better interpret the photocurrent spatial distribution, we performed calculations of the excitonic states of t-WS_2 using the *ab initio GW*-BSE(*136, 137*). Here the exciton wavefunction χ_S is expressed as a linear combination of single-particle conduction (ck_m) and valence states (vk_m) in the moiré BZ: $\chi_S(r_e, r_h) = \sum_{cvk_m} A^S_{cvk_m} \psi^*_{vk_m}(r_h)\psi_{ck_m}(r_e)$ where S is the exciton principal quantum number, k_m is the electron wave vector in the

moiré BZ, $\mathrm{r_e}$and $\mathrm{r_h}$ are the electron and hole coordinates, respectively, v and c label a valence and conduction band, respectively, and $\mathrm{A}^{S}_{cv\mathrm{k}_m}$ are exciton electron-hole expansion coefficients. The exciton states can be calculated (including electron and hole degree of freedom) by state-of-the-art full-spinor *GW*-BSE calculations. However, due to the large number of atoms (~4000) in the t-WS_2 moiré unit cell, this calculation is computationally intractable. To overcome this bottleneck, we developed a new computational algorithm for calculating the electron-hole interaction kernel matrix elements. This involves extending the pristine unit-cell matrix projection (PUMP) method (developed previously for reconstructed monolayers(*115*)) to bilayer moiré superlattices. In the generalized pristine unit-cell matrix projection (PUMP) approach, we first express the twisted bilayer WS_2 moiré superlattice electronic wavefunctions as a linear combination of pristine wavefunctions of the individual layers. We denote the bottom pristine layer as 'a' and top layer as 'b'. The moiré valence and conduction states are constructed from the pristine wavefunctions,

$$|\psi^{\mathrm{cons}}_{\mathrm{v}\mathbf{k}_\mathrm{m}}\rangle = \sum_{i=1}^{n} (\mathrm{a}_i^{\mathrm{v}\mathbf{k}_\mathrm{m}} |\Phi^{\mathrm{val}}_{\mathrm{a},i\mathbf{k}_\mathrm{m}}\rangle + \mathrm{b}_i^{\mathrm{v}\mathbf{k}_m} |\Phi^{\mathrm{val}}_{\mathrm{b},i\mathbf{k}_\mathrm{m}}\rangle), \tag{6.1}$$

$$|\psi^{\mathrm{cons}}_{\mathrm{c}\mathbf{k}_\mathrm{m}}\rangle = \sum_{i=1}^{n} (\mathrm{a}_i^{\mathrm{c}\mathbf{k}_\mathrm{m}} |\Phi^{\mathrm{cond}}_{\mathrm{a},i\mathbf{k}_\mathrm{m}}\rangle + \mathrm{b}_i^{\mathrm{c}\mathbf{k}_m} |\Phi^{\mathrm{cond}}_{\mathrm{b},i\mathbf{k}_\mathrm{m}}\rangle). \tag{6.2}$$

Here, $|\Phi^{\mathrm{val}}_{\mathrm{a},i\mathbf{k}_\mathrm{m}}\rangle$ and $|\Phi^{\mathrm{val}}_{\mathrm{b},i\mathbf{k}_\mathrm{m}}\rangle$ refers to pristine superlattice valence states of layer 'a' and layer 'b', respectively, and $|\Phi^{\mathrm{cond}}_{\mathrm{a},i\mathbf{k}_\mathrm{m}}\rangle$ and $|\Phi^{\mathrm{cond}}_{\mathrm{b},i\mathbf{k}_\mathrm{m}}\rangle$ to pristine superlattice conduction states of layer 'a' and layer 'b', respectively. We have verified that the new basis sufficiently describes the original moiré electronic wavefunctions ($|\psi_{\mathrm{v}\mathbf{k}_\mathrm{m}}\rangle$ and $|\psi_{\mathrm{c}\mathbf{k}_\mathrm{m}}\rangle$) by computing the overlaps $\langle\psi^{\mathrm{cons}}_{\mathrm{v}\mathbf{k}_\mathrm{m}}|\psi_{\mathrm{v}\mathbf{k}_\mathrm{m}}\rangle$ and $\langle\psi^{\mathrm{cons}}_{\mathrm{c}\mathbf{k}_\mathrm{m}}|\psi_{\mathrm{c}\mathbf{k}_\mathrm{m}}\rangle$ (see Figure 6-5). Using the expansion coefficients, the BSE electron-hole interaction kernel matrix elements of the moiré superlattice can be approximated as a linear combination of pristine unit-cell kernel matrix elements of layer 'a' and layer 'b',

$$\langle\psi_{\mathrm{v}\mathbf{k}_\mathrm{m}}\psi_{\mathrm{c}\mathbf{k}_\mathrm{m}}|\mathrm{K}|\psi_{\mathrm{v}\mathbf{k}'_\mathrm{m}}\psi_{\mathrm{c}\mathbf{k}'_\mathrm{m}}\rangle$$

$$\approx \sum_{\alpha\beta\gamma\lambda=\mathrm{a,b}} \sum_{ijpq} \alpha_i^{\mathrm{v}\mathbf{k}_\mathrm{m}*} \beta_j^{\mathrm{c}\mathbf{k}_\mathrm{m}*} \gamma_p^{\mathrm{v}\mathbf{k}_\mathrm{m}} \lambda_q^{\mathrm{c}\mathbf{k}_\mathrm{m}} \langle\Phi^{\mathrm{val}}_{\alpha,i\mathbf{k}_\mathrm{m}} \Phi^{\mathrm{cond}}_{\beta,j\mathbf{k}_\mathrm{m}} | \mathrm{K} | \Phi^{\mathrm{val}}_{\gamma,p\mathbf{k}'_\mathrm{m}} \Phi^{\mathrm{cond}}_{\lambda,q\mathbf{k}'_\mathrm{m}}\rangle \tag{6.3}$$

$$= \sum_{\alpha\beta\gamma\lambda=\mathrm{a,b}} \sum_{ijpq} \alpha_i^{\mathrm{v}\mathbf{k}_\mathrm{m}*} \beta_j^{\mathrm{c}\mathbf{k}_\mathrm{m}*} \gamma_p^{\mathrm{v}\mathbf{k}_\mathrm{m}} \lambda_q^{\mathrm{c}\mathbf{k}_\mathrm{m}} \langle\phi^{\mathrm{val}}_{\alpha,s\mathbf{k}^1_{\mathrm{uc}}} \phi^{\mathrm{cond}}_{\beta,t\mathbf{k}^2_{\mathrm{uc}}} | \mathrm{K} | \phi^{\mathrm{val}}_{\gamma,y\mathbf{k}^3_{\mathrm{uc}}} \phi^{\mathrm{cond}}_{\lambda,z\mathbf{k}^4_{\mathrm{uc}}}\rangle, \tag{6.4}$$

where α, β, γ and λ are layer indices, i and p are pristine valence band indices, j and q are pristine conduction band indices. The pristine states $i\mathbf{k}_\mathrm{m}, j\mathbf{k}_\mathrm{m}, p\mathbf{k}'_\mathrm{m}$ and $q\mathbf{k}'_\mathrm{m}$ in the moiré BZ are related to $s\mathbf{k}^1_{\mathrm{uc}}, t\mathbf{k}^2_{\mathrm{uc}}, y\mathbf{k}^3_{\mathrm{uc}}$ and $z\mathbf{k}^4_{\mathrm{uc}}$ in the unit-cell BZ by band folding. The kernel matrix element is in Eq. S3 refers to the pristine supercell matrix element, while the matrix element in Eq. S4 refers to the pristine unit-cell matrix element. The screened Coulomb interaction used in Eq. S4 is that of pristine AB or 2H stacking. Thus,

we can express each moiré kernel matrix element as a linear combination of pristine unit-cell kernel matrix elements.

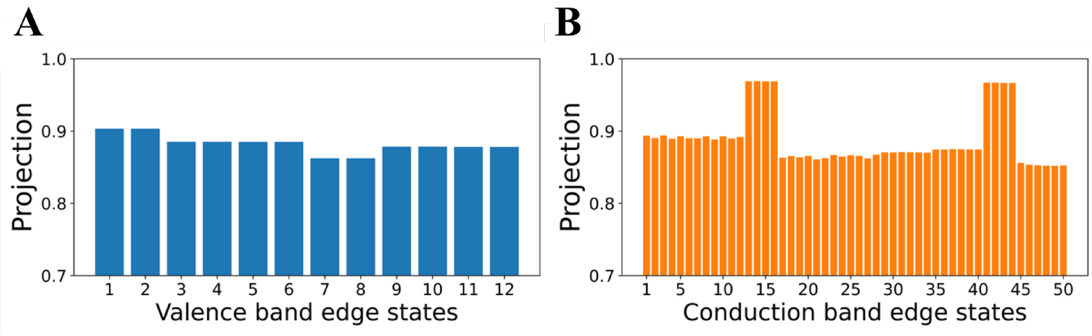

Figure 6-5 Projection of the constructed wavefunctions on the original wavefunctions. Projection of the constructed 57.72° twisted bilayer WS_2 moiré superlattice valence ($\langle\psi^{\mathrm{cons}}_{\mathrm{v}\mathbf{k}_\mathrm{m}}|\psi_{\mathrm{v}\mathbf{k}_\mathrm{m}}\rangle$) (**A**) and conduction ($\langle\psi^{\mathrm{cons}}_{\mathrm{c}\mathbf{k}_\mathrm{m}}|\psi_{\mathrm{c}\mathbf{k}_\mathrm{m}}\rangle$) (**B**) electronic states on the original electronic states at the γ point in the moiré BZ, respectively. The moiré electronic states are constructed using a basis of 200 valence and 200 conductions states of each pristine layer ($n = 200$ in Eq. S1). The average projection is 89%. The conduction states derived from the *K* point in the pristine unit-cell BZ, which have less interlayer hybridization, have a higher projection compared to the states derived from the *Q* point.

The BSE kernel(*138*) is given by $\mathrm{K} = -\mathrm{K_d} + \mathrm{K_x}$, where $\mathrm{K_d}$ is a direct matrix element responsible for the attractive electron-hole interaction, and $\mathrm{K_x}$ is a repulsive exchange interaction. The kernel matrix elements are six-dimensional integrals,

$$\left\langle \Phi^{\mathrm{val}}_{\alpha,\mathrm{i}\mathbf{k}_\mathrm{m}} \Phi^{\mathrm{cond}}_{\beta,\mathrm{j}\mathbf{k}_\mathrm{m}} \middle| \mathrm{K^d} \middle| \Phi^{\mathrm{val}}_{\gamma,\mathrm{p}\mathbf{k}'_\mathrm{m}} \Phi^{\mathrm{cond}}_{\lambda,\mathrm{q}\mathbf{k}'_\mathrm{m}} \right\rangle \tag{6.5}$$

$$= \int \mathrm{d}\mathbf{r}\mathrm{d}\mathbf{r}' \Phi^{\mathrm{cond}*}_{\beta,\mathrm{j}\mathbf{k}_\mathrm{m}}(\mathbf{r}) \Phi^{\mathrm{cond}}_{\lambda,\mathrm{q}\mathbf{k}'_\mathrm{m}}(\mathbf{r}) \mathrm{W^{AB}}(\mathbf{r},\mathbf{r}') \Phi^{\mathrm{val}}_{\alpha,\mathrm{i}\mathbf{k}_\mathrm{m}}(\mathbf{r}') \Phi^{\mathrm{val}*}_{\gamma,\mathrm{p}\mathbf{k}'_\mathrm{m}}(\mathbf{r}'), \tag{6.6}$$

$$\left\langle \Phi^{\mathrm{val}}_{\alpha,\mathrm{i}\mathbf{k}_\mathrm{m}} \Phi^{\mathrm{cond}}_{\beta,\mathrm{j}\mathbf{k}_\mathrm{m}} | \mathrm{K^x} | \Phi^{\mathrm{val}}_{\gamma,\mathrm{p}\mathbf{k}'_\mathrm{m}} \Phi^{\mathrm{cond}}_{\lambda,\mathrm{q}\mathbf{k}'_\mathrm{m}} \right\rangle \tag{6.7}$$

$$= \int \mathrm{d}\mathbf{r}\mathrm{d}\mathbf{r}' \Phi^{\mathrm{cond}*}_{\beta,\mathrm{j}\mathbf{k}_\mathrm{m}}(\mathbf{r}) \Phi^{\mathrm{val}}_{\alpha,\mathrm{i}\mathbf{k}_\mathrm{m}}(\mathbf{r}) \mathrm{W^{AB}}(\mathbf{r},\mathbf{r}') \Phi^{\mathrm{cond}}_{\lambda,\mathrm{q}\mathbf{k}'_\mathrm{m}}(\mathbf{r}') \Phi^{\mathrm{val}*}_{\gamma,\mathrm{p}\mathbf{k}'_\mathrm{m}}(\mathbf{r}'). \tag{6.8}$$

The pristine kernel matrix elements that we need to compute can be classified in terms of the layer indices, α, β, γ and λ.

When all the indices refer to layer ‘a’ or layer ‘b’, the kernel matrix element is an intralayer kernel matrix element of layer ‘a’ or layer ‘b’, respectively, with a pristine AB stacking screened Coulomb interaction. For the intralayer kernel matrix elements of layer ‘a’, we choose the screened Coulomb interaction with the periodicity of the layer ‘a’, i.e., $W^{\mathrm{AB}}_{\mathbf{q}}(\mathbf{G}_\mathrm{a}, \mathbf{G}'_\mathrm{a})$ where $\mathbf{G}_\mathrm{a}$ and $\mathbf{G}'_\mathrm{a}$ are reciprocal lattice vectors of layer ‘a’. Similarly, for the intralayer kernel matrix elements of layer ‘b’ we choose the screened Coulomb interaction with layer ‘b’ periodicity: $W^{\mathrm{AB}}_{\mathbf{q}}(\mathbf{G}_\mathrm{b}, \mathbf{G}'_\mathrm{b})$. The choice of W has important

implications for the Umklapp processes involved. For the intralayer kernel matrix elements of layer 'a', only terms with $\mathbf{k}^2_{\mathrm{uc}} - \mathbf{k}^1_{\mathrm{uc}} = \mathbf{k}^4_{\mathrm{uc}} - \mathbf{k}^3_{\mathrm{uc}} + \mathbf{G}_{\mathrm{a}}$ are non-zero,

$$\left\langle \Phi^{\mathrm{val}}_{\mathrm{a},i\mathbf{k}_{\mathrm{m}}} \Phi^{\mathrm{cond}}_{\mathrm{a},j\mathbf{k}_{\mathrm{m}}} | \mathrm{K} | \Phi^{\mathrm{val}}_{\mathrm{a},p\mathbf{k}'_{\mathrm{m}}} \Phi^{\mathrm{cond}}_{\mathrm{a},q\mathbf{k}'_{\mathrm{m}}} \right\rangle \tag{6.9}$$

$$= \left\langle \phi^{\mathrm{val}}_{\alpha,s\mathbf{k}^1_{\mathrm{uc}}} \phi^{\mathrm{cond}}_{\beta,t\mathbf{k}^2_{\mathrm{uc}}} | \mathrm{K} | \phi^{\mathrm{val}}_{\gamma,y\mathbf{k}^3_{\mathrm{uc}}} \phi^{\mathrm{cond}}_{\lambda,z\mathbf{k}^4_{\mathrm{uc}}} \right\rangle \delta_{\mathbf{k}^2_{\mathrm{uc}} - \mathbf{k}^1_{\mathrm{uc}}, \mathbf{k}^4_{\mathrm{uc}} - \mathbf{k}^3_{\mathrm{uc}} + \boldsymbol{G}_a} \tag{6.10}$$

The other combinations of α, β, γ and λ refer to interlayer kernel matrix elements. Since layer 'a' and layer 'b' are separated by about 3 Å, and the wavefunctions of each layer exponentially decay in vacuum, we only compute the dominant interlayer interactions for the direct and exchange matrix elements. From Eq. (6.5), we find that the interlayer interaction is non-negligible for the direct kernel matrix element only when $\alpha = \gamma$ and $\beta = \lambda$. For example, the contribution of $\Phi^{\mathrm{cond}*}_{\beta,j\mathbf{k}_{\mathrm{m}}}(\mathbf{r})\Phi^{\mathrm{cond}}_{\lambda,q\mathbf{k}'_{\mathrm{m}}}(\mathbf{r})$ is small to the integral in Eq. (6.5) when the two conduction states are in different layers. Similarly, the interlayer interaction is non-negligible for the exchange kernel matrix element when $\alpha = \beta$ and $\gamma = \lambda$ (from Eq. (6.6)). For the interlayer direct kernel interactions, we approximate the screened Coulomb interaction to have the periodicity of layer 'a' and we further include only long-range interactions in the in-plane direction ($\mathrm{G_x} = \mathrm{G'_x} = 0$ and $\mathrm{G_y} = \mathrm{G'_y} = 0$), while fully including local-field effects in the out-of-plane direction:

$$\mathrm{W}_{\mathbf{q}}(\mathbf{G}, \mathbf{G}') \approx \mathrm{W}_{\mathbf{q}}(\mathbf{G}, \mathbf{G}') \delta_{\mathrm{G_x}, \mathrm{G'_x}=0} \delta_{\mathrm{G_y}, \mathrm{G'_y}=0}, \tag{6.11}$$

where $\mathbf{G}$ is a reciprocal lattice vector. This approximation is valid for the interlayer matrix elements since the hole and electron are in different layers, hence the in-plane local-field effect and short-wavelength modulations of W are not as important as the long-wavelength interactions.

This generalized PUMP method allows us to calculate moiré exciton energies and wavefunctions for the t-WS_2 moiré superlattice. We study the $\mathrm{Q} = 0$ exciton in the moiré BZ, where Q is the exciton center-of-mass wave vector. While these states are formed by coherent superposition of direct transitions in the moiré BZ, the valence-band and conduction-band states involved originate from different valleys in the unfolded unit-cell BZ and are strongly modified by the moiré potential.

Figure 6-6A shows the calculated electron density distribution for the lowest-energy exciton wavefunction $\chi_0(r_e, r_h)$ with a fixed hole position r_h (labeled with a red solid dot) at the AB site (left panel), the $\mathrm{B^{W/W}}$ site (middle panel), and the $\mathrm{B^{S/S}}$ site (right panel). The electron density is maximum at the $\mathrm{B^{W/W}}$ site when the hole is at the AB site and is vanishingly small when the hole is at the $\mathrm{B^{W/W}}$ and $\mathrm{B^{S/S}}$ sites. The spin-aligned and spin-antialigned excitons have the same energy due to spatial separation of photoexcited electron and hole, which results in a small exchange energy. In the out-of-plane direction, the electron and hole charge densities are delocalized over both layers and show no interlayer charge transfer. This demonstrates that the lowest-energy exciton state in t-WS_2 is a layer-hybridized in-plane charge-transfer (ICT) exciton, in which the electron and hole prefer the $\mathrm{B^{W/W}}$ site and AB site, respectively. The calculated binding energy for the ICT exciton, when the bilayer is suspended in vacuum, is ~150 meV. In presence of the

hBN substrate, we expect the binding energy to be smaller due to additional dielectric screening.

ICT moiré excitons can be expected to yield a STM tip-position dependent photocurrent polarity due to their intrinsic lateral electron-hole separation. As illustrated in Figure 6-6B, when the STM tip is parked above the photoexcited electron of an ICT exciton (left panel) the tunneling probability for the electron dominates compared to the spatially displaced photoexcited hole, thus resulting in negative tunneling current. Similarly, positive tunnel current is expected when the tip is parked above the photoexcited hole (right panel). Our photocurrent measurement thus directly reflects the charge density distribution of the lowest-energy ICT moiré exciton which can be expressed in unit of proton charge as $\rho(r) = \rho_h(r) - \rho_e(r)$, where $\rho_e(r) = \int |\chi_0(r_e, r_h)|^2 dr_h$ and $\rho_h(r) = \int |\chi_0(r_e, r_h)|^2 dr_e$ are the electron and hole densities, respectively. The calculated distribution map for $\rho(r)$ is shown in Figure 6-6C. The laterally separated electrons and holes of the ICT excitons yield an alternating charge polarity that nicely matches our photocurrent map (Figure 6-6C), providing quantitative spatial evidence that we are imaging ICT moiré excitons.

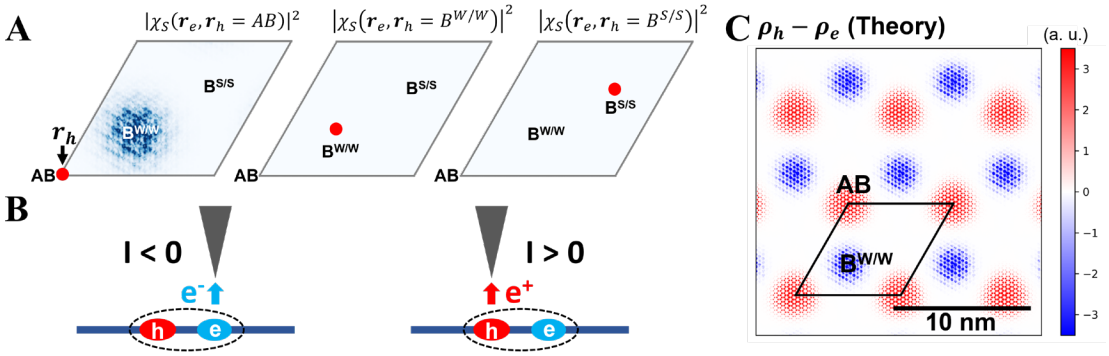

Figure 6-6 Theoretical calculation for the lowest-energy exciton state. **A**. Calculated electron density for the lowest-energy exciton, $|\chi_0(r_e, r_h)|^2$, with fixed hole position r_h (labeled with red solid dot) at the AB site (left panel), the $B^{W/W}$ site (middle panel), and the $B^{S/S}$ site (right panel). The maps show appreciable electron density at the $B^{W/W}$ site only when the hole position is fixed at the AB site (left panel). **B**. Schematic for tip-position dependent tunnel current from an ICT exciton. When the STM tip sits above the electron (left panel) the larger tunnel probability for the electron yields a negative current. A positive current is detected when the tip sits above the hole (right panel). **C**. Calculated charge distribution map $\rho(r) = \rho_h(r) - \rho_e(r)$ of the ICT exciton, where $\rho_h(r) = \int |\chi_0(r_e, r_h)|^2 dr_e$ and $\rho_e(r) = \int |\chi_0(r_e, r_h)|^2 dr_h$.

6.6 Tip-induced Exciton Dissociation

We can further explore the interaction between the STM tip and ICT moiré excitons by investigating the V_{bias} dependence of the photocurrent. Figure 6-7A shows the photocurrent as a function of V_{bias} measured at the AB (red, hole dominant) and $B^{W/W}$ (blue, electron dominant) sites. It shows a ~200mV tip bias range (marked by dashed lines) where positive photocurrent (at AB sites) and negative photocurrent (at $B^{W/W}$ sites)

coexist. To observe the tip's effect on the photocurrent we measured photocurrent maps for -985mV ≤ V_{bias} ≤ -602mV using the same tip (Figure 6-7B-F). These maps also show a ~200mV range of V_{bias} values where positive and negative photocurrent coexist, consistent with Figure 6-7A (this V_{bias} range varies depending on the tip sharpness but always lies between 100mV and 250mV.

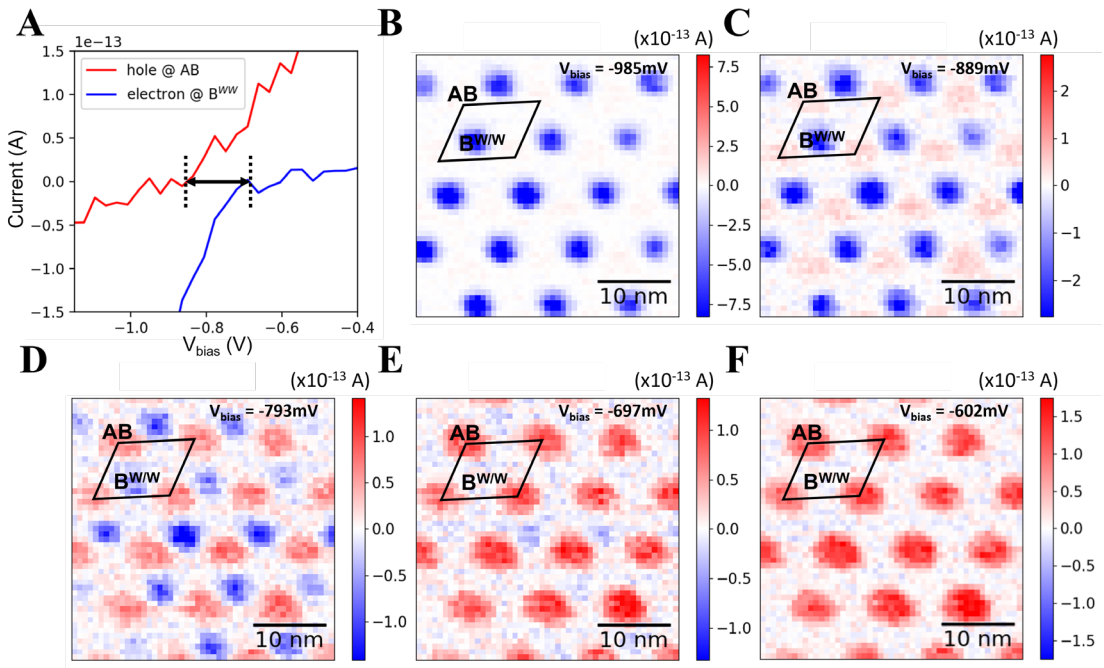

Figure 6-7 V_{bias} dependent photocurrent mapping. **A**. Zoom-in photocurrent spectra at the AB (hole) site (red) and the $B^{W/W}$ (electron) site (blue). Spatially alternating current polarity occurs for a V_{bias} range of ~200mV (dashed line). **B-F**. Evolution of t-WS_2 photocurrent maps for increasing V_{bias}: (**B**) V_{bias} = -985mV, (**C**) V_{bias} = -889mV, (**D**) V_{bias} = -793mV, (**E**) V_{bias} = -697mV, and (**F**) V_{bias} = -602mV. Spatially alternating current polarity exists only in (**C-E**), while negative (positive) current dominates in **B** (**F**).

The V_{bias} dependence of the photocurrent reflects a tip-induced exciton dissociation effect, as illustrated in Figure 6-8A-C for different V_{bias} values. Because of capacitive coupling between the backgate graphite and the STM tip, a potential difference between them induces an electric field near the tip apex that perturbs the ICT moiré excitons (the t-WS_2 chemical potential lies within an energy gap at V_{BG} = 0 and so does not screen the electric field). The work function difference between the tip (made of Pt/Ir) and the graphite back gate causes that this field to be present even at V_{bias} = 0, but it can be cancelled by setting $V_{bias} = V_0$ where V_0 is the work function difference. At $V_{bias} - V_0 = 0$ (Figure 6-8A) the tip exerts only a weak pertubation on the ICT excitons and so a spatially alternating photocurrent polarity can be observed (Figure 6-4C and (Figure 6-7C-E). However, at $V_{bias} - V_0 > 0$ the tip apex accumulates negative charge and attracts holes while repelling electrons (Figure 6-8B). Above a certain threshold this effect dissociates the ICT excitons and only a positive current can be observed as in Figure 6-8B. Similarly, only a negative current is seen when $V_{bias} - V_0$ is much smaller

than zero (Figure 6-7B) due to opposite dissociation of the ICT excitons, as illustrated in Figure 6-8C. The experimentally observed V_0 ranges from -800mV to -300mV depending on the tip structure (V_0 = -790mV for the measurements shown in Figure 6-7).

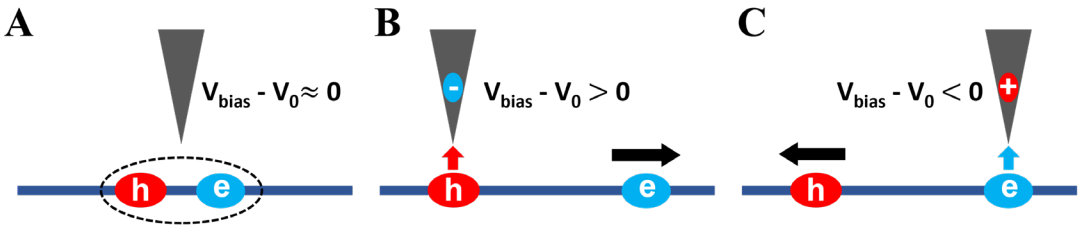

Figure 6-8 Diagram of tip-induced ICT exciton dissociation effect. V_0 is the bias voltage offset that compensates the work function difference between the tip and the back gate graphite. **A**. For $V_{bias} - V_0 \approx 0$ the tip does not significantly perturb the ICT exciton and so both photocurrent polarities are seen. **B**. For $V_{bias} - V_0 > 0$ negative charge accumulates at the tip apex which attracts holes and repels electrons, thereby dissociating ICT excitons. **C**. For $V_{bias} - V_0 < 0$ the tip attracts electrons and repels holes, thereby dissociating ICT excitons.

We note that if only the Pauli exclusion principle is considered while the tip induced Coulomb interaction is neglected, a much wider V_{bias} range for coexisting positive and negative photocurrent polarities should be expected. Figure 6-9A (I-III) illustrates the band diagram for the ideal tunneling of ICT moiré excitons for different V_{bias} conditions controlling the difference between the chemical potentials of the t-WS_2 (μ_{tWS_2}) and the tip (μ_{tip}). When μ_{tip} is within the bandgap of the t-WS_2 (regime I), both the electron and hole of the ICT exciton can tunnel into the STM tip (with probabilities depending on the tip position). When V_{bias} is more negative such that μ_{tip} is below the energy of the exciton's hole (labeled with a red peak) (regime II), the tunneling of the hole is forbidden due to the Pauli exclusion principle. Similarly, the tunneling of the electron into the tip is forbidden when μ_{tip} is above the energy of the exciton's electron (regime III). Figure 6-9B illustrates the ideal tunnel photocurrent as a function of V_{bias} at $B^{W/W}$ sites and AB sites where electrons and holes localize, respectively. Negative tunnel current due to electron tunneling exists when $eV_{bias} > -(E_g - E_b)$ while positive tunnel current due to hole tunneling exists when $eV_{bias} < (E_g - E_b)$, where E_g (~1.3eV) and E_b (~20meV) are the band gap and ICT exciton binding energy, respectively.

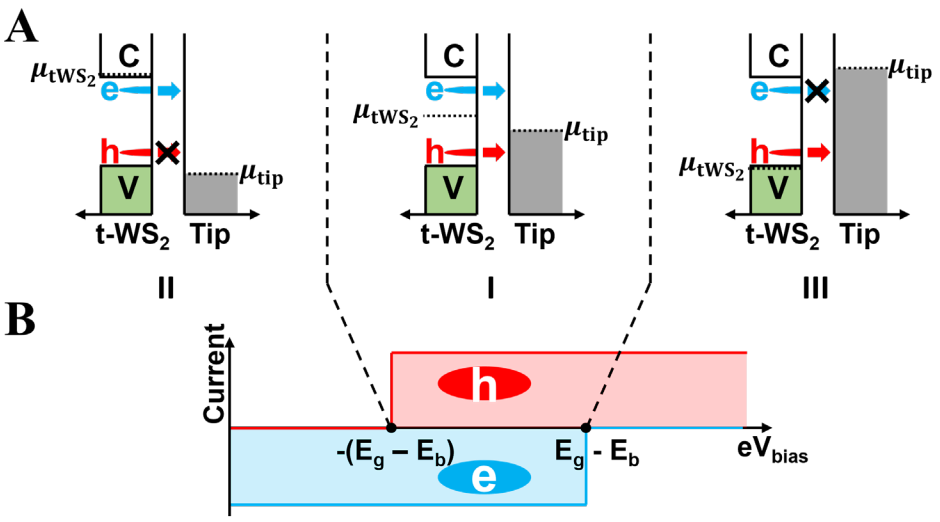

Figure 6-9 Ideal tunneling of ICT exciton without STM tip perturbation for different V_{bias} conditions. See full discussion in Section 6.6.

6.7 Summary and Outlook

In conclusion, our photocurrent tunneling microscopy enables real-space imaging of in-plane charge-transfer moiré excitons with sub-nanometer spatial resolution. The observed electron and hole distributions agree well with *ab initio GW*-BSE calculation results. This work establishes a new approach for probing the microscopic behavior of photoexcited states in 2D van der Waals heterostructures.

References

1. K. S. Novoselov *et al.*, Electric field effect in atomically thin carbon films. *science* **306**, 666-669 (2004).
2. A. C. Neto, F. Guinea, N. M. Peres, K. S. Novoselov, A. K. Geim, The electronic properties of graphene. *Reviews of modern physics* **81**, 109 (2009).
3. , (!!! INVALID CITATION !!! {}).
4. G. Cassabois, P. Valvin, B. Gil, Hexagonal boron nitride is an indirect bandgap semiconductor. *Nature photonics* **10**, 262-266 (2016).
5. S. Manzeli, D. Ovchinnikov, D. Pasquier, O. V. Yazyev, A. Kis, 2D transition metal dichalcogenides. *Nature Reviews Materials* **2**, 1-15 (2017).
6. A. Splendiani *et al.*, Emerging photoluminescence in monolayer MoS2. *Nano letters* **10**, 1271-1275 (2010).
7. K. F. Mak, C. Lee, J. Hone, J. Shan, T. F. Heinz, Atomically thin MoS 2: a new direct-gap semiconductor. *Physical review letters* **105**, 136805 (2010).
8. D. Xiao, G.-B. Liu, W. Feng, X. Xu, W. Yao, Coupled spin and valley physics in monolayers of MoS 2 and other group-VI dichalcogenides. *Physical review letters* **108**, 196802 (2012).
9. A. Chernikov *et al.*, Exciton binding energy and nonhydrogenic Rydberg series in monolayer WS 2. *Physical review letters* **113**, 076802 (2014).
10. B. Radisavljevic, A. Radenovic, J. Brivio, V. Giacometti, A. Kis, Single-layer MoS2 transistors. *Nature nanotechnology* **6**, 147-150 (2011).
11. A. K. Geim, I. V. Grigorieva, Van der Waals heterostructures. *Nature* **499**, 419-425 (2013).
12. L. Wang *et al.*, One-dimensional electrical contact to a two-dimensional material. *Science* **342**, 614-617 (2013).
13. X. Hong *et al.*, Ultrafast charge transfer in atomically thin MoS2/WS2 heterostructures. *Nature nanotechnology* **9**, 682-686 (2014).
14. K. F. Mak, J. Shan, Opportunities and challenges of interlayer exciton control and manipulation. *Nature nanotechnology* **13**, 974-976 (2018).
15. T. Li *et al.*, Quantum anomalous Hall effect from intertwined moiré bands. *Nature* **600**, 641-646 (2021).
16. Y. Cao *et al.*, Correlated insulator behaviour at half-filling in magic-angle graphene superlattices. *Nature* **556**, 80-84 (2018).
17. X. Liu *et al.*, Spin-polarized correlated insulator and superconductor in twisted double bilayer graphene. *arXiv preprint arXiv:1903.08130*, (2019).
18. L. Wang *et al.*, Correlated electronic phases in twisted bilayer transition metal dichalcogenides. *Nat Mater* **19**, 861-866 (2020).
19. Y. Cao *et al.*, Unconventional superconductivity in magic-angle graphene superlattices. *Nature* **556**, 43-50 (2018).
20. M. Yankowitz *et al.*, Tuning superconductivity in twisted bilayer graphene. *Science* **363**, 1059-1064 (2019).
21. G. Chen *et al.*, Signatures of tunable superconductivity in a trilayer graphene moiré superlattice. *Nature* **572**, 215-219 (2019).
22. H. Kim *et al.*, Evidence for unconventional superconductivity in twisted trilayer graphene. *Nature* **606**, 494-500 (2022).
23. M. Oh *et al.*, Evidence for unconventional superconductivity in twisted bilayer graphene. *Nature* **600**, 240-245 (2021).

24. G. Chen *et al.*, Tunable correlated chern insulator and ferromagnetism in a moiré superlattice. *Nature* **579**, 56-61 (2020).
25. A. T. Pierce *et al.*, Unconventional sequence of correlated Chern insulators in magic-angle twisted bilayer graphene. *arXiv preprint arXiv:2101.04123*, (2021).
26. Y. Xie *et al.*, Fractional Chern insulators in magic-angle twisted bilayer graphene. *arXiv preprint arXiv:2107.10854*, (2021).
27. A. L. Sharpe *et al.*, Emergent ferromagnetism near three-quarters filling in twisted bilayer graphene. *Science* **365**, 605-608 (2019).
28. H.-P. Eckle, *Models of Quantum Matter: A First Course on Integrability and the Bethe Ansatz*. (Oxford University Press, 2019).
29. E. H. Lieb, F.-Y. Wu, Absence of Mott transition in an exact solution of the short-range, one-band model in one dimension. *Physical Review Letters* **20**, 1445 (1968).
30. S. A. Hartnoll, Theory of universal incoherent metallic transport. *Nature Physics* **11**, 54-61 (2015).
31. D. P. Arovas, E. Berg, S. A. Kivelson, S. Raghu, The hubbard model. *Annual review of condensed matter physics* **13**, 239-274 (2022).
32. S. Y. Kim *et al.*, Spectroscopic studies on the metal–insulator transition mechanism in correlated materials. *Advanced Materials* **30**, 1704777 (2018).
33. J. Hubbard, Generalized Wigner lattices in one dimension and some applications to tetracyanoquinodimethane (TCNQ) salts. *Physical Review B* **17**, 494 (1978).
34. M. F. Crommie, C. P. Lutz, D. M. Eigler, Confinement of electrons to quantum corrals on a metal surface. *Science* **262**, 218-220 (1993).
35. Ø. Fischer, M. Kugler, I. Maggio-Aprile, C. Berthod, C. Renner, Scanning tunneling spectroscopy of high-temperature superconductors. *Reviews of Modern Physics* **79**, 353 (2007).
36. G. Binnig, H. Rohrer, Scanning tunneling microscopy—from birth to adolescence. *reviews of modern physics* **59**, 615 (1987).
37. J. Tersoff, D. R. Hamann, Theory of the scanning tunneling microscope. *Physical Review B* **31**, 805 (1985).
38. J. Bardeen, Tunnelling from a many-particle point of view. *Physical review letters* **6**, 57 (1961).
39. N. A. Pradhan, N. Liu, C. Silien, W. Ho, Atomic scale conductance induced by single impurity charging. *Physical review letters* **94**, 076801 (2005).
40. R. Decker *et al.*, Local electronic properties of graphene on a BN substrate via scanning tunneling microscopy. *Nano letters* **11**, 2291-2295 (2011).
41. X. Lu *et al.*, Superconductors, orbital magnets and correlated states in magic-angle bilayer graphene. *Nature* **574**, 653-657 (2019).
42. U. Zondiner *et al.*, Cascade of phase transitions and Dirac revivals in magic-angle graphene. *Nature* **582**, 203-208 (2020).
43. X. Liu *et al.*, Tunable spin-polarized correlated states in twisted double bilayer graphene. *Nature* **583**, 221-225 (2020).
44. G. W. Burg *et al.*, Correlated insulating states in twisted double bilayer graphene. *Physical Review Letters* **123**, 197702 (2019).
45. Y. Cao *et al.*, Tunable correlated states and spin-polarized phases in twisted bilayer–bilayer graphene. *Nature* **583**, 215–220 (2020).
46. G. Chen *et al.*, Evidence of a gate-tunable Mott insulator in a trilayer graphene moiré superlattice. *Nature Physics* **15**, 237-241 (2019).
47. Y. Tang *et al.*, Simulation of Hubbard model physics in WSe 2/WS 2 moiré superlattices. *Nature* **579**, 353-358 (2020).
48. E. C. Regan *et al.*, Mott and generalized Wigner crystal states in WSe 2/WS 2 moiré superlattices. *Nature* **579**, 359-363 (2020).

49. L. Wang *et al.*, Correlated electronic phases in twisted bilayer transition metal dichalcogenides. *Nature materials*, 1-6 (2020).
50. F. Wu, T. Lovorn, E. Tutuc, A. H. MacDonald, Hubbard model physics in transition metal dichalcogenide moiré bands. *Physical review letters* **121**, 026402 (2018).
51. Y. Shimazaki *et al.*, Strongly correlated electrons and hybrid excitons in a moiré heterostructure. *Nature* **580**, 472-477 (2020).
52. K. Slagle, L. Fu, Charge Transfer Excitations, Pair Density Waves, and Superconductivity in Moir\'e Materials. *arXiv preprint arXiv:2003.13690*, (2020).
53. Y. Zhang, N. F. Yuan, L. Fu, Moiré quantum chemistry: charge transfer in transition metal dichalcogenide superlattices. *Physical Review B* **102**, 201115 (2020).
54. A. Kerelsky *et al.*, Maximized electron interactions at the magic angle in twisted bilayer graphene. *Nature* **572**, 95-100 (2019).
55. Y. Xie *et al.*, Spectroscopic signatures of many-body correlations in magic-angle twisted bilayer graphene. *Nature* **572**, 101-105 (2019).
56. Y. Jiang *et al.*, Charge order and broken rotational symmetry in magic-angle twisted bilayer graphene. *Nature* **573**, 91-95 (2019).
57. Y. Choi *et al.*, Electronic correlations in twisted bilayer graphene near the magic angle. *Nature Physics* **15**, 1174-1180 (2019).
58. Y. Pan *et al.*, Quantum-confined electronic states arising from the moiré pattern of MoS2–WSe2 heterobilayers. *Nano letters* **18**, 1849-1855 (2018).
59. C. Zhang *et al.*, Interlayer couplings, Moiré patterns, and 2D electronic superlattices in MoS2/WSe2 hetero-bilayers. *Science advances* **3**, e1601459 (2017).
60. Z. Zhang *et al.*, Flat bands in twisted bilayer transition metal dichalcogenides. *Nature Physics* **16**, 1093-1096 (2020).
61. A. Raja *et al.*, Coulomb engineering of the bandgap and excitons in two-dimensional materials. *Nature communications* **8**, 1-7 (2017).
62. G. Wang *et al.*, Colloquium: Excitons in atomically thin transition metal dichalcogenides. *Reviews of Modern Physics* **90**, 021001 (2018).
63. M. M. Ugeda *et al.*, Giant bandgap renormalization and excitonic effects in a monolayer transition metal dichalcogenide semiconductor. *Nature materials* **13**, 1091-1095 (2014).
64. H. Li *et al.*, Imaging moiré flat bands in three-dimensional reconstructed WSe 2/WS 2 superlattices. *Nature Materials* **20**, 945–950 (2021).
65. Y. Liu *et al.*, Toward barrier free contact to molybdenum disulfide using graphene electrodes. *Nano letters* **15**, 3030-3034 (2015).
66. H. Li *et al.*, Electrode-Free Anodic Oxidation Nanolithography of Low-Dimensional Materials. *Nano letters* **18**, 8011-8015 (2018).
67. D. Waters *et al.*, Flat Bands and Mechanical Deformation Effects in the Moiré Superlattice of MoS2-WSe2 Heterobilayers. *ACS Nano*, (2020).
68. K. Slagle, L. Fu, Charge transfer excitations, pair density waves, and superconductivity in moiré materials. *Physical Review B* **102**, 235423 (2020).
69. M. H. Naik, M. Jain, Origin of layer dependence in band structures of two-dimensional materials. *Physical Review B* **95**, 165125 (2017).
70. A. J. Bradley *et al.*, Probing the role of interlayer coupling and coulomb interactions on electronic structure in few-layer MoSe2 nanostructures. *Nano letters* **15**, 2594-2599 (2015).
71. M. H. Naik, M. Jain, Ultraflatbands and shear solitons in moiré patterns of twisted bilayer transition metal dichalcogenides. *Physical review letters* **121**, 266401 (2018).
72. M. H. Naik, S. Kundu, I. Maity, M. Jain, Origin and Evolution of Ultraflatbands in Twisted Bilayer Transition Metal Dichalcogenides: Realization of Triangular Quantum Dots. *arXiv preprint arXiv:1908.10399*, (2019).

73. C. Jin *et al.*, Stripe phases in WSe 2/WS 2 moiré superlattices. *Nature Materials*, 1-5 (2021).
74. Y. Xu *et al.*, Correlated insulating states at fractional fillings of moiré superlattices. *Nature* **587**, 214-218 (2020).
75. X. Huang *et al.*, Correlated insulating states at fractional fillings of the WS2/WSe2 moiré lattice. *Nature Physics* **17**, 715-719 (2021).
76. H. Li *et al.*, Imaging local discharge cascades for correlated electrons in WS2/WSe2 moiré superlattices. *Nature Physics*, (2021).
77. C. Zhang *et al.*, Probing critical point energies of transition metal dichalcogenides: surprising indirect gap of single layer WSe2. *Nano letters* **15**, 6494-6500 (2015).
78. S. Jung *et al.*, Evolution of microscopic localization in graphene in a magnetic field from scattering resonances to quantum dots. *Nature Physics* **7**, 245-251 (2011).
79. V. W. Brar *et al.*, Gate-controlled ionization and screening of cobalt adatoms on a graphene surface. *Nature Physics* **7**, 43-47 (2011).
80. D. Wong *et al.*, Characterization and manipulation of individual defects in insulating hexagonal boron nitride using scanning tunnelling microscopy. *Nature nanotechnology* **10**, 949-953 (2015).
81. K. Teichmann *et al.*, Controlled charge switching on a single donor with a scanning tunneling microscope. *Physical review letters* **101**, 076103 (2008).
82. R. Geick, C. Perry, G. Rupprecht, Normal modes in hexagonal boron nitride. *Physical Review* **146**, 543-547 (1966).
83. C. Jin *et al.*, Stripe phases in WSe2/WS2 moir\'e superlattices. *arXiv preprint arXiv:2007.12068*, (2020).
84. Y. Xu *et al.*, Abundance of correlated insulating states at fractional fillings of WSe $ _ {2} $/WS $ _ {2} $ moir\'e superlattices. *arXiv preprint arXiv:2007.11128*, (2020).
85. X. Huang *et al.*, Correlated Insulating States at Fractional Fillings of the WS2/WSe2 Moir\'e Lattice. *arXiv preprint arXiv:2007.11155*, (2020).
86. V. Goldman, M. Santos, M. Shayegan, J. Cunningham, Evidence for two-dimentional quantum Wigner crystal. *Physical review letters* **65**, 2189 (1990).
87. J. Jang, B. M. Hunt, L. N. Pfeiffer, K. W. West, R. C. Ashoori, Sharp tunnelling resonance from the vibrations of an electronic Wigner crystal. *Nature Physics* **13**, 340-344 (2017).
88. H. Zhou, H. Polshyn, T. Taniguchi, K. Watanabe, A. Young, Solids of quantum Hall skyrmions in graphene. *Nature Physics* **16**, 154-158 (2020).
89. I. Shapir *et al.*, Imaging the electronic Wigner crystal in one dimension. *Science* **364**, 870-875 (2019).
90. X. Huang *et al.*, Correlated insulating states at fractional fillings of the WS 2/WSe 2 moiré lattice. *Nature Physics*, 1-5 (2021).
91. V. V. Deshpande, M. Bockrath, The one-dimensional Wigner crystal in carbon nanotubes. *Nature Physics* **4**, 314-318 (2008).
92. P. K. Lam, S. Girvin, Liquid-solid transition and the fractional quantum-Hall effect. *Physical Review B* **30**, 473 (1984).
93. D. Levesque, J. Weis, A. MacDonald, Crystallization of the incompressible quantum-fluid state of a two-dimensional electron gas in a strong magnetic field. *Physical Review B* **30**, 1056 (1984).
94. D. C. Tsui, H. L. Stormer, A. C. Gossard, Two-dimensional magnetotransport in the extreme quantum limit. *Physical Review Letters* **48**, 1559 (1982).
95. K. v. Klitzing, G. Dorda, M. Pepper, New method for high-accuracy determination of the fine-structure constant based on quantized Hall resistance. *Physical review letters* **45**, 494 (1980).

96. R. Crandall, R. Williams, Crystallization of electrons on the surface of liquid helium. *Physics Letters A* **34**, 404-405 (1971).
97. R. Williams, R. Crandall, A. Willis, Surface states of electrons on liquid helium. *Physical Review Letters* **26**, 7 (1971).
98. C. Grimes, G. Adams, Evidence for a liquid-to-crystal phase transition in a classical, two-dimensional sheet of electrons. *Physical Review Letters* **42**, 795 (1979).
99. F. Williams, Collective aspects of charged-particle systems at helium interfaces. *Surface Science* **113**, 371-388 (1982).
100. H. Pan, F. Wu, S. D. Sarma, Quantum phase diagram of a Moiré-Hubbard model. *Physical Review B* **102**, 201104 (2020).
101. H. Li *et al.*, Imaging two-dimensional generalized Wigner crystals. *Nature* **597**, 650-654 (2021).
102. H. Li *et al.*, Imaging local discharge cascades for correlated electrons in WS2/WSe2 moir\'e superlattices. *arXiv preprint arXiv:2102.09986*, (2021).
103. W. Schutte, J. De Boer, F. Jellinek, Crystal structures of tungsten disulfide and diselenide. *Journal of Solid State Chemistry* **70**, 207-209 (1987).
104. Y. Zhang *et al.*, Giant phonon-induced conductance in scanning tunnelling spectroscopy of gate-tunable graphene. *Nature Physics* **4**, 627-630 (2008).
105. D. Wong *et al.*, Spatially resolving density-dependent screening around a single charged atom in graphene. *Physical Review B* **95**, 205419 (2017).
106. F. Yang *et al.*, Experimental determination of the energy per particle in partially filled Landau levels. *arXiv preprint arXiv:2008.05466*, (2020).
107. T. Li *et al.*, Charge-order-enhanced capacitance in semiconductor moir\'e superlattices. *arXiv preprint arXiv:2102.10823*, (2021).
108. S. L. Tomarken *et al.*, Electronic compressibility of magic-angle graphene superlattices. *Physical review letters* **123**, 046601 (2019).
109. B. Padhi, R. Chitra, P. W. Phillips, Generalized Wigner crystallization in moiré materials. *Physical Review B* **103**, 125146 (2021).
110. S. Tessmer, P. Glicofridis, R. Ashoori, L. Levitov, M. Melloch, Subsurface charge accumulation imaging of a quantum Hall liquid. *Nature* **392**, 51-54 (1998).
111. G. Finkelstein, P. Glicofridis, R. Ashoori, M. Shayegan, Topographic mapping of the quantum Hall liquid using a few-electron bubble. *Science* **289**, 90-94 (2000).
112. G. A. Steele, R. Ashoori, L. Pfeiffer, K. West, Imaging transport resonances in the quantum Hall effect. *Physical review letters* **95**, 136804 (2005).
113. Y.-M. Xie, C.-P. Zhang, J.-X. Hu, K. F. Mak, K. T. Law, Valley-Polarized Quantum Anomalous Hall State in Moiré MoTe 2/WSe 2 Heterobilayers. *Physical Review Letters* **128**, 026402 (2022).
114. C. Jin *et al.*, Observation of moiré excitons in WSe 2/WS 2 heterostructure superlattices. *Nature* **567**, 76-80 (2019).
115. M. H. Naik *et al.*, Intralayer charge-transfer moiré excitons in van der Waals superlattices. *Nature* **609**, 52-57 (2022).
116. K. L. Seyler *et al.*, Signatures of moiré-trapped valley excitons in MoSe 2/WSe 2 heterobilayers. *Nature* **567**, 66-70 (2019).
117. K. Tran *et al.*, Evidence for moiré excitons in van der Waals heterostructures. *Nature* **567**, 71-75 (2019).
118. O. Karni *et al.*, Structure of the moiré exciton captured by imaging its electron and hole. *Nature* **603**, 247-252 (2022).
119. M. Imai-Imada *et al.*, Orbital-resolved visualization of single-molecule photocurrent channels. *Nature* **603**, 829-834 (2022).
120. L. Wang, Y. Xia, W. Ho, Atomic-scale quantum sensing based on the ultrafast coherence of an H2 molecule in an STM cavity. *Science* **376**, 401-405 (2022).

121. X. Qiu, G. Nazin, W. Ho, Vibrationally resolved fluorescence excited with submolecular precision. *Science* **299**, 542-546 (2003).
122. E. Ćavar *et al.*, Fluorescence and phosphorescence from individual C 60 molecules excited by local electron tunneling. *Physical review letters* **95**, 196102 (2005).
123. L. Bolotov, T. Tada, V. Poborchii, K. Fukuda, T. Kanayama, Spatial distribution of photocurrent in Si stripes under tilted illumination measured by multimode scanning probe microscopy. *Japanese Journal of Applied Physics* **51**, 088005 (2012).
124. H. Y. H. Yamamoto, I. K. I. Kamiya, T. T. T. Takahashi, Photoinduced current properties of InAs-covered GaAs studied by scanning tunneling microscopy. *Japanese journal of applied physics* **38**, 3871 (1999).
125. O. Takeuchi *et al.*, Probing subpicosecond dynamics using pulsed laser combined scanning tunneling microscopy. *Applied physics letters* **85**, 3268-3270 (2004).
126. M. McEllistrem, G. Haase, D. Chen, R. Hamers, Electrostatic sample-tip interactions in the scanning tunneling microscope. *Physical review letters* **70**, 2471 (1993).
127. G. P. Kochanski, R. Bell, STM measurements of photovoltage on Si (111) and Si (111): Ge. *Surface science* **273**, L435-L440 (1992).
128. T. W. Matthes *et al.*, Investigation of photoinduced tunneling current and local surface photovoltage by STM. *Applied surface science* **123**, 187-191 (1998).
129. F. Wu, T. Lovorn, A. H. MacDonald, Topological exciton bands in moiré heterojunctions. *Physical review letters* **118**, 147401 (2017).
130. Y. Zeng, A. H. MacDonald, Strong modulation limit of excitons and trions in moiré materials. *Physical Review B* **106**, 035115 (2022).
131. M. H. Naik, S. Kundu, I. Maity, M. Jain, Origin and evolution of ultraflat bands in twisted bilayer transition metal dichalcogenides: Realization of triangular quantum dots. *Physical Review B* **102**, 075413 (2020).
132. C. Jin *et al.*, Ultrafast dynamics in van der Waals heterostructures. *Nature nanotechnology* **13**, 994-1003 (2018).
133. H. Wang, C. Zhang, F. Rana, Ultrafast dynamics of defect-assisted electron–hole recombination in monolayer MoS2. *Nano letters* **15**, 339-345 (2015).
134. H. Shi *et al.*, Exciton dynamics in suspended monolayer and few-layer MoS2 2D crystals. *ACS nano* **7**, 1072-1080 (2013).
135. L. A. Jauregui *et al.*, Electrical control of interlayer exciton dynamics in atomically thin heterostructures. *Science* **366**, 870-875 (2019).
136. M. S. Hybertsen, S. G. Louie, Electron correlation in semiconductors and insulators: Band gaps and quasiparticle energies. *Physical Review B* **34**, 5390 (1986).
137. M. Rohlfing, S. G. Louie, Electron-hole excitations in semiconductors and insulators. *Physical review letters* **81**, 2312 (1998).
138. M. Rohlfing, S. G. Louie, Electron-hole excitations and optical spectra from first principles. *Physical Review B* **62**, 4927 (2000).